N-05-66-1 • JUNE 1966

N-05-66-1

THERMAL SCALE MODELING IN A SIMULATED SPACE ENVIRONMENT

June 1966

Technical Summary Report for Period
June 1, 1964 to April 30, 1966

THERMAL SCALE MODELING IN A SIMULATED SPACE ENVIRONMENT

NAS 8-11152

by

R. E. Rolling

Aerospace Sciences Laboratory
Lockheed Palo Alto Research Laboratory
LOCKHEED MISSILES & SPACE COMPANY
A Group Division of Lockheed Aircraft Corporation
Palo Alto, California

FOREWORD

This report was prepared by the Palo Alto Research Laboratory of Lockheed Missiles & Space Company, for the George C. Marshall Space Flight Center of the National Aeronautics and Space Administration. The work was performed under Contract NAS 8-11152 and was administered by the Research Projects Laboratory of Marshall Space Flight Center, with Mr. B. P. Jones and Mr. J.R. Watkins as contract officers.

This Technical Summary Report describes work performed from 1 June 1964 to 30 April 1966.

ACKNOWLEDGMENT

The author gratefully acknowledges the advice, interest, and enthusiastic encouragement offered by Mr. B. P. Jones and Mr. J. R. Watkins of the Research Projects Laboratory, Marshall Space Flight Center. Their continued efforts in support of the program objectives were of immeasurable assistance in achieving a successful experimental demonstration of thermal modeling.

The author also acknowledges the interest and significant contributions of Mr. W. E. Morton, Mr. T. F. Vajta, and Mrs. M. A. White of the Thermophysics Group, Aerospace Sciences Laboratory, Lockheed Missiles & Space Company, Palo Alto, California. Their efforts in model construction, testing, thermal analyses, and instrumentation made possible a successful completion of the program.

CONTENTS

ILLUSTRATIONS

TABLES

Section 1
INTRODUCTION

Successful operation of manned and unmanned spacecraft on planetary or interplanetary missions is dependent to a large extent upon maintenance of proper thermal levels for all operational systems within the vehicle. Thermal control is established through proper design of the conductive and radiative heat-transfer paths between components in the vehicle in conjunction with control of the exterior radiative exchange of the vehicle with its environment. The design itself is based upon the results of extensive efforts in thermophysical properties measurement, coating system development and application, thermal analysis, and system thermal testing. Current practice requires a simulated flight test of either a full-scale thermal model or the actual hardware to verify that the final assembly is a successful combination of the many disciplines involved.

Simulated flight tests are performed in large environmental chambers that have the capability of providing a match of the thermal environment of space. The general requirements of such chambers are that the vacuum, space thermal sink, and solar irradiation are provided with sufficient accuracy to establish flight thermal behavior of the test object. Such requirements may be achieved; however, the chambers have exceedingly high initial, operational, and maintenance costs which rise in an exponential manner as chamber size and test complexity increase. In spite of the considerable efforts expended in vehicle thermal design, it is still frequently found that manufacturing tolerances in combination with inherent uncertainties in the design thermal analyses result in thermal failures during final acceptance tests. Discovery of inadequate performance at this stage of manufacture leads to expensive modifications and repetition of the acceptance test effort. Only limited knowledge of the scope and expense of such corrective procedures is required to conclude that any efforts that provide greater

certainty of achieving satisfactory performance with the initial design are of considerable value. A possible approach to reducing the possibility of error is incorporation of thermal modeling techniques into the design and test effort. Small-scale thermal models have the capability of demonstrating actual thermal performance of subsystems or complete satellite assemblies when subjected to a simulated space thermal environment. Results obtained from these models can be used concurrently with the design or testing effort to point out potential difficulties prior to assembly of flight hardware. They also have considerable potential as substitutes for full-scale testing where sufficiently large facilities are not available to simulate flight conditions on large satellites and orbiting space stations.

The use of model studies for prediction of full-scale behavior is a well established procedure in many scientific and engineering disciplines. Maximum use of the procedure has probably been in the area of fluid dynamics where wind tunnels, towing tanks, and hydraulic models have provided highly accurate forecasts of the behavior of full-scale objects under real conditions. However, the use of models for prediction of spacecraft thermal behavior is not yet an accepted or well developed procedure. Interest in this application is increasing as is evident from the growing number of publications on the subject. The derivation of modeling criteria has been discussed by Katzoff (Ref. 1), Wainwright (Ref. 2), and Chao (Ref. 3) where dimensionless groups are presented and their application to model design discussed. Jones (Ref. 4) has established generalized modeling criteria as they apply to heat transfer in the space environment and has discussed the applicability of these criteria to a variety of design approaches. Experimental studies have been conducted by Clark (Ref. 5), Fowle (Ref. 6), Vickers (Ref. 7), and others where model configurations were used to determine the behavior of flight hardware. Adkins (Ref. 8) and Jones (Ref. 9) have also demonstrated the application of thermal modeling to prediction of temperatures for a specially designed test system. These are but a few of the recent publications on this subject. However, they are representative of the work being accomplished in thermal similitude. A more complete review of activity was given by Vickers (Ref. 10) in an article whose purpose was to discuss the state-of-the-art in thermal modeling of spacecraft.

Most of the efforts to date have dealt with the problem of duplicating or predicting the steady state behavior of spacecraft. This is undoubtedly due to the considerable complication introduced when transient considerations must be included both in design of the model and in operation of the test. However, if the true utility of the procedure is to be realized it is necessary that transient models be included in studies of the approach.

This report describes a program that demonstrates the accuracy of models in prediction of steady state and transient thermal performance in the space environment. The study was primarily experimental in nature since a laboratory demonstration of the technique was desired. The configurations chosen for test were simple geometrically, but provided the thermal complexity of spacecraft systems in current use. The test objects were subjected to a simulated thermal near-earth orbit, as well as a steady state heat-flux input. The results of these tests provide strong justification for continued development and use of the model approach.

Section 2

MODEL CRITERIA

2.1 DERIVATION OF THE MODEL LAWS

A number of techniques are available for derivation of the basic modeling criteria applicable to thermal conditions in the space environment. A purely dimensional approach can be used to establish a variety of independent groups. This technique has been thoroughly demonstrated by J. R. Watkins at the Marshall Space Flight Center (Refs. 11, 12, 13, 14) where a computer program was developed to establish the dimensionless parameters which apply under various conditions. A second method is to establish the behavioral equations of the system and derive the similarity criteria directly from these equations. Given that a systems behavior is properly understood in terms of its governing influences, it is probable that either technique will result in selection of identical modeling criteria. However, since the derivation of criteria from the behavioral equations will normally provide better insight into the relative strength of each dimensionless parameter, this was the method used in this program.

For a spacecraft system free from atmospheric influences it is possible to establish a generalized differential equation which describes the energy transfer at each incremental volume in the system. If such a volume is considered in terms of its heat capacity, its radiative and conductive energy transfer, and its internal energy generation, then the following terms will be required to perform an energy balance on the increment.

$\rho_i V_i C_p \frac{dT_i}{d\theta}$ — Rate of change of element sensible heat due to energy transfer to or from the element or energy production within the element. Subscript i denotes the element of interest.

$A_{s_i} S \mathcal{J}_{s_i}$ — Energy rate absorbed by i due to incident solar flux S. A_{s_i} is the area of i receiving solar energy, and $\mathcal{J}_{s_i}$ is a factor which is defined as the ratio of solar flux rate absorbed by i to the total solar flux rate falling on the vehicle. Therefore, it accounts for all internal reflections of energy and includes the reflectance and absorptance of materials involved in transfer of solar energy to the ith element. This form is used here to simplify the resulting equation.

$A_{r_i} R \mathcal{J}_{r_i}$ — Energy rate absorbed by element i due to planet albedo.

$A_{e_i} E \mathcal{J}_{e_i}$ — Energy rate absorbed by element i due to planet emission.

Q_i — Energy rate produced or absorbed by sources internal to element i .

$K_n A_n \frac{dTi\text{-}n}{dXi\text{-}n}$ — Energy rate conducted to or from i along the path n due to supporting or adjacent elements.

$\sigma A_i \mathcal{J}_{i-j}(Tj^4 - Ti^4)$ — Energy rate gained or lost due to radiant exchange between the i and j elements. $\mathcal{J}_{i-j}$ accounts for all inter-reflections and is the ratio of energy from i absorbed by j to the total energy emitted by a black body at Tj.

The total energy balance on the ith element becomes:

$$\rho_i V_i Cp_i \frac{dTi}{d\theta} = A_{s_i} S \mathcal{J}_{s_i} + A_{r_i} R \mathcal{J}_{r_i} + A_{e_i} E \mathcal{J}_{e_i} + Q_i - \sum_{n=1}^{N} K_n A_n \frac{dTi-n}{dXi-n}$$

$$+ \sum_{j=1}^{J} \sigma A_i \mathcal{J}_{i-j} (Tj^4 - Ti^4) \qquad (1)$$

It has been assumed in the above formulation that the incremental element under consideration has a uniform temperature $T = T_i$ over its volume. This assumption is entirely valid for the derivation of modeling criteria and, in fact, is not mathematically restrictive where the elemental size is sufficiently small. It has also been assumed that radiation and conduction are the only heat transfer modes of interest. For manned spacecraft the additional influence of gaseous conduction and forced convection would be considered for the interior of the vehicle. However, since this program was conducted on systems free of gaseous effects, these considerations have not been included in Eq. (1).

A complete energy balance on the vehicle can be achieved by machine solution of N simultaneous equations of the type derived. However, for establishment of the model ratios, one such governing equation is sufficient.

If the thermal model representing a given system is to have a behavior which reflects prototype behavior then it is necessary that the model system also obey Eq. (1). Since point-by-point correspondence is desired between the model and prototype, it is obvious that each equation written for the prototype elements will have a similar equation written for a corresponding element in the model. The difference between the sets of equations will be that those applying to the model contain model properties and temperatures while those applying to the prototype contain prototype properties and temperatures.

If the ratio of a property at similar points on the model and the prototype is represented by an asterisk, for example

$$L^* = \frac{L_m}{L_p} = \frac{\text{representative length of model}}{\text{representative length of prototype}}$$

$$\rho^* = \frac{\rho_m}{\rho_p} = \frac{\text{density of model material}}{\text{density of prototype material}}$$

then the model equation can be placed in the form

$$\frac{\rho^* V^* C^* T^*}{\theta^*}\left[\rho_i V_i C_{p_i}\frac{dTi}{d\theta}\right]_p = A_s^* S^* \mathcal{J}_s^*\left[A_{s_i} S \mathcal{J}_{s_i}\right]_p + A_r^* R^* \mathcal{J}_r^*\left[Ar_i R \mathcal{J}r_i\right]_p$$

$$+ A_e^* E^* \mathcal{J}_e^*\left[A_{e_i} E \mathcal{J}_{e_i}\right]_p + Q^*[Q_i]_p$$

$$- \frac{K_n^* A_n^* T^*}{X^*}\left[\sum_{n=1}^{N} K_n A_n \frac{dT_{i-n}}{dX_{i-n}}\right]_p$$

$$+ A_i^* \mathcal{J}_{i-j}^* T^{*4}\left[\sum_{j=1}^{J} \sigma A_i \mathcal{J}_{i-j}\left(T_j^4 - T_i^4\right)\right]_p \qquad (2)$$

In this form the model equation is identical to the prototype expression derived as Eq. (1) with the exception of the dimensionless elements multiplying each term. It is clear that these elements must be identically equal if the prototype equation and its solution are unique. Equality of the multiplying elements will provide point-by-point similarity between the model and prototype and results in the following identities:

$$\frac{\rho^* V^* C^* T^*}{\theta^*} = A_s^* S^* \mathcal{J}_s^* = A_r^* R^* \mathcal{J}_r^* = A_e^* E^* \mathcal{J}_e^* = Q^* = \frac{K_n^* A_n^* T^*}{L^*} = A_i^* \mathcal{J}_{i-j}^* T^{*4} \qquad (3)$$

It should be emphasized that the results obtained through the above procedure apply only under the following restrictions:

(1) The ratios of properties designated as L^*, ρ^*, T^*, etc., are constants throughout the model for all test conditions and thermal levels.
(2) Geometric identity is required if point-by-point similarity is to be achieved.

Under these restrictions the model will theoretically provide a precise indication of prototype thermal behavior.

The role of geometry and surface optical properties in scaling of the complex shape factors ($\mathcal{J}$) can be demonstrated by analysis of a simple arrangement such as that of concentric spheres or cylinders. Taking such a system, where it is assumed that no interconnecting elements exist, results in the following equation for the transfer of thermal energy from one object to the other.

$$Q = \sigma \mathcal{J}_{1-2} A_1 \left[T_1^4 - T_2^4\right] \tag{4}$$

where $\mathcal{J}_{1-2}$ is the complex shape factor and includes geometry and surface properties. For this case, the factor $\mathcal{J}_{1-2}$ is given by:

$$\mathcal{J}_{1-2} = \frac{1}{1/\epsilon_1 + A_1/A_2 (1/\epsilon_2 - 1)} \tag{5}$$

A_1 and ϵ_1 are properties of the inner member. If a <u>geometrically similar</u> model of such a system were built, the model laws derived from Eq. (5) would be:

$$\mathcal{J}^*_{1-2} A^*_2 \epsilon^*_2 = \mathcal{J}^*_{1-2} A^*_1 \epsilon^*_1 = \mathcal{J}^*_{1-2} \epsilon^*_2 \epsilon^*_1 A^*_1 = A^*_2 \epsilon^*_2 \epsilon^*_1 \tag{6}$$

Since $\mathcal{J}_{1-2}A_1 = \mathcal{J}_{2-1}A_2$ (by reciprocity), then $\mathcal{J}^*_{1-2} = \mathcal{J}^*_{2-1}$. From these relationships it is found that proper modeling of the radiant condition requires $\epsilon^*_1 = \epsilon^*_2 = 1$. Thus, the radiant properties of the model must be identical to those of the prototype. This result is fortuitous since the preparation of a model with identical surface properties is within the capabilities of the model fabricator while preparation of special coatings have a specified ratio of radiative properties is a much more difficult if not impossible task. This example is a specific case of the more general formulations which apply to complex assemblies used in satellites; however, a similar analysis on the more general formulations leads to the same conclusions. Thus, values of $\mathcal{J}^* = 1$ are achieved through use of identical surface properties and Eq. (3) is simplified by elimination of the $\mathcal{J}^*$ terms.

A second simplification of the ratios can be obtained by a single identification of the terms S*, R*, E*. These are all concerned with incident energy rates; and, since it is desired to maintain the proper proportions of long and short wavelength energy in the simulated case, all such energy sources must be modeled to the same ratio. Under these circumstances it is possible to define $S^* = R^* \equiv I^*$, where I^* is an overall incident energy ratio.

Substituting in Eq. (3) and setting $\mathcal{J}^* = 1$ yields

$$\frac{\rho^* V^* C^* T^*}{\theta^*} = A^*_I I^* = Q^* = \frac{K^*_n A^*_n T^*}{L^*} = A^*_i T^{*4} \qquad (7)$$

It should be emphasized at this point that the terms applicable to geometry have not been equated to a common length ratio. These terms have been left in the forms V^*, A^*_I, A^*_n, and A^*_i in order to maintain their identity with the heat capacity, incident thermal energy, thermal conduction, and long wavelength emission or absorption. This has been done to permit individual consideration of geometric distortion in terms of the heat transfer modes involved.

The ratios in Eq. (7) are the governing similitude criteria for prediction of prototype behavior from observed model behavior. As previously indicated, the terms must be maintained identically for all comparative thermal levels of the model and prototype. This identity extends to each elemental volume and surface area and includes thermally induced changes in surface and bulk thermal properties. For example, the relationship

$$\frac{\rho^* V^* C^* T^*}{\theta^*} = \frac{K_n^* A_n^* T^*}{L^*}$$

must hold over the full range of test temperatures. If K_n and C_p are strong functions of temperature in the prototype, then their temperature dependence must be properly scaled in the model. Errors caused by overlooking such effects are covered in detail by Chao (Ref. 3) where the thermal conductivity and specific heat are considered.

The analysis presented by Chao assumes simple power law functions for both the specific heat and thermal conductivity. Under this first-order representation these properties are given by

$$\begin{aligned} K_n &= \bar{K}_n T^a \\ C_p &= \bar{C}_p T^b \end{aligned} \tag{8}$$

Using these definitions for property ratios give

$$K_n^* = \frac{\bar{K}_{n_m}}{\bar{K}_{n_p}} \frac{T_m^{a_m}}{T_p^{a_p}} = \bar{K}_n^* T^{*a_m} T_p^{(a_m - a_p)}$$

$$C_p^* = \frac{C_{P_m}}{C_{p_p}} \frac{T_m^{b_m}}{T_p^{b_p}} = \bar{C}_p T^{*b_m} T_p^{(b_m - b_p)} \tag{9}$$

Substitution of this result in Eq. (7) gives a more explicit set of model criteria that includes the assumed variation of Eqs. (8).

$$\frac{\rho^* V^* C^* T^{*(1+b_m)}_{T_p (b_m - b_p)}}{\theta^*} = A_I^* I^* = Q^* = \frac{\bar{K}_n^* A_n^* T^{*(1+a_m)}_{T_p (a_m - a_p)}}{L^*} = A_i^* T^{*4} \tag{10}$$

It has been shown that a basic requirement for similarity between the model and prototype systems is that the dimensionless ratios of properties remain constant throughout for all thermal levels of the two systems. It is clear from Eq. (10) that this is possible only for the case where $a_m = a_p$ and $b_m = b_p$. If these equalities are not met, strict similarity will not be obtained. Assuming that materials are selected which provide equal exponents, and dropping the subscripts for model and prototype gives for Eq. (10)

$$\frac{\rho^* V^* C^* T^{*(1+b)}}{\theta^*} = A_I^* I^* = Q^* = \frac{K_n^* A_n^* T^{*(1+a)}}{L^*} = A_i^* T^{*4} \tag{11}$$

This result shows that the temperature ratio between model and prototype is influenced exponentially by thermal changes in material properties. However, in many cases the absolute influence of these changes will be small. For example, most structural materials have values of the exponents a and b on the order of $a \approx 0.3$, and $b \approx 0.15$, for T in degrees Kelvin. For a room temperature component these values result in approximately a 1% change in K_n and a 0.6% change in C_p for each 10° K variation in temperature. The importance of such magnitudes must be assessed in terms of expected model behavior. Where these changes are important, care must be exercised in selection of materials with $a_m = a_p$ and $b_m = b_p$ to assure compliance with the model criteria.

Chao presents a more detailed consideration of errors in temperature prediction and time constants for geometrically distorted and geometrically similar models. The treatment included herein is only for the purpose of demonstrating that specific forms of property variations are easily inserted in the basic model criteria and are included

in the requirements which led to the statement of Eq. (7). A discussion of error introduced by thermal property variations on models used in this program will be found in Appendix A.3.

2.2 SELECTION OF MODEL PROCEDURE

In applying the criteria of Eq. (7), the investigator must have an understanding of the relative importance of each component of the heat transfer system involved. A satisfactory model design may often be achieved by use of imagination in application of the model criteria in lieu of rigorous point-by-point satisfaction of Eq. (7). Conducting path cross-sectional areas, emitting areas, and internal sources may often be distorted to some extent while a good representation of the overall heat transfer system is preserved. Such techniques may alter local temperature distributions with no measurable effect on areas removed from their immediate thermal influence. However, when exception is taken to an exact satisfaction of the model criteria, it is necessary that extreme care be used to assure that significant variations of thermal behavior have not been introduced. This requires considerable insight on the part of the investigator which may be fortified by a thorough thermal analysis of the prototype system. It is in this regard that programs using thermal models must still rely upon the established analytical techniques presently used for thermal design of spacecraft.

The model criteria in themselves do not dictate a specific model test procedure. They are entirely general in this respect and become restricted to a given approach only by the investigator's selection of a time constant, energy rates, test temperatures, or material properties. However, considerable attention has been given in previous literature to use of either "Temperature Preservation" or "Material Preservation" techniques. These are, as the terminology implies, models that are designed to identically duplicate the temperature of the prototype or that are constructed from materials identical to those of the prototype. The advantages and disadvantages of each of these approaches has been discussed in detail sufficiently often to create an impression that they are the most desirable solutions. However, they are usually selected for practical reasons related to reduction of test data or to availability of materials

rather than for reasons associated with the quality of the test results or the model criteria themselves. It is often more desirable to design models which use neither of these preservation techniques, in the interest of conducting an accurate and inexpensive model investigation.

2.2.1 Temperature Preservation

In cases where identical test temperatures are desired in the model and prototype, the temperature ratio is $T^* = 1$ and Eq. (7) becomes:

$$\frac{\rho^* V^* C^*}{\theta^*} = A_I^* I^* = Q^* = \frac{K_n^* A_n^*}{L^*} = A_i^* \tag{11}$$

Under conditions where strict geometric similiarity is maintained this reduces to:

$$\frac{\rho^* L^* C^*}{\theta^*} = I^* = \frac{Q^*}{L^{*2}} = \frac{K_n^*}{L^*} = 1 \tag{12}$$

Equation (12) indicates that proper steady state model design will require selection of model materials whose thermal conductivity is less than that of the prototype in the same ratio as the scale factor employed in model design ($K_n^* = L^*$). For small scale factors this is often a severe limitation, particularly in those cases where poor conductors are used in the prototype. This materials selection problem may often be circumvented by geometric distortion of the conducting path to provide $[K_n^* A_n^*] = L^{*3}$. This type of distortion requires reduction of the conducting path in excess of $A_n^* = L^{*2}$. However, when this is done important external radiative areas must still be maintained in the ratio $A_i^* = L^{*2}$.

When the temperature preservation model is also to serve for prediction of transient behavior, the model design is additionally complicated by the necessity for maintaining proper distribution of heat capacity $(\rho^* V^* C^*)/(L^{*2}\theta^*) = 1$. This ratio assures

an equal time constant for all elements and is set to some degree by selection of materials for maintenance of required path conductances. Total satisfaction of Eq. (12) under transient conditions with temperature preservation can become a considerable challenge to the investigator. In fact, the model design may become sufficiently difficult to negate the positive advantages of measuring prototype temperatures directly from the model test.

2.2.2 Materials Preservation

In cases where it is desirable to design a model from the same materials as the prototype, the model ratios from Eq. (7) become:

$$\frac{V^*T^*}{\theta^*} = IA_I^* = Q^* = \frac{A_n^*T^*}{L^*} = A_i^*T^{*4}$$

Then for a geometrically similar model, $T^{*3} = 1/L^*$. For small scale ratios this result requires high test temperatures for the model and may introduce excessive changes in thermophysical properties. For example, a 1/10th scale model will have measured temperatures near 645° K for prediction of 300° K temperatures on the prototype. Such high thermal levels may well exceed the useful limits of model materials. Once again the model designer must resort to geometric distortion to reduce the required model test temperature. The obvious approach in this case is to make the ratio A_n^*/A_i^* as small as possible since reduction of this ratio is directly realized as a reduction in the required model test temperature $T^{*3} = (A_n^*/A_i^*)(1/L^*)$. Any changes in model geometry to bring about this reduction must necessarily be in compliance with the remainder of the model criteria. Thus, for a transient model the distortion must be controlled for all elements to maintain $\theta^* = V^*/A_i^*T^{*3} = V^*L^*/A_n^*$ constant throughout the model. Once again this may be sufficiently difficult to negate the advantages of the approach in terms of available material thicknesses and strengths.

The preceding paragraphs point out some of the difficulties associated with the temperature and materials preservation techniques. A better understanding of the shortcomings of these procedures is obtained by attempting an actual solution to a particular problem.

The full utility of the model technique can be realized for a particular study by utilizing the complete flexibility of the model criteria. To select a preservation technique before careful consideration of other approaches will often place initial restrictions on the study which result in unnecessary difficulties. The solution to modeling any given thermal system must first be evaluated in terms of available materials, complexity of model construction, test facilities, required accuracy, test time, and overall costs. No single approach is likely to be optimum with respect to these considerations; therefore, a number of designs should be considered before a final selection is made.

Section 3
EXPERIMENTAL PROGRAM

3.1 GENERAL DISCUSSION

The purpose of the experimental program was to demonstrate that both steady state and transient behavior can be predicted from small-scale models of a prescribed thermal system. The program was conducted in two phases so that experience gained during the first phase of activity could be used to improve the quality of results obtained during the second phase. To accomplish this objective, a geometrically simple opposed disk model was designed, fabricated, tested, and the results analyzed before proceeding to a more complex truncated cone. The test data reported in subsection 3.4 clearly show that improved techniques in design and testing applied during the second phase of effort produced a higher prediction accuracy.

Model designs were in compliance with the model criteria and were accomplished with commonly available materials and construction techniques. This approach was included as part of the program scope and imposed limitations on model precision insofar as strict compliance with the model criteria could not be achieved while maintaining geometric similarity. It was necessary to include some degree of geometric distortion into the design of all models. The full-scale (prototype) objects were constructed of materials having properties and thicknesses similar to those in common use on present space hardware and they functioned at thermal levels similar to a vehicle in a near-earth orbit.

The opposed disk and enclosed cone configurations used in the program were specifically selected to include thermal effects of geometries with large space exposure and of totally enclosed systems. The full-size objects were limited in size by the volume of an available 8-ft diameter by 10-ft-long vacuum chamber. This limited the prototypes

to dimensions which could be enclosed by a 4-ft cubical volume. This size assured sufficient work space within the chamber and was compatible with available source power levels.

Each configuration was tested in full scale and at two different reduced scale ratios. This procedure was used not only to provide two separate predictions for prototype behavior, but also to indicate difficulties which might arise due to decreasing model size. Initial considerations led to the choice of scale ratios on the order of 1/2 and 1/4. These provided a desirable range for the program objectives and permitted ease of construction for the smallest sized object. Actual design of the models led to slight changes in these values since materials were not available for direct satisfaction of the initial specifications.

3.2 MODEL CONFIGURATION

3.2.1 Opposed Disks

The first test object consisted of two opposed disks, four connecting tubular members, and a single heater box. Its geometry is shown in detail in Fig. 1. Thermal design of the object was established to produce conduction through the tubular members and radiation from the front to back plate at approximately equal levels. The inside flat surfaces were coated with black Kemacryl with the exception of 1-1/2 in. of polished aluminum on the outer edge of the front plate. The tubular members were finished with polished aluminum to reduce radiant exchange along their length. The outside surface of the front plate was coated with white Kemacryl ($\alpha_s = 0.26$, $\epsilon = 0.85$) which provided a variable absorptance with changes in lamp intensity. The outside surface of the rear plate was finished with polished aluminum to reduce the radiant loss from the test object to the chamber cold walls. This was necessary to achieve average test temperatures near earth ambient. The prototype material thicknesses and diameters were selected from common stock without regard to the future difficulties of model design.

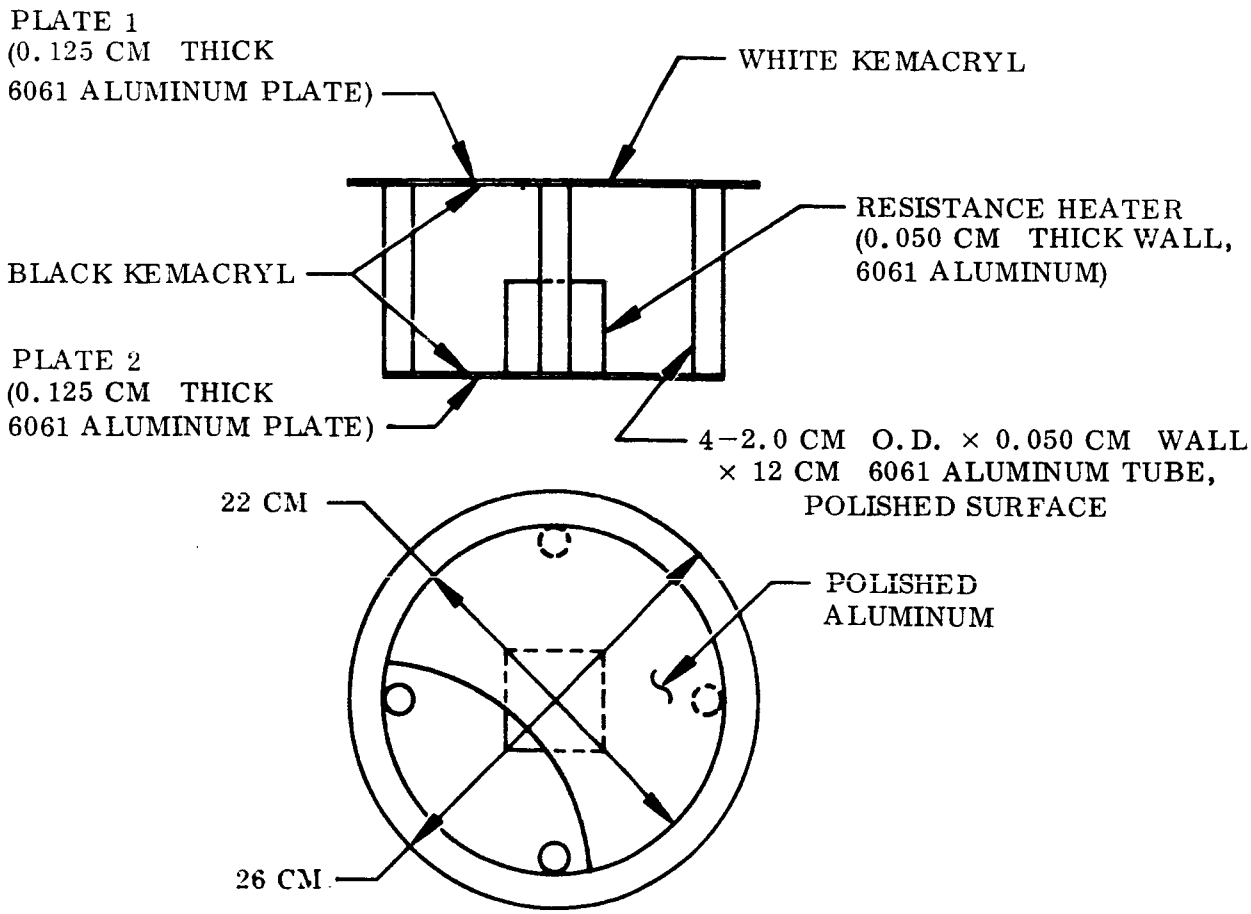

Fig. 1 Opposed Disk Geometry

Design of the half- and quarter-scale models of configuration A for steady state and transient behavior was accomplished through listing of available materials and stock sizes which approximately satisfied the model criteria of the previous section. The list was then used to generate a number of model designs. Each of these initial designs required some distortion of the conducting path cross-sectional areas. The length ratios were then altered slightly and new designs initiated. Small changes in length ratio allowed entirely different designs to be achieved. This process was repeated until a final selection could be made which closely satisfied the model criteria and which required the least amount of geometric distortion.

The design process is guided by utilization of the modeling criteria. For example, assuming geometric similarity and materials preservation for a half-scale model gives

$$T^{*3} = L^{*-1} \quad \text{or} \quad T^* = (2)^{1/3} \quad ; \quad T_m = 1.26\ T_p$$

Then since

$$I^* = T^{*4} \qquad ; \quad I_m = 2.52\ I_p$$

Under these conditions a room-temperature prototype would be modeled at 105° C (378° K) and a 1-sun prototype illumination would require 2.52 suns on the model. These conditions are already more severe than is desirable both in terms of changes in properties at elevated temperatures and available energy within the test chamber. Therefore, geometric distortion of the conducting paths is attempted. Initially it can be assumed that a choice of $A_n^* = L^{*2.5}$ with $A_i^* = L^{*2}$ may provide a satisfactory design. This distortion gives $T^* = L^{*-1/6} = 1.12$. A room-temperature component on the prototype (300° K) would then model at 60° C (333° K). The required illumination is $I_m = 1.59\ I_p$.

Use of this degree of distortion results in a model condition having a more appropriate thermal level and requires less intense energy from the source. A search is then made for material sizes that fall within the required ratio of areas. The materials

found may require some alteration of the attempted approach that will generally result in a design near the one selected. The effect of distortion must then be assessed analytically in terms of the geometries involved. This was done for model designs used in this program.

Computation of conducting path area ratios for plates and tubes was accomplished in accordance with two major simplifying assumptions. In the case of tubes it was assumed that the model must provide similarity along the length of the tube without regard to gradients in the circumferential direction. For plates the similarity was required in directions parallel to the surface while gradients through the plate thickness were assumed to be negligible. These assumptions were valid for the conditions studied and permitted model design without use of special materials.

The final designs of the half-scale model used $L^* = 1/2.14$ with $A_n^* = 1/6.69$ for both tubes and plates. The temperature and incident energy ratios were $T^* = 1.135$ and $I^* = 1.63$ respectively. These were reasonable levels for maintenance of material properties and performance of the model test with available source conditions.

The quarter-scale model design was established in a manner similar to that described with the exception that the small size of the model required use of materials other than aluminum. A choice of stainless steel provided a considerable portion of the required reduction in thermal conductivity and permitted reasonable skin thicknesses. It was also desirable since it is available in a large variety of shapes and sizes. This wide availability was required to achieve model design with minimal distortion.

Tables 1 and 2 indicate the materials used in the prototype and both models and the scale ratios resulting from this selection.

For the half-scale model, it was possible to select both tube and plate material that gave corresponding ratios of A_n^* through distortion of thicknesses and diameters. As previously indicated, the distortion of thickness ratios in this case was not serious since a highly conductive material was used. Distortion of tube diameters produced

Table 1

MATERIAL SELECTION – OPPOSED DISKS

Structure	Full Scale	Half Scale	Quarter Scale
Material	6061 Al	6061 Al	304 S.S.
Plate	0.125 in. (0.318 cm)	0.040 in. (0.104 cm)	0.078 in. (0.199 cm)
Tubing	2.0 o.d. × 0.050 in. (5.08 × 0.128 cm)	0.75 o.d. × 0.020 in. (1.91 × 0.051 cm)	9/16 o.d. × 0.028 in. (1.45 × 0.071 cm)

Table 2

MODEL RATIOS – OPPOSED DISKS

Model	Structure	Dimensionless Ratio							
		L*	A_n^*	D*	θ*	T*	Q*	I*	t*
1/2 Scale									
6061 Al	Plate	1/2.14	1/6.69		1/4.55	1.135	1/4.55	1.63	1/3.12
$\rho^* = 1$									
K* = 1	Tube	1/2.14	1/6.69	1/2.66	1/4.55	1.135	1/2.81		1/2.50
1/4 Scale									
304 S.S.	Plate	1/3.98	1/6.38		1/1.004	1.01	1/15.2	1.04	1/1.60
$\rho^* = 2.87$									
K* = 0.105									
$C_p^* = 0.571$	Tube	1/3.98	1/6.32	1/3.54	1/1.002	1.005	1/15.2		1/1.78

shape factors to the tubes which were too small for compliance with simulation of the prototype. Computations were performed to evaluate the effect of this distortion on the radiant interchange between the plates and these showed that an error in energy transfer of less than 0.1 percent was involved. This was certainly acceptable in view of the other variables involved in performance of the overall test.

Table 2 shows that it was not possible to select materials for the quarter-scale model which gave the same ratio of A_n^* for tubes and plates. This resulted in dissimilar time and temperature ratios for these components as shown in the T^* and θ^* columns. However, the variation was small enough to be negligible and was not corrected for in the model construction. If a partial correction of the difference were desired, it could have been achieved by using a slightly different L^* for the tubes than was used for the plates since this would have almost no effect on the shape factors. However, due to the small differences in T^* and θ^* it is doubtful that any improvement in performance would have been observed through such a procedure.

The plates, tubes, and heater box on all sizes of the opposed disks were assembled with welded joints. This construction provided high conductance joints and eliminated possible effects of variable properties at these interfaces.

Preparation of surface coatings was performed concurrently on all three models to assure identity of these coatings as required by the model criteria. Paints were applied in accordance with those specifications currently used for spacecraft manufacture. No special procedures were implemented to achieve thinner coatings on the model than on the prototype, although care was used to limit the thickness to that required for opacity. The radiative properties of surfaces were inspected for proper values of spectral reflectance and infrared emittance using a Lion Optical Surface Comparator. Values obtained on the test objects were compared to those obtained on small disks prepared during the painting process. The small disks were evaluated using a Gier-Dunkle-type integrating sphere reflectometer and a heated cavity hohlraum. This procedure assured that the thermal radiation properties of the coatings were identical for all three sizes of the opposed disks. Figure 2 shows the completed test objects.

Fig. 2 Opposed Disk Test Objects

Internal energy dissipation was supplied by electrical heaters manufactured from tungsten filaments. For the opposed disks, these filaments were obtained by removal from commercially available lights. In all cases the filament size was rated at considerably greater wattage than that used in the test. The test conditions including the filament power are included in detail in subsection 3.3.

The prototype and two models were instrumented with 13 copper-constantan thermocouples located as shown in Fig. 3. For the full-scale and quarter-scale sizes, the thermocouples were drilled and peened into the surface before application of thermal-control paints. For the half-scale model this was not possible due to the thin materials used in construction. Therefore, the thermocouples were beaded and epoxied to the surface with a high conductance epoxy prior to application of the paint. The thermal response of all junctions was checked with a high sensitivity surface probe thermometer before installation in the vacuum chamber. Following installation in the chamber the absolute response was checked by variation of the chamber internal temperature over the range of anticipated test temperatures. While this procedure did not duplicate actual run conditions, it did assure that the wire response for all junctions was not affected by installation procedures. During actual runs the thermocouple response was further influenced by thermal gradients through paint thickness and along the wire length. Changes in calibration due to these gradients were assumed to be less than 1° K. The 15-ft long thermocouple wires were passed through epoxied feed-throughs in the vacuum vessel and directly connected to instrumentation exterior to the vessel. This assured that intervening thermocouple junctions were not created along the length of the wire and eliminated this source of spurious emf. The sample mounting technique, vacuum conditions, cold wall and source operation, and instrumentation are described in subsection 3.3.

3.2.2 Truncated Cone

Configuration C consisted of a totally enclosed truncated cone whose interior, including the flat end plates, was removable from the conical skin. The geometry of the full-scale test object is shown in detail in Fig. 4. Thermal design was again

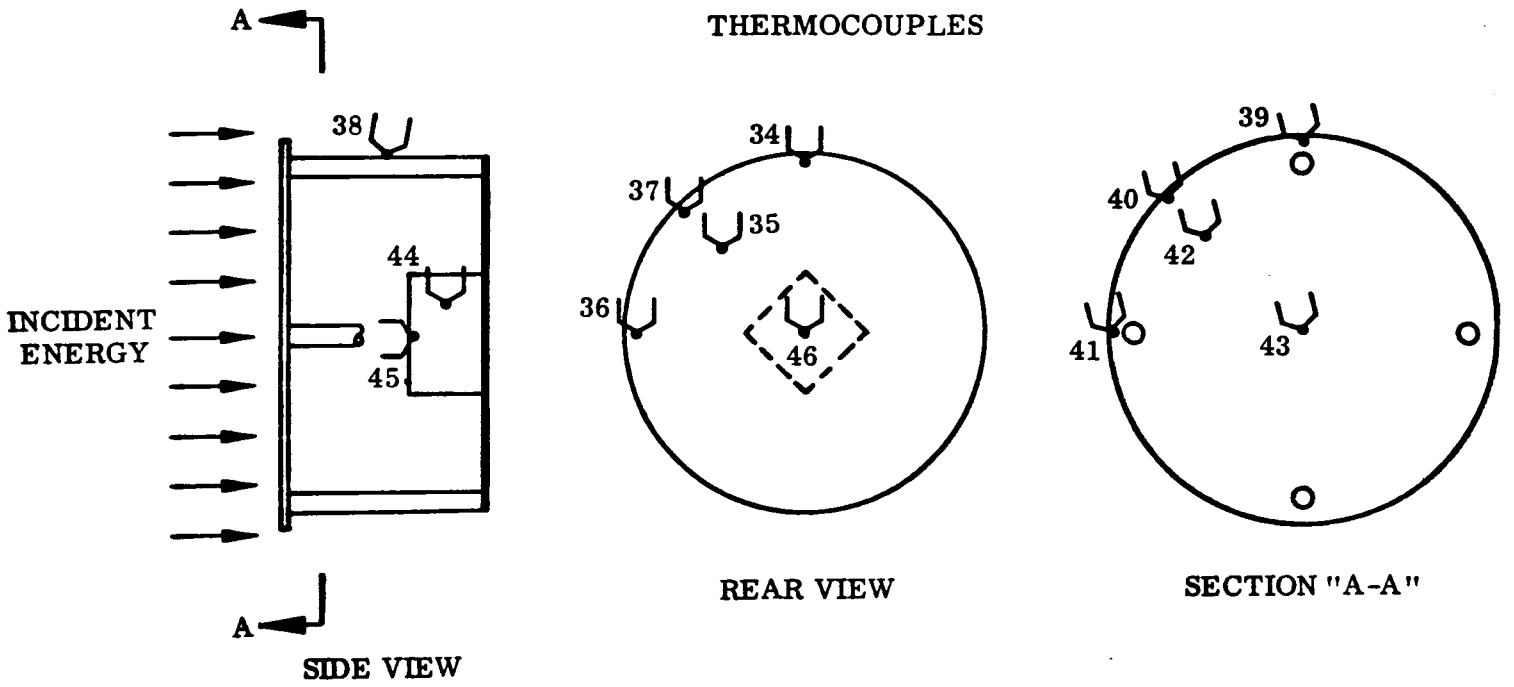

Fig. 3 Opposed Disk Thermocouple Locations

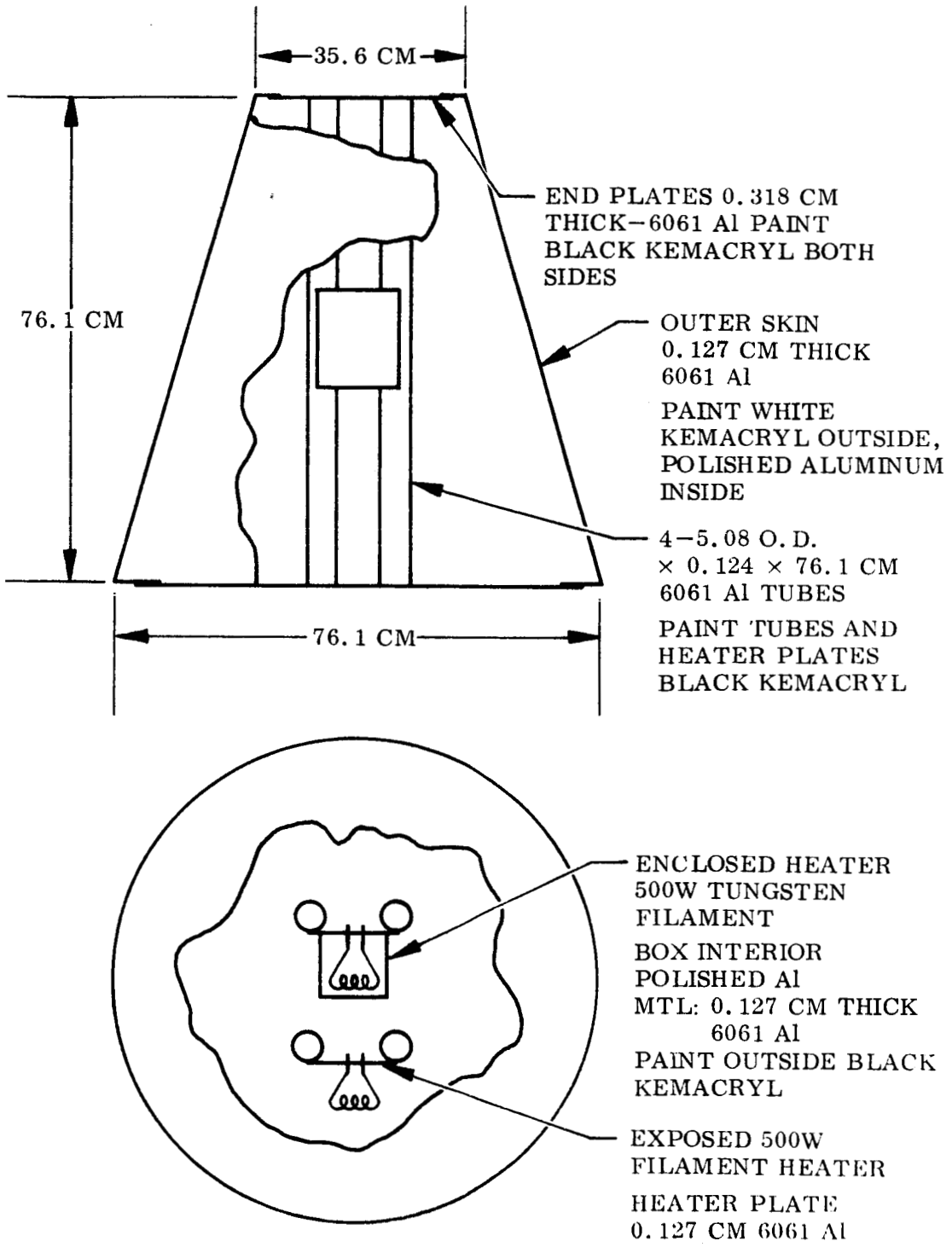

Fig. 4 Truncated Cone Geometry

directed toward producing a geometry that would provide test temperatures in the range expected from unmanned satellites while relying equally upon conduction and radiation for distribution of energy within the enclosure.

The prototype contained two internal heaters which were independently operated during the test. One heater was enclosed within a box to assure distribution of its energy by conduction along the mounting bracket and support tubing. The other was left open to provide distribution primarily by radiation. The removable section of the cone interior was coated with a high-emittance black paint while the interior surface of the conical skin was of polished aluminum. These surface finishes assured a complex distribution of radiant energy in the interior. Exterior surfaces on both ends were coated with a black paint while the exterior of the cone was covered with white Kemacryl having properties as presented in Appendix A.

Design of half- and quarter-scale models of the cone followed the same procedures as those used for the opposed disk of configuration A. The final model ratios used were based upon the availability of common materials for satisfaction of the model laws. Table 3 contains the material sizes and dimensions used for the models and demonstrates that geometrical distortion was necessary to achieve compliance with the transient model laws. Table 4 presents the model scale ratios which resulted from the stated material selection.

The interior removable section was entirely of welded construction to minimize the effects of joint resistance. The exterior cone assembly was rolled to shape, the longitudinal seam riveted, and the end pieces welded on. The procedure was necessary to avoid considerable warpage at the seam. The riveted joint was butted together and reinforced with a small backing plate. Indium was used as a filler in the joint to assure thermal contact of mating surfaces. This procedure was also followed on the models with care taken to provide joints whose conductance and mass were in compliance with the governing model criteria. The assembled truncated cones are shown in Fig. 5.

Table 3

MATERIAL SELECTION – TRUNCATED CONES

Structure	Full Scale	Half Scale	Quarter Scale
Material	6061 Al	6061 Al	304 S.S.
Outer skin	0.050 in. (0.128 cm)	0.016 in. 0.041 cm)	0.032 in. (0.081 cm)
Tubes	2.0 o.d. × 0.050 in. (5.08 × 0.128 cm)	0.75 o.d. × 0.020 in. (1.91 × 0.051 cm)	9/16 o.d. × 0.28 in. (1.45 × 0.071 cm)
End plates	0.125 in. (0.318 cm)	0.040 in. (0.104 cm)	0.078 in. (0.199 cm)
Heater box	0.050 in. (0.128 cm)	0.016 in. (0.041 cm)	0.032 in. (0.081 cm)

Table 4

MODEL RATIOS – TRUNCATED CONES

Model	Structure	Dimensionless Ratio							
		L*	A_n^*	D*	t*	θ*	T*	Q*	I*
1/2 Scale	Outer skin	1/2.14	1/6.69		1/3.12	1/4.55	1.135	1/2.81	1.63
6061 Al	Tubes	1/2.14	1/6.69	1/2.66	1/2.50	1/4.55	1.135	1/2.81	
$\rho^* = 1$ $K^* = 1$	End plates	1/2.14	1/6.69		1/3.12	1/4.55	1.135	1/2.81	1.63
$C_p^* = 1$	Heater box	1/2.14	1/6.69		1/3.12	1/4.55	1.135	1/2.81	
1/4 Scale	Outer skin	1/3.98	1/6.21		1/1.56	1/1.004	1.01	1/15.2	1.04
304 S.S.	Tubes	1/3.98	1/6.21	1/3.54	1/1.78	1/1.002	1.005	1/15.2	
$\rho^* = 2.87$ $K^* = 0.105$	End plates	1/3.98	1/6.38		1/1.60	1/1.004	1.015	1/15.2	
$C_p^* = 0.571$	Heater box	1/3.98	1/6.21		1/1.56	1/1.004	1.01	1/15.2	1.04

Fig. 5 Truncated Cone Test Objects

The prototype and models were instrumented with 25 copper-constantan thermocouples in the locations shown on Fig. 6. The same installation procedures were used as those described for the opposed disks. However, considerably more care was taken to determine thermocouple response as a function of sample temperature. Each junction was calibrated for steady state and transient thermal response under conditions similar to those of the test runs. Several thermocouples had to be replaced due to poor transient response.

The mounting technique used for the cones provided isolation of the samples from their mounts and also permitted rotation of the samples relative to the source lamp bank. The details of chamber installation and the test procedure are contained in subsection 3.3.

3.3 TEST CONDITIONS

3.3.1 Chamber System

The vacuum chamber used for testing of the models was an 8-ft diameter by 10-ft long horizontal cylinder with a high vacuum capability. The chamber interior was completely lined with blackened cryogenically cooled walls to reduce the thermal background to a minimum. Liquid nitrogen at an average pressure of 35 psia was recirculated through the walls at a rapid rate to assure the highest degree of temperature uniformity. Inlet and outlet pressure of the coolant was controlled to maintain single-phase flow throughout the system with separation of the gas phase occurring after return to the storage vessel.

The chamber was pumped with a 36-in. oil diffusion pump capable of maintaining a working pressure of 2×10^{-8} Torr with the nitrogen cooled walls. The forepump was a 600 liter/sec jet ejector backed by a 250 ft^3/min oil-sealed mechanical pump. This system was valved and trapped to provide minimum backstreaming to the working chamber with maximum pumping speed.

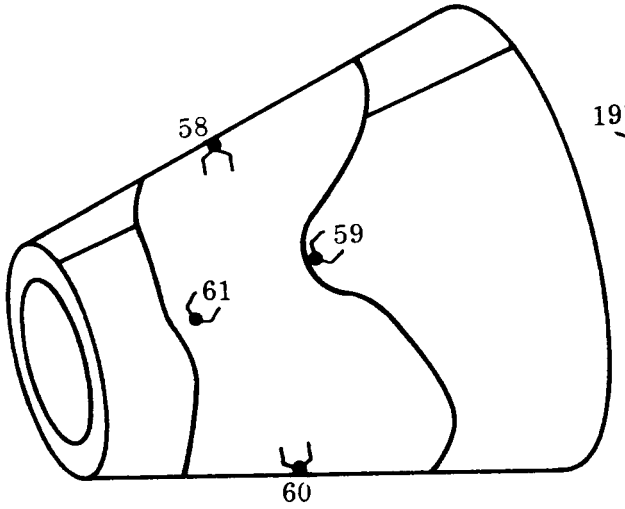

THERMOCOUPLES NO. 58, 59, 60, 61 LOCATED ON INTERIOR OF CONE

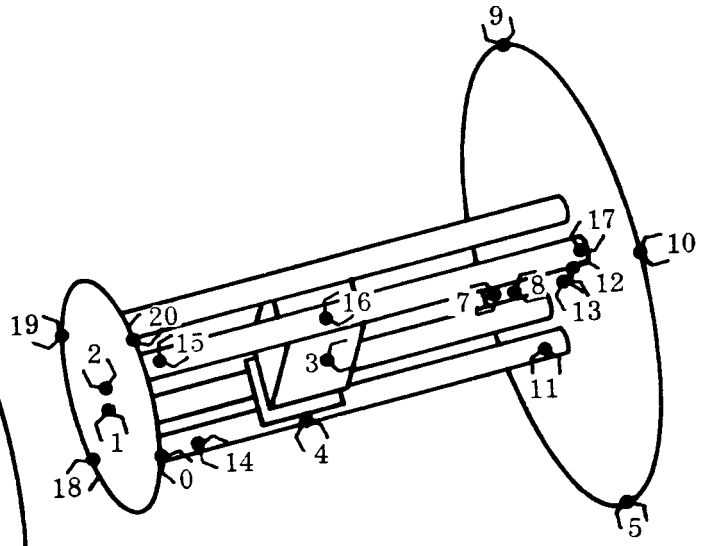

THERMOCOUPLES NO. 0, 1, 2, 18, 19, 20 LOCATED ON INTERIOR SIDE OF END PLATE

THERMOCOUPLE NO. 6 NOT SHOWN IS LOCATED ON INSIDE OF LARGE END 180 DEG FROM NO. 10

Fig. 6 Truncated Cone Thermocouple Locations

All valves and controls were electrically actuated in the proper sequence by a fully automatic control console which allowed complete operation of the facility by a single technician. Figure 7 indicates the details of the vacuum system, valving, and liquid nitrogen supply system.

3.3.2 Opposed Disk Test Conditions

Installation of the test object in the chamber was accomplished by mounting the specimen to a framework supported by the removable door of the chamber as indicated on Fig. 8. This permitted the entire system to be instrumented and checked out before placing it in the chamber for test. The prototype and models were suspended from the overhead frame by 3 mil (0.076 mm) stainless steel wires. Thermocouple and power leads were led out along the same framing member. The thermocouple leads were passed through epoxied feed throughs without interruption to instrumentation located near the exterior of the door. A spare door is available with the chamber which made it possible to mount and instrument a second test object during testing operations. Identical installation procedures were used for both of the doors.

The sample was oriented with the white Kemacryl-coated, solar-reflecting, thermal control surface facing the lamp bank. A thin radiation shield was placed around the edge of the illuminated plate to prevent lamp energy from striking the interior surfaces. The edge spacing between the shield and test object was 0.32 cm (1/8 in.). The shield was constructed of thin sheet aluminum with three layers of 0.0025 cm (1 mil) aluminum foil placed on its surface. This prevented energy transfer to the rear of the shield.

During performance of steady state tests, the temperatures of eight junctions were initially recorded on a multipoint, millivolt recorder which provided constant monitoring of the sample condition. Instrument response time was 1/2 sec with 2 sec required between each print. A steady condition was assumed when the recorder output showed all temperature variations to be less than 0.5° K/hr. Steady state data were then recorded by use of a Leeds and Northrop Model 8662 portable potentiometer with an agitated ice bath reference.

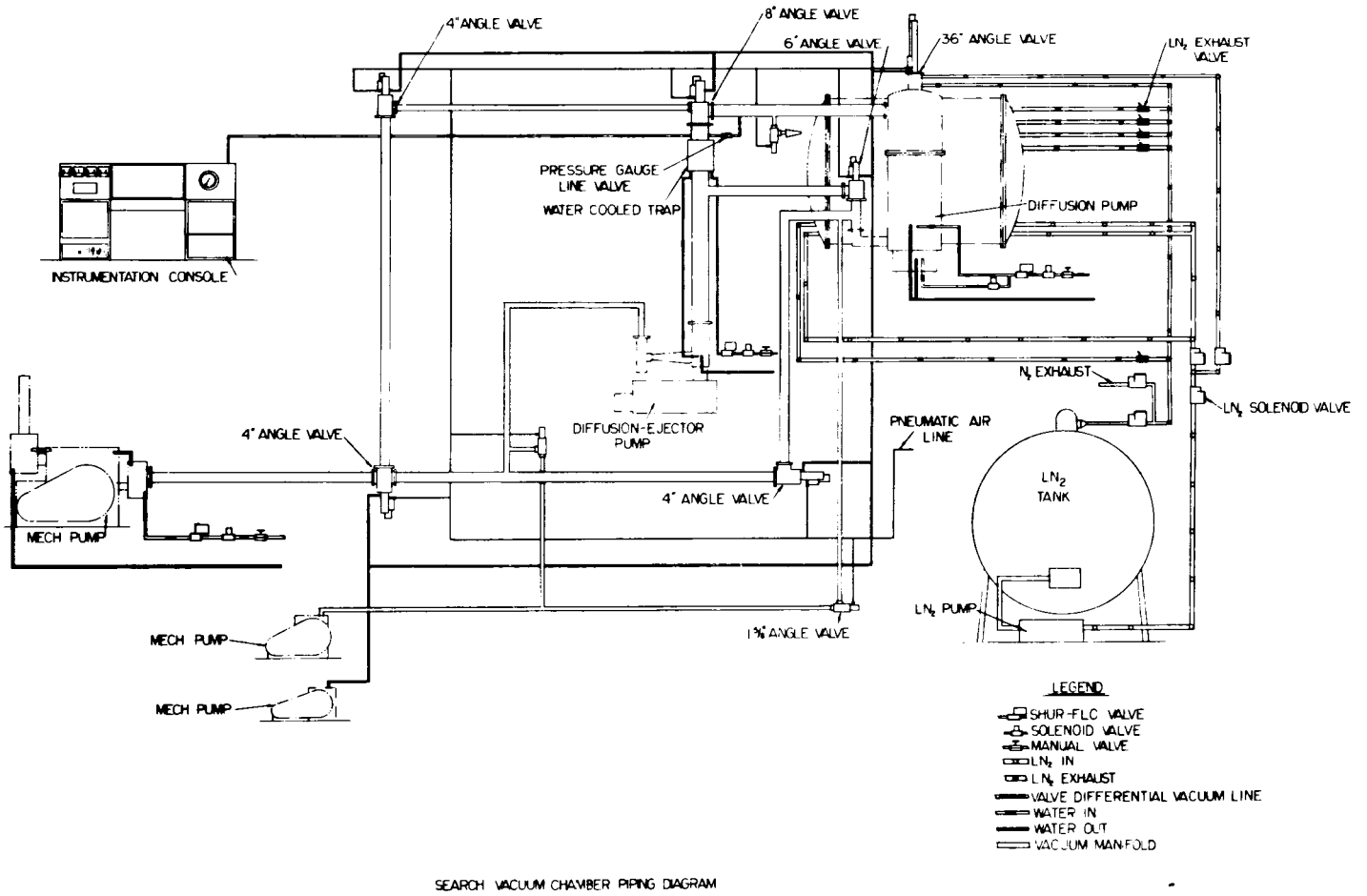

SEARCH VACUUM CHAMBER PIPING DIAGRAM

Fig. 7 SEARCH 8 ft by 10 ft Vacuum Chamber

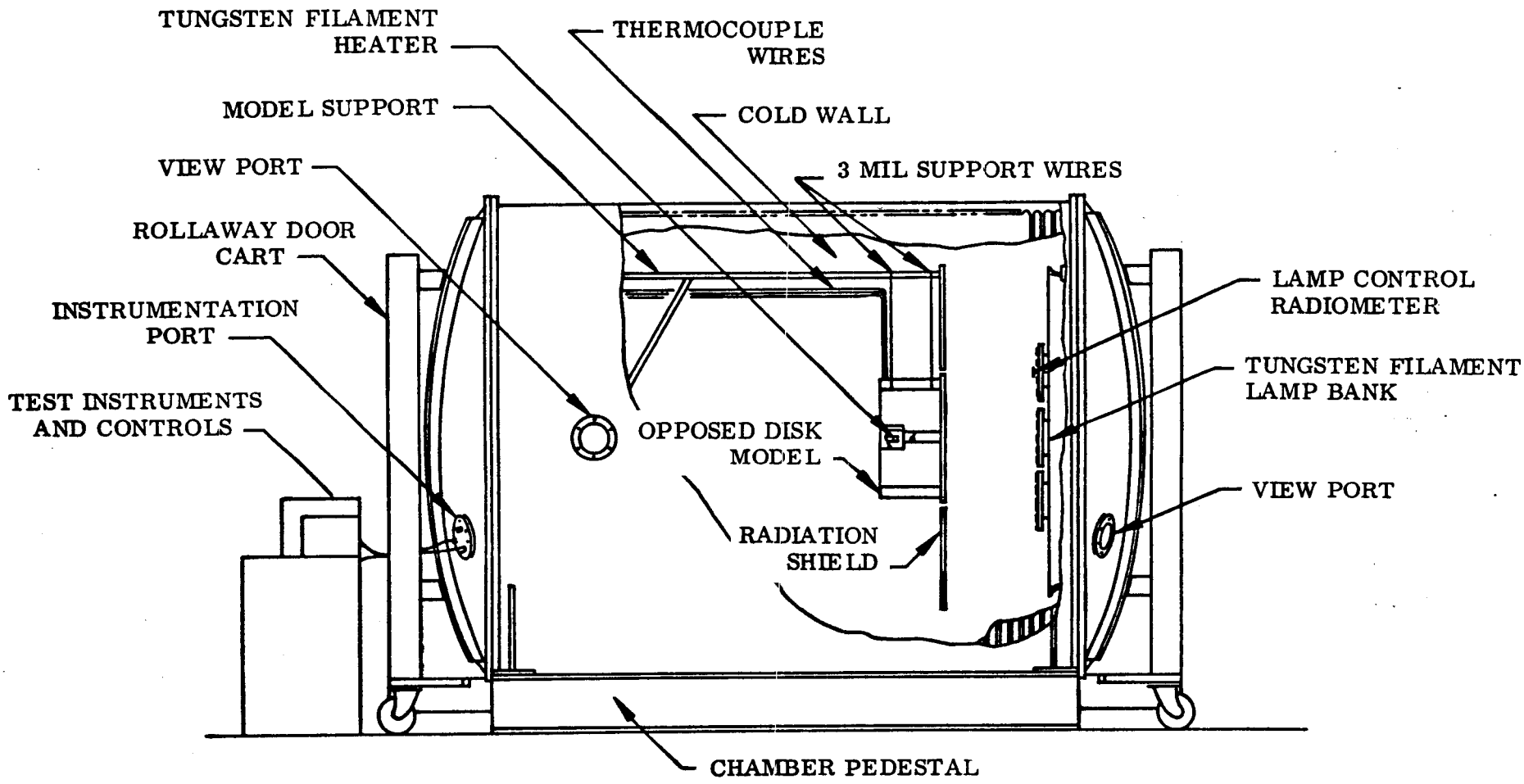

Fig. 8 Opposed Disk Mounted in Chamber

Transient tests used the same instrumentation with the addition of two more continuous recorders for observation of the transient thermocouple response.

Steady periodic conditions were assumed to be existent when adjacent peaks and valleys of the temperature histories were within $\pm 0.5°$ K. Normal operation required a minimum of 6 cycles to achieve this condition with a prototype period of 90 min. After steady periodic conditions were achieved, two complete cycles were recorded. The millivolt response was then reduced to time-temperature history and plotted in that form.

The internal heater was controlled by an on-off reset timer which could be adjusted to give a specified on time with an accuracy of 1 sec. The on portion of the cycle was initiated by a microswitch that was actuated by a cam on the lamp bank controller. For steady state runs the heater was controlled manually. Heater energy levels were set by manual adjustment of a powerstat in parallel with the heater circuit. Power levels were measured with a laboratory precision null voltmeter, Fluke model 803B, with a sensitivity of 10 μV and 30 μV accuracy. Voltage was read directly and current determined by measurement of voltage drop across a 0.025 ohm 0.1 percent precision resistor placed in series with the heater coil. The overall accuracy of the power determination was estimated as 1.0 percent with uncertainties associated primarily with lead losses and voltage transients.

Incident energy was placed on the samples by a bank of quartz enclosed, reflector backed, tungsten filament lamps. The lamp bank was mounted on the interior of the chamber door and controlled by an external power supply. Lamp intensity was varied by a Research Incorporated silicon controlled rectifier. For steady state operation, the lamp intensity was manually set by adjustment of the rectifier system. For transient conditions the lamp intensity was varied sinusoidally by a Research Incorporated Thermac feedback controller in conjunction with a sine wave generator fabricated for use on this program.

Operation of the feedback controller required input signals to the controller from a sine wave generator and from a lamp monitoring detector. The sine wave generator for the opposed disk tests was fabricated from a four revolution per hour timer motor, two perpendicular disks, a rack and gear assembly, and a single turn 100-ohm precision linear potentiometer. The general arrangement of these components is shown in Fig. 9. Adjustment of the cycle period was accomplished by placement of the motor in relation to the axis of the driven disk. While this arrangement resulted in excellent sine wave generation, it was difficult to adjust and was used only for the first phase tests.

Establishment of required incident flux levels was accomplished through careful calibration of the system as a function of lamp bank supply voltage. This calibration gave incident flux as a function of voltage, lamp monitor output, and response of two calorimeter detectors placed in the sample plane. This information was then used to set the gain of the power controller such that desired maximum and minimum signal levels were achieved. Following this procedure a scan of the sample plane was made with a hemispherical asymptotic foil calorimeter to determine the distribution of energy throughout the sample test plane. The calibration layout and bank arrangement are shown in Fig. 10 for the full-scale case. The results of the calibration and spatial distribution are shown in Figs. 11 and 12.

The procedures described above for the prototype were also followed for each of the smaller scale models. The instrumentation, chamber installation, thermocouple calibration, lamp calibration, operating controls, data recording, and data reduction procedures were similar. The major change required in performing the small-scale tests was a rearrangement of the lamp bank so that required levels of energy were available at the sample test plane. For the quarter-scale model, this change was small since the model had a required flux ratio of unity. This was achieved by moving the lamps closer together and removing some of the individual elements of the bank. For the half-scale model it was more difficult since the required flux ratio was 1.63. This was obtained by use of all 15 lamps and moving the sample in closer to the bank. Since only a uniform intensity over the test plane was required, it was possible to

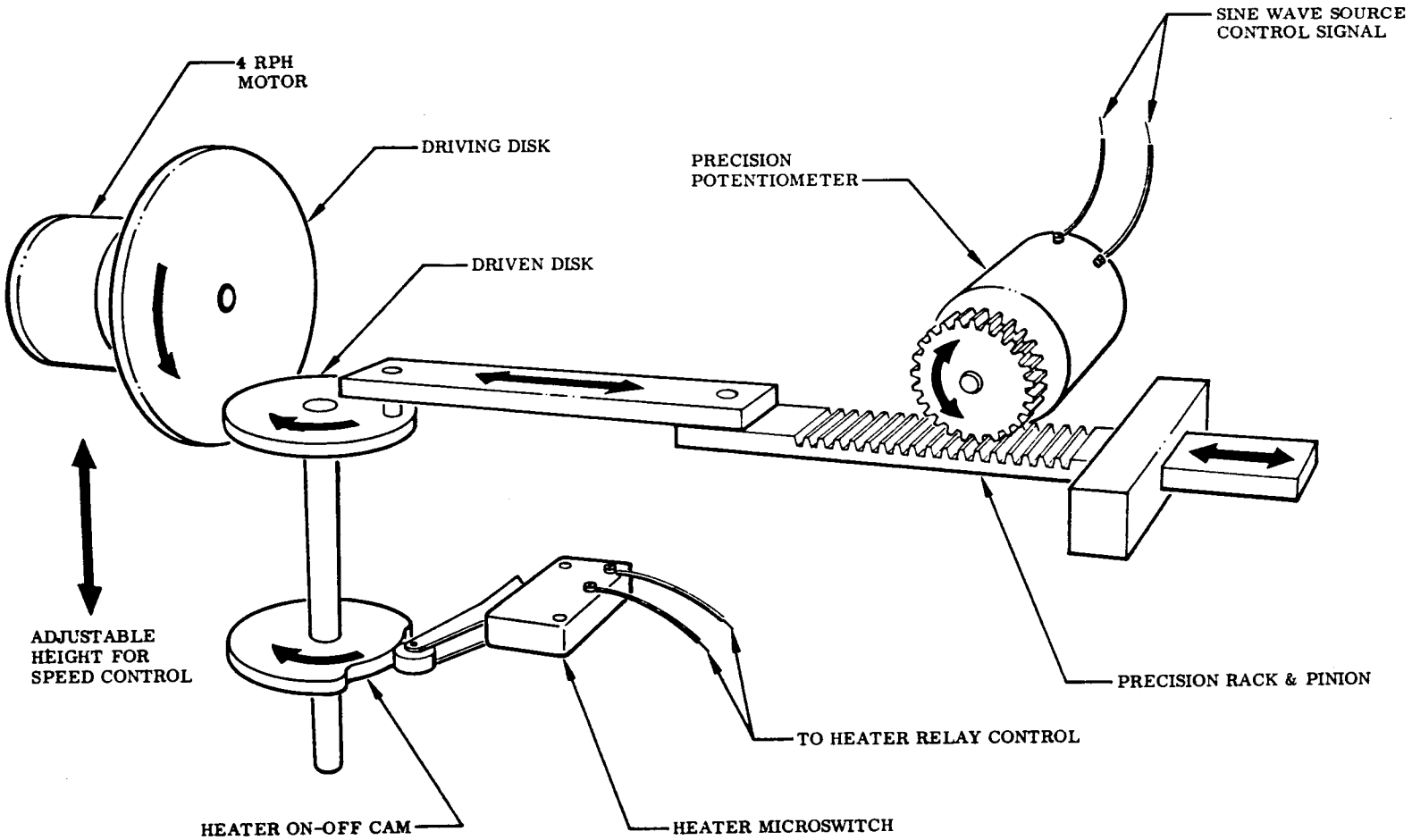

Fig. 9 Sine Wave Generator for Opposed Disk Tests

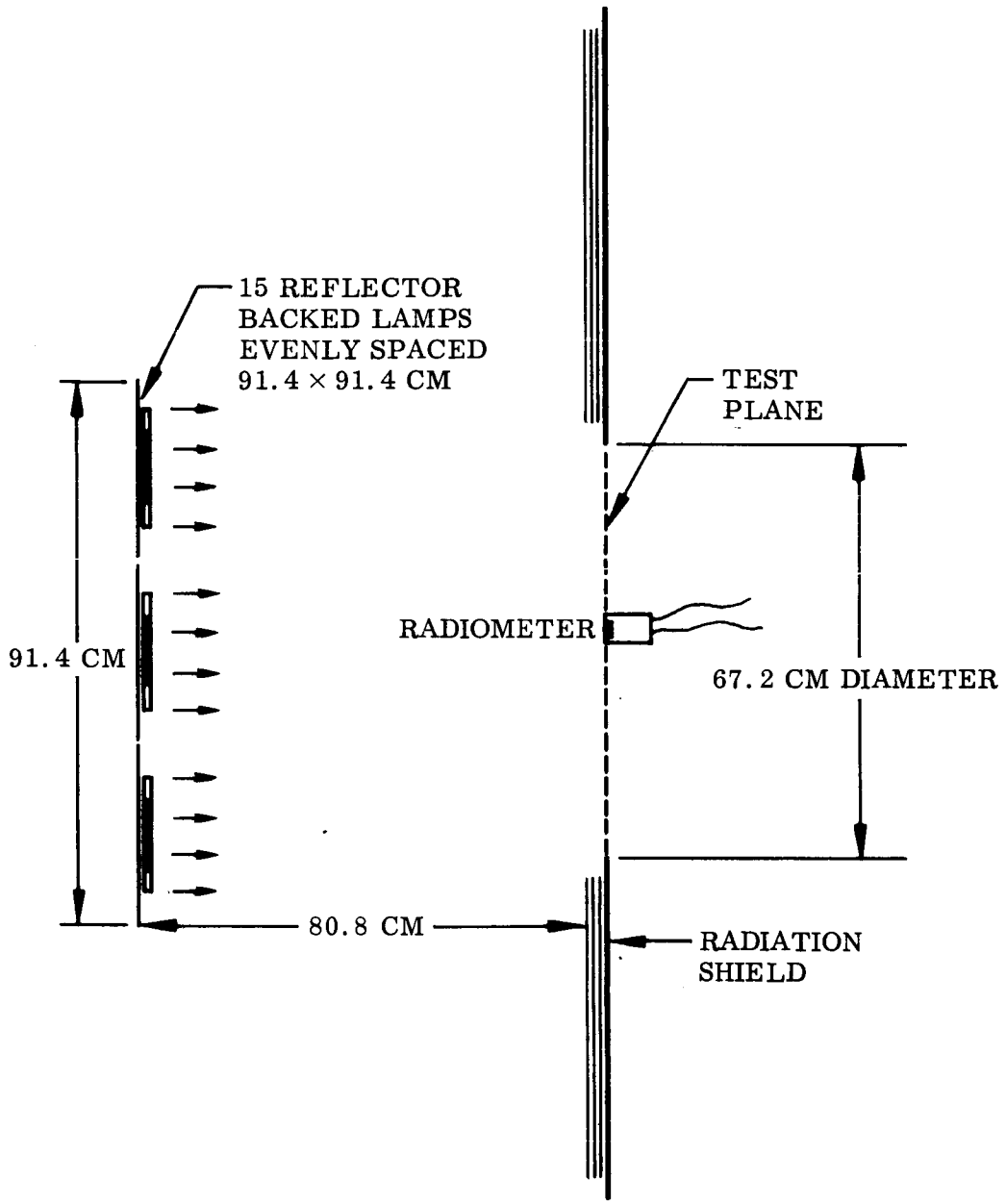

Fig. 10 Chamber Source Calibration Arrangement

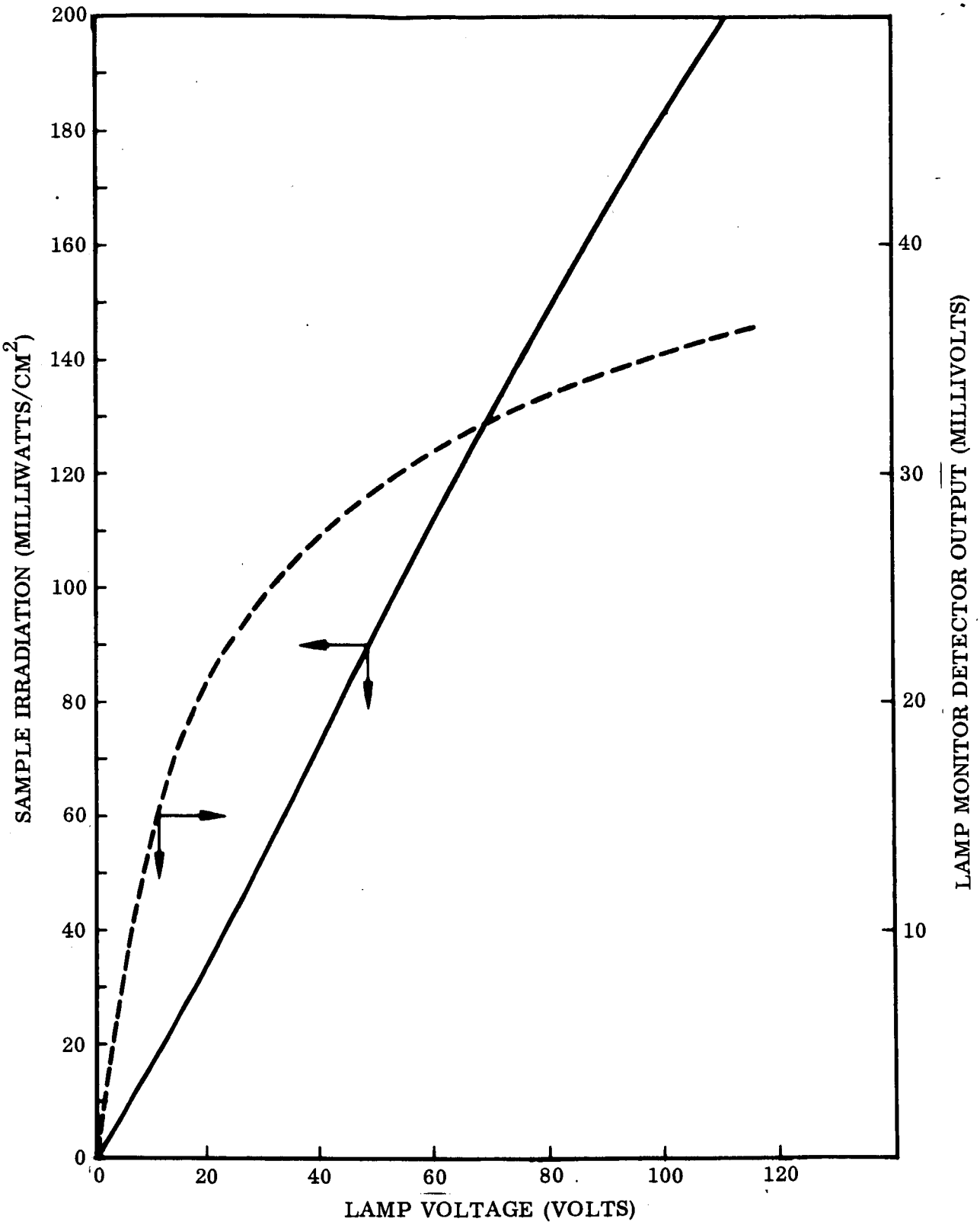

Fig. 11 Source Calibration

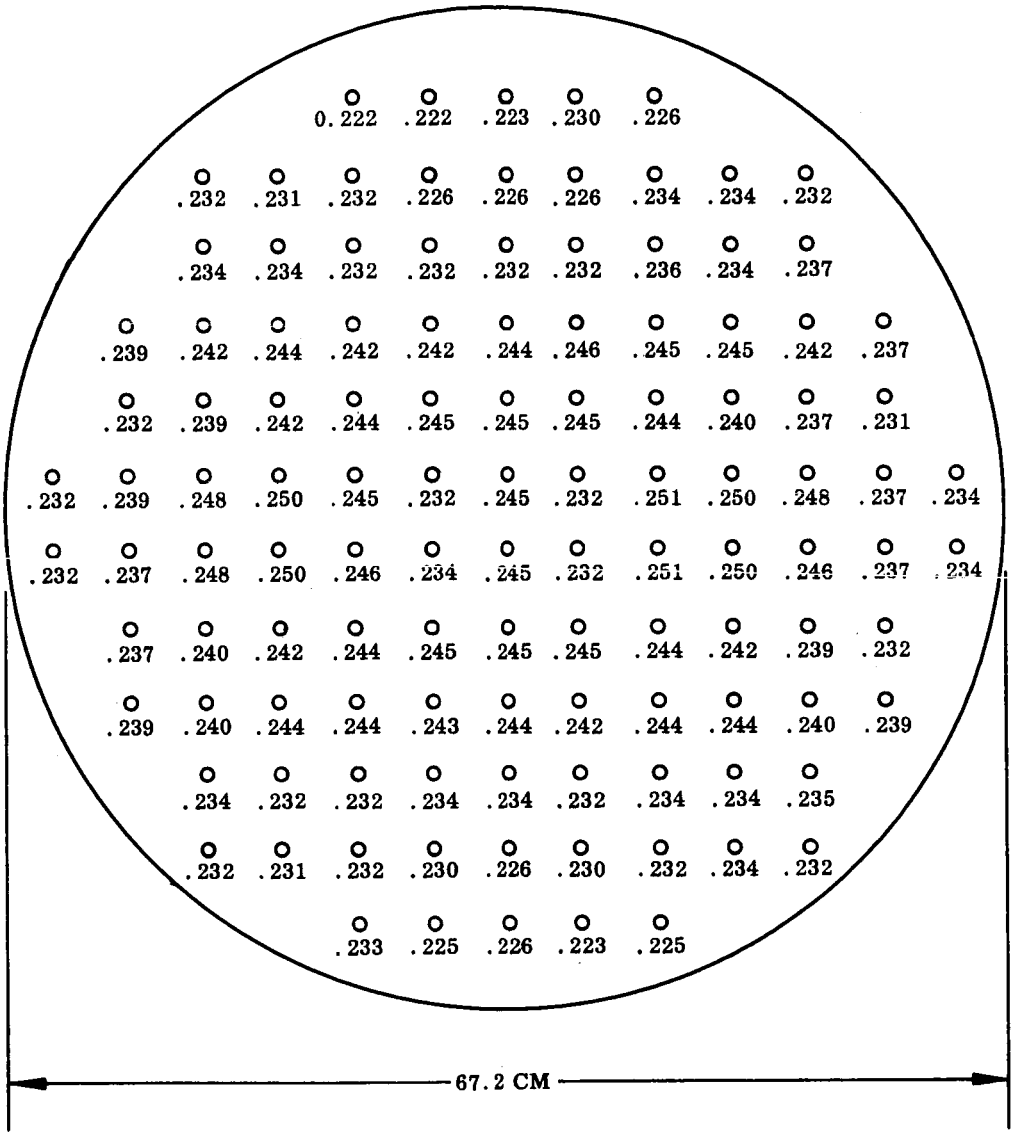

Fig. 12 Energy Distribution in Watts/cm^2 for Lamps at 115 Volts

ignore geometric similarity of the bank itself. As will be seen later this was not possible in the truncated cone test arrangements.

Tests were run on all three sizes for steady state and transient conditions. Steady state runs were made with the heater on and off and the lamp bank providing a constant flux. Transient runs were made with the incident energy varied sinusoidally over a specified period while the internal heater was actuated for a specified duration at a given time during the period. The test conditions are presented in Table 5.

Table 5

OPPOSED DISK TEST CONDITIONS

Model Size	Incident Flux ($Watts/cm^2$)				Internal Heater Power (Watts)		
	Steady State	Transient			Steady State	Transient	
		Max.	Min.	Period (min)		Max.	Time On (min)
Full	0.127	0.192	0.063	87	95.8	95.8	20
Half	0.209	0.314	0.103	18.3	35.0	34.8	4.4
Quarter	0.129	0.194	0.065	85.79	6.7	6.6	19.7

Difficulties were encountered in the half- and quarter-scale tests due to loss of heater filaments. These filaments were initially designed on the basis of required power levels and the desire to maintain geometric conformity of the filament size with respect to the box enclosure. This approach provided filaments that were small and that had to be operated at high temperatures. This resulted in loss of the filaments before the test series could be completed. The tests then had to be shut down, new filaments of a heavier design installed, and the tests repeated. The use of heavier filaments provided lower filament temperatures and longer life but also introduced relative geometries between the filament and box enclosure that were not identical.

3.3.3 Truncated Cone Test Conditions

After fabrication, instrumentation, and assembly of the truncated cone prototype and models, they were installed in the vacuum chamber by suspension with 3-mil support wires. Operational checks were then performed and calibration procedures similar to those described for the opposed disks were completed. Figure 13 shows the half-scale model on its support framing. Figure 14 indicates the overall chamber installation.

These models were all suspended from a rotating mechanism which permitted changes in orientation of the cone with respect to the lamp bank. This mechanism was driven by a small electric motor which was actuated from the chamber exterior. Orientation of the test specimen with an accuracy of two circular degrees was provided by a scale on the suspension system that could be viewed through chamber view ports.

Radiant energy was again supplied by the bank of tungsten filament lamps. However, for this test series a frontal shield was not used. The bank was initially arranged for the prototype tests to give required amounts of energy at reasonable voltage levels. After a number of adjustments it was found that the most desirable arrangement was the same as that previously specified for the full-scale tests of configuration A. The bank was calibrated using an Eppley hemispherical radiometer, two thumbtack stem calorimeters, four button calorimeters, and an asymptotic calorimeter. These instruments were distributed throughout the plane occupied by the large end of the cone when it was directly facing the bank. The resulting calibration was identical to that presented in Fig. 9 which was obtained for the same lamp arrangement during the first test series. For this relative geometry between the lamps and sample, the energy is not uniformly distributed over the sample when either the side or small cone end is facing the bank. In these cases the energy received depends upon the shape factor between each point on the surface and the portion of the bank illuminating that area. Therefore, the relative geometry between the lamp bank and specimen had to be preserved for the small-scale tests. It was also necessary that identical filament temperatures be used for the small-scale tests to provide the same degree of absorbed energy.

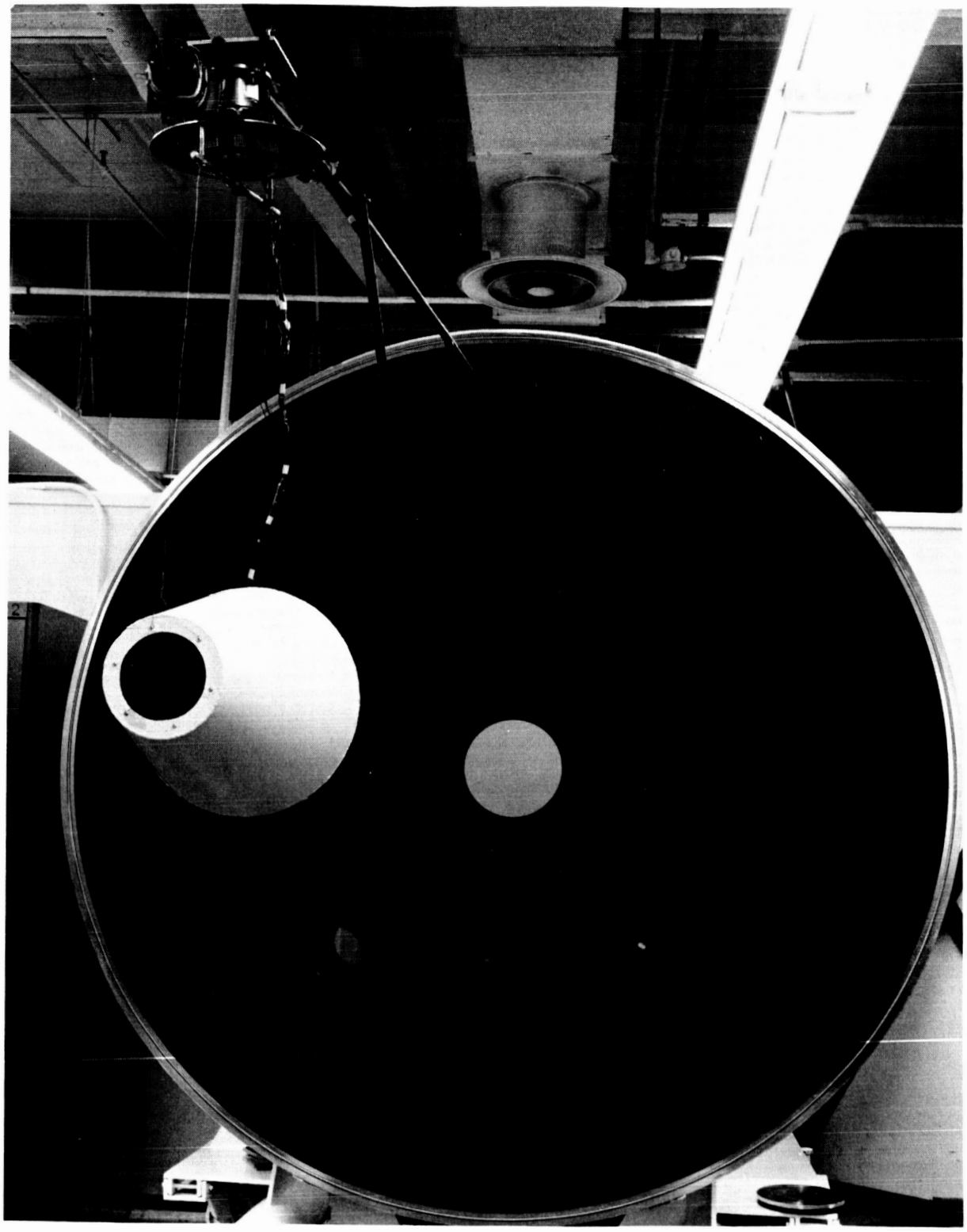

Fig. 13 Half-Scale Truncated Cone on Support Framing

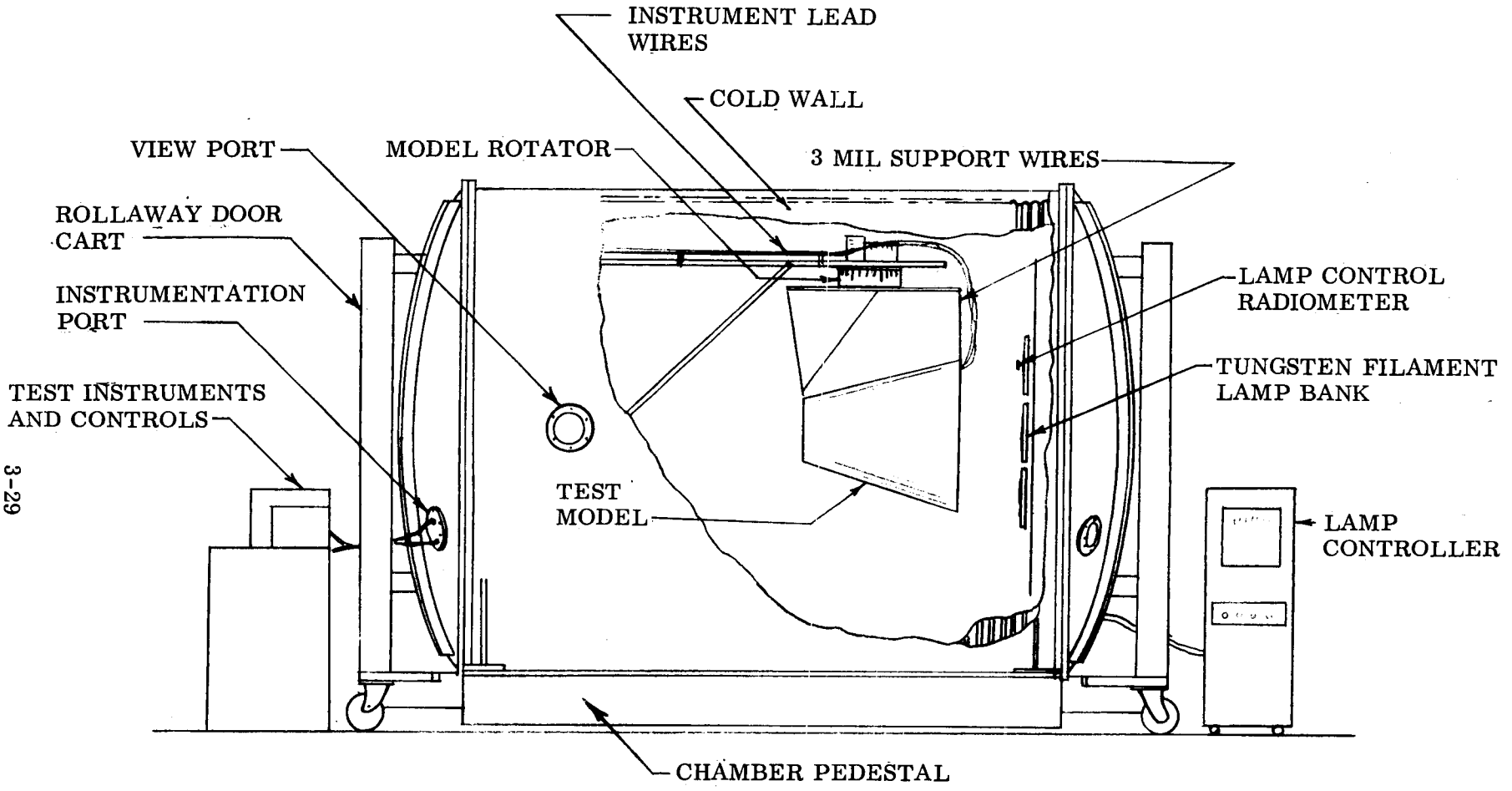

Fig. 14 Chamber Installation

The requirements of identical relative geometry and duplication of spectrum were met for the models by rearrangement of the bank followed by repetition of the calibration procedures. For the half-scale model, it was found that the bank could be compressed, the reflectors removed, and the number of lamps reduced, to provide the required conditions. For the quarter-scale model it was not possible to provide the proper irradiation using direct illumination from the lamps. In this case it was necessary to fabricate a special aluminum shield in the shape of the required bank, illuminate the shield uniformly with two reflector backed lamps, and direct this radiation to the sample plane. Considerable effort was required to achieve the proper source arrangement; however, calibration of the final approach established that this condition was satisfactory. The special arrangements provided flux levels at the sample plane in direct accordance with the model criteria.

Control of the lamp bank for this series of tests was again through use of the Thermac temperature controller. However, the mechanical sine wave generator previously used for transient control was replaced by a card programmer which gave much more accurate control over the required flux levels. The feedback signal to the controller was again supplied by a radiometer facing the lamps.

The internal heaters were controlled by individual variacs which were turned on and off by relays in the card programmer. The relays were thrown by a signal from the card and gave precise regulation of both heater initiation and duration of the cycle. For transient runs, the enclosed heater was started 15 min before the peak of external irradiation and run for 15 min. It was then shut off and the open heater started for its 15-min cycle. In this manner the heaters were interchanged precisely at the peak of the illumination. This was repeated throughout the transient run. For the half-scale run, the heating period was shortened by the required time scale. Steady state runs were made with the heaters both on or both off until steady temperatures were achieved. The criterion for steady state was again set as less than 0.5° K/hr temperature drift. Heater dissipation rates were measured using the same instrumentation as that used for the first test series.

Steady state runs were made for three positions of the cone. These were for the large end facing the lamps, the small end facing the lamps, and the side facing the lamps such that the horizontal center line of the cone was in a plane parallel to the plane of the lamp bank. In each position data were taken with the lamps furnishing constant external flux and the internal heaters both on or both off.

Transient runs were made for the large end and small end facing the lamps. The side facing position was not used for the transient runs as it would not have furnished any additional useful information over that gained from the two conditions actually used.

Steady state conditions were observed on continuously recording instrumentation until constant thermal levels were obtained. The thermocouple output was then read out point by point. A precision digital voltmeter was used for this test series in place of the portable potentiometer. This voltmeter was an Electro Instruments Model 4010 with a Model A-1415-C preamplifier. The two units provide a sensitivity of 1 μV and 3 μV calibrated accuracy. All thermocouples were read and recorded twice to minimize operator error. Transient conditions were observed until a steady periodic condition was achieved and the data then recorded on multipoint and continuous recorders. Lamp irradiation, model irradiation, thermocouple response, heater operation and dissipation, and chamber operation were all continuously recorded during the two data taking cycles.

Difficulties were again encountered in obtaining reliable operation from the internal heaters; however, the difficulties were not due to any single cause. The filaments were constructed from 500-Watt filaments and were not lost due to burnout of the filament but rather from failure or shorting of the leads. These problems were corrected as they became apparent and caused only brief delays in the test program.

Test conditions for the steady state and periodic runs are given in Table 6. All flux levels in the table are those measured in the frontal plane with the cone large end facing the lamp bank. Rotation placed the small end in this same plane.

Table 6

TRUNCATED CONE TEST CONDITIONS

Model Size	Incident Flux (Watts/cm^2)				Internal Heater Power (Watts)[a]					
	Steady State	Transient			Steady State		Transient			
							Open		Enclosed	
		Max.	Min.	Period (min)	Open	Enclosed	Power	Period (min)	Power	Period (min)
Full	0.129	0.195	0.064	90	84.0	10.3	92	15	10.3	15
Half	0.210	0.316	0.0[b]	19.8	29.9	35.6	32.5	3.3	36.0	3.3
Quarter	0.129	0.195	0.063	90	5.55	6.80	5.7	15	7.2	15

(a) Heater power varied ±3% between runs. Value given is average.
(b) Lamp source shut off to zero power during transient run due to controller response.

3.4 RESULTS

3.4.1 Opposed Disk Test Results

Steady state results for the opposed disks are presented in Tables 7 and 8 for measurements on all three test objects. Measured temperatures are reported in degrees Kelvin for the prototype and both small-scale models. The model measurements were adjusted by the scaling criteria to give values for predicted prototype behavior. These predictions are compared to the measured prototype temperatures. The temperature difference ΔT and percent error $\Delta T/T\%$ both use the prototype temperature as a base condition.

An inspection of these results shows that the general prediction of prototype response was good with differences between prototype measurements and model predictions being on the order of 5° to 10° K. No general order of differences was noted, with both positive and negative values sharing equal weight in the results. Notable exceptions to a random behavior are thermocouple locations 38, 40, and 45. Thermocouple location 40 for both the half- and quarter-scale model predictions was high when

Table 7

STEADY STATE THERMAL RESPONSE OF OPPOSED DISKS WITH HEATER OFF[a]

Thermocouple Location	Thermocouple Number	Full	Half Scale				Quarter Scale			
		Measured	Measured on Model	Predicted for Prototype	ΔT	ΔT/T %	Measured on Model	Predicted for Prototype	ΔT	ΔT/T %
Small End Plate	34	258	294	257	-1	-0.4	253	261	3	1.2
	37	262	289	253	-8	-3.1	256	263	1	0.4
	36	262	300	262	0	0	250	258	-4	-1.5
	35	254	294	258	4	1.6	246	254	0	0
	46	258	294	257	-1	-0.4	251	258	0	0
Leg	38	277	321	281	4	1.4	268	277	0	0
Heater Box	44	261	(b)	—	—	—	251	258	-3	-1.1
	45	261	296	259	-2	-0.8	252	260	-1	-0.4
Large End Plate	39	300	342	300	0	0	292	302	2	0.7
	40	299	350	307	8	2.7	301	311	12	4.0
	41	303	336	297	-6	-2.0	289	298	5	1.6
	42	303	343	301	-2	-0.7	296	304	1	0.3
	43	305	344	302	-3	-1.0	302	312	7	2.3
				Maximum	8	-3.1		Maximum	12	4.0
				Numerical Average	-0.6	-0.23		Numerical Average	1.8	0.58

(a) Temperature in °K.
(b) Data not available. Thermocouple failed during test.

Table 8

STEADY STATE THERMAL RESPONSE OF OPPOSED DISKS WITH HEATER ON[(a)]

Thermocouple Location	Thermocouple Number	Full	Half Scale				Quarter Scale			
		Measured	Measured on Model	Predicted for Prototype	ΔT	ΔT/T %	Measured on Model	Predicted for Prototype	ΔT	ΔT/T %
Small End Plate	34	307	355	303	-4	-1.3	298	307	0	0
	37	311	353	303	-8	-2.6	298	308	-3	-1.0
	36	303	364	312	9	3.0	293	302	-1	-0.3
	35	305	365	313	8	2.6	294	303	-2	-0.7
	46	326	386	331	4	1.2	315	324	-2	-0.6
Leg	38	299	363	318	19	6.4	294	303	4	1.3
Heater Box	44	334	–	–	–	–	328	339	5	1.5
	45	336	399	350	14	4.2	329	339	3	0.9
Large End Plate	39	316	362	318	2	0.6	308	317	1	0.3
	40	313	367	322	9	2.9	314	323	10	3.2
	41	319	357	313	-6	-1.9	304	313	-6	-1.9
	42	317	361	317	0	0	316	325	8	2.5
	43	319	362	318	-1	-0.3	317	327	6	1.9
				Maximum	19	6.4		Maximum	10	3.2
				Numerical Average	3.8	1.2		Numerical Average	1.8	0.55

(a) Temperature in °K.

compared to the prototype response. This must be assumed to be due to a large measurement error on the prototype. For locations 38 and 45, the half-scale model, with heater on, predicted high temperatures. The model was closely examined after the tests to determine some reason for the high readings. No logical source of error in construction, thermocouple installation, or thermocouple response was found.

The average ΔT and $\Delta T/T\%$ are based on a numerical sum of values in each column and provide a measure of overall comparison between the measured and predicted prototype response. Some indication of the accuracy of the test procedure can be gained from these average values. For the half-scale model "heater on" test, it appeared that the energy supplied to the heater was not well distributed through the rear plate causing an overall temperature increase in that region. This apparently resulted in a high average temperature for that test. The remainder of the tests provided average prediction errors that were well within the accuracy of the test procedures used and indicate no strong trends toward high or low temperatures.

The transient results are presented in Figs. 15 through 20. Figure 15 presents the prototype response at thermocouples located at critical points of the test object for one complete cycle. The lamp detector output is also shown to give an indication of the phase relation between front plate temperatures and incident energy rates. The test conditions caused thermal gradients between the front and rear plate of approximately 40° K, and a change in heater box temperature of 53° K due to heater dissipation. Figures 16 through 20 present the prototype and predicted prototype temperatures for individual thermocouple locations. In general, the predictions were in good agreement with the prototype temperatures with prediction errors being on the same order as those observed for the steady state runs. Agreement at any time was within 10° K for thermocouples 37, 38, 39, and 43. Thermocouple 45 produced quite different results. On the half-scale model a large prediction error was observed for the front of the heater box. The quarter-scale model produced a reasonable prediction for this same location. (Inspection of the steady state data for this thermocouple location shows a high value for the half-scale model.) This variable behavior is attributed to the difficulties encountered in fabricating and installing heaters with the same relative geometry

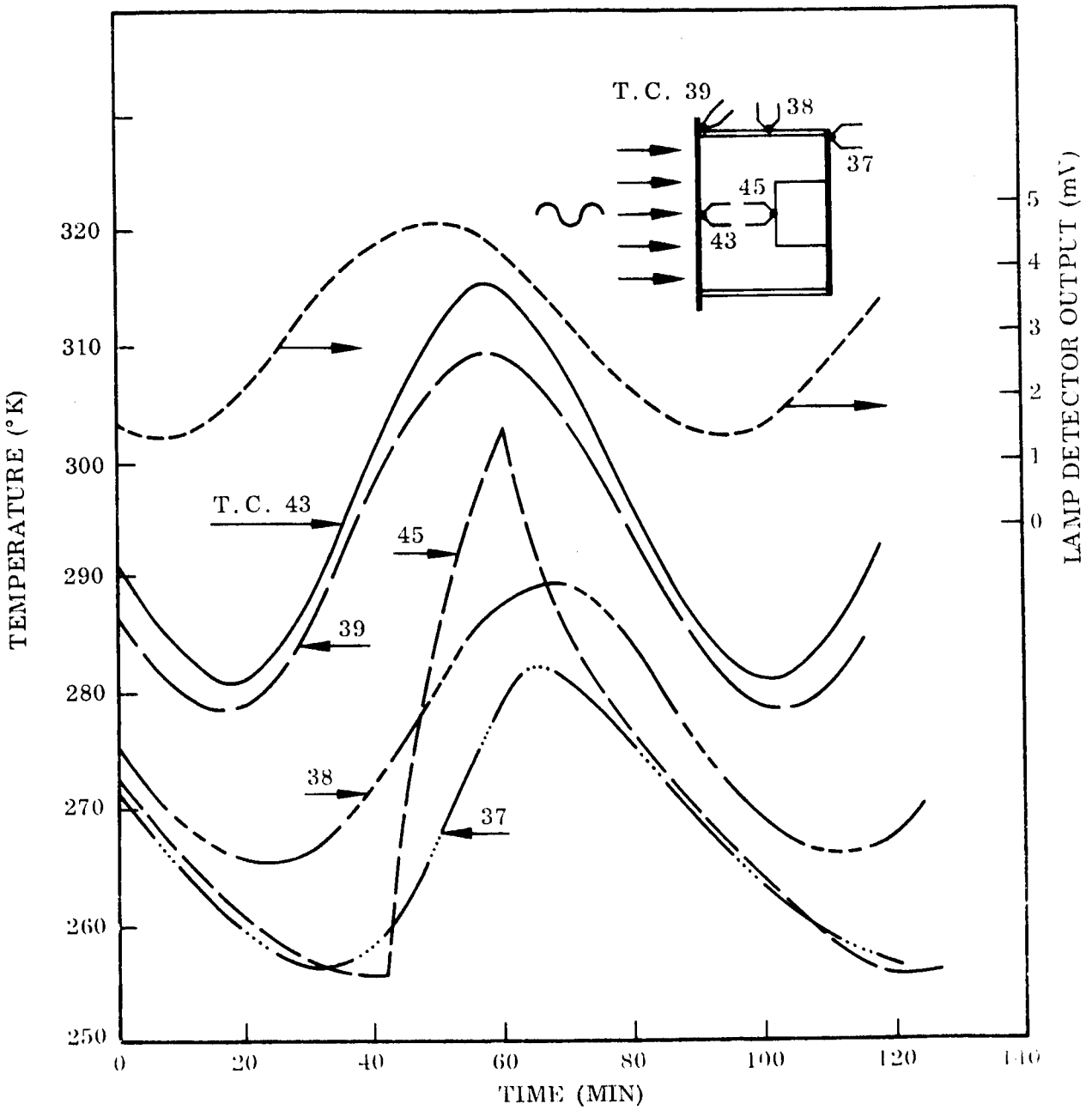

Fig. 15 Opposed Disk Prototype Response

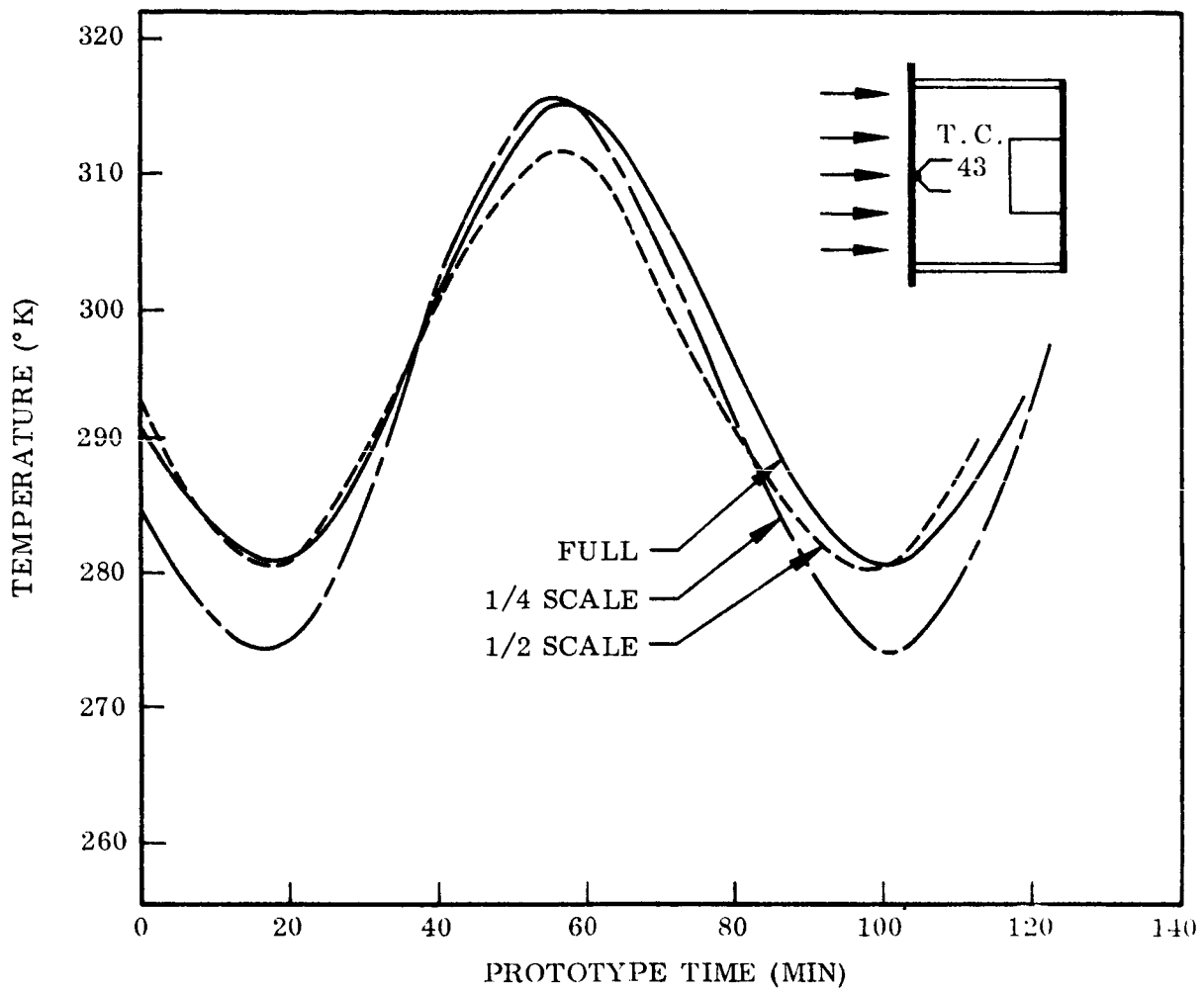

Fig. 16 Predicted and Measured Transient Temperatures for Center of Large End Plate

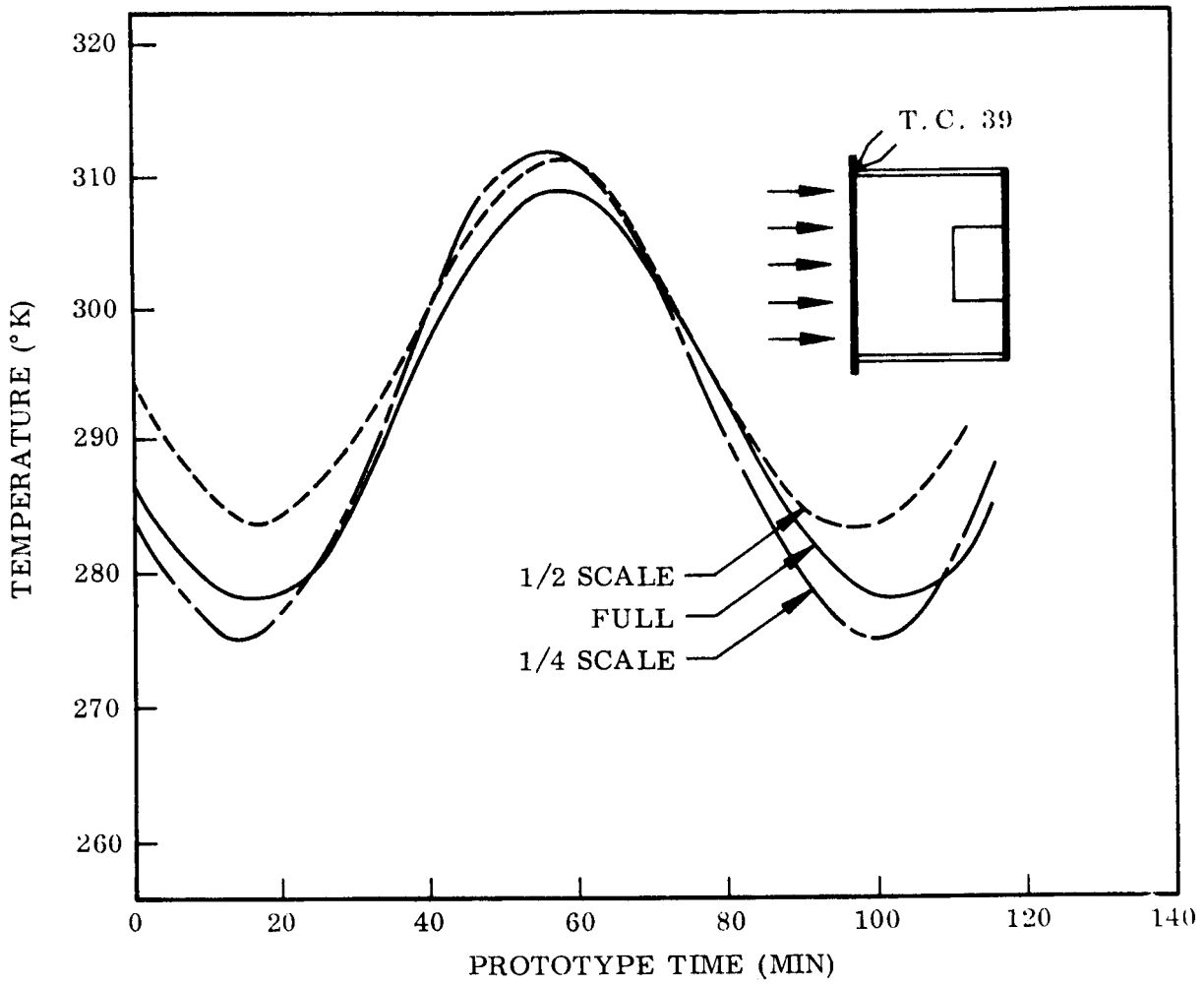

Fig. 17 Predicted and Measured Transient Temperatures for Edge of Large End Plate

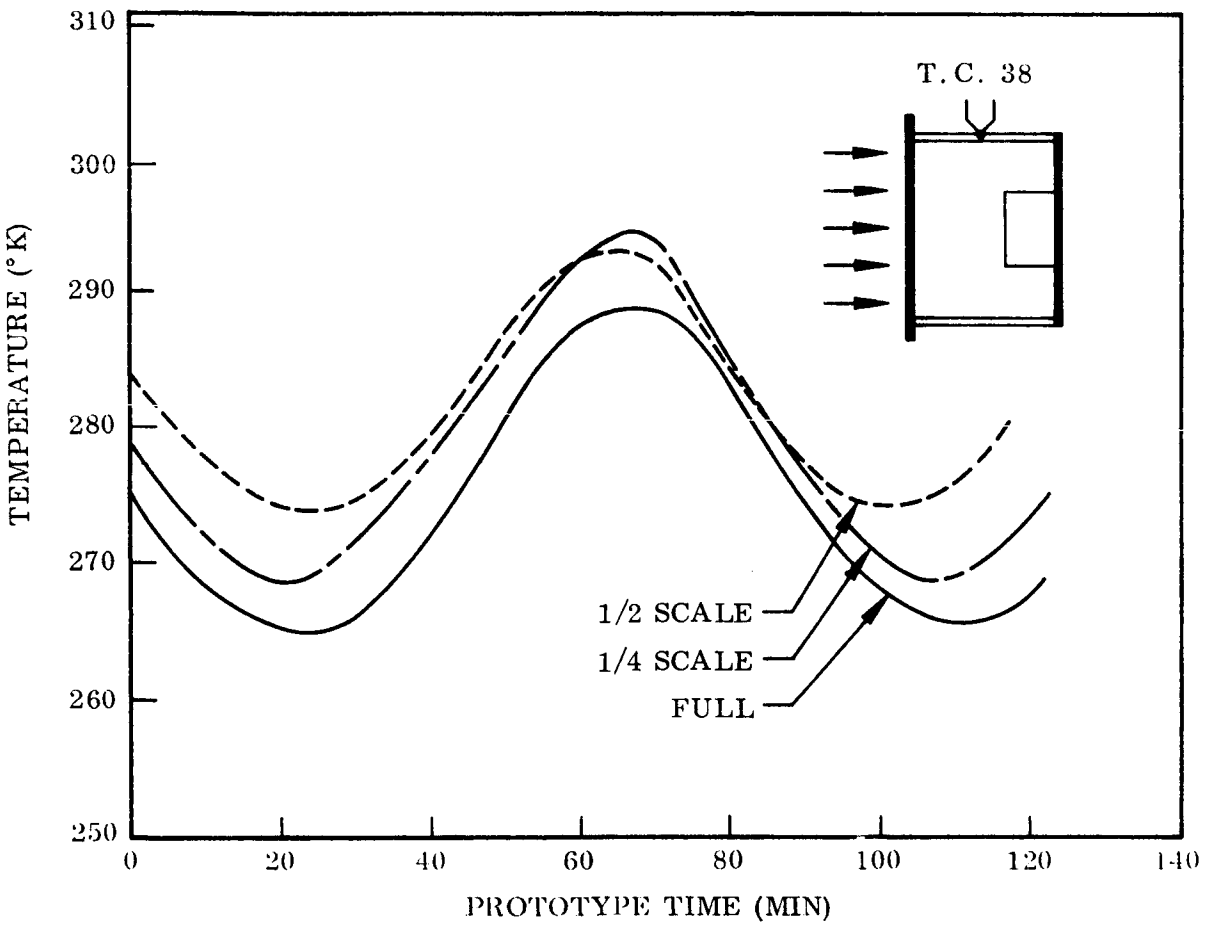

Fig. 18 Predicted and Measured Transient Temperatures for Middle of Support Leg

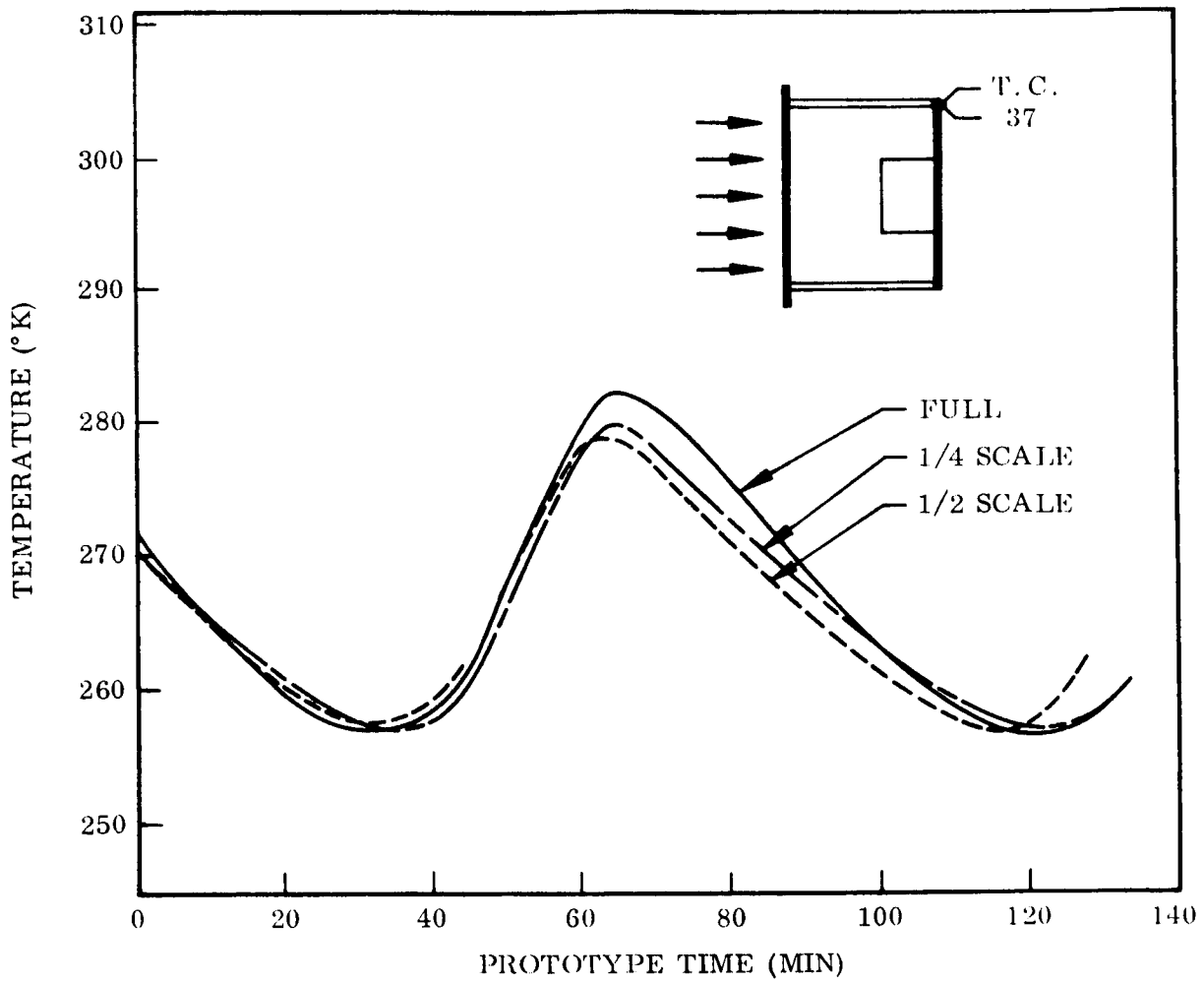

Fig. 19 Predicted and Measured Transient Temperatures for Edge of Small End Plate

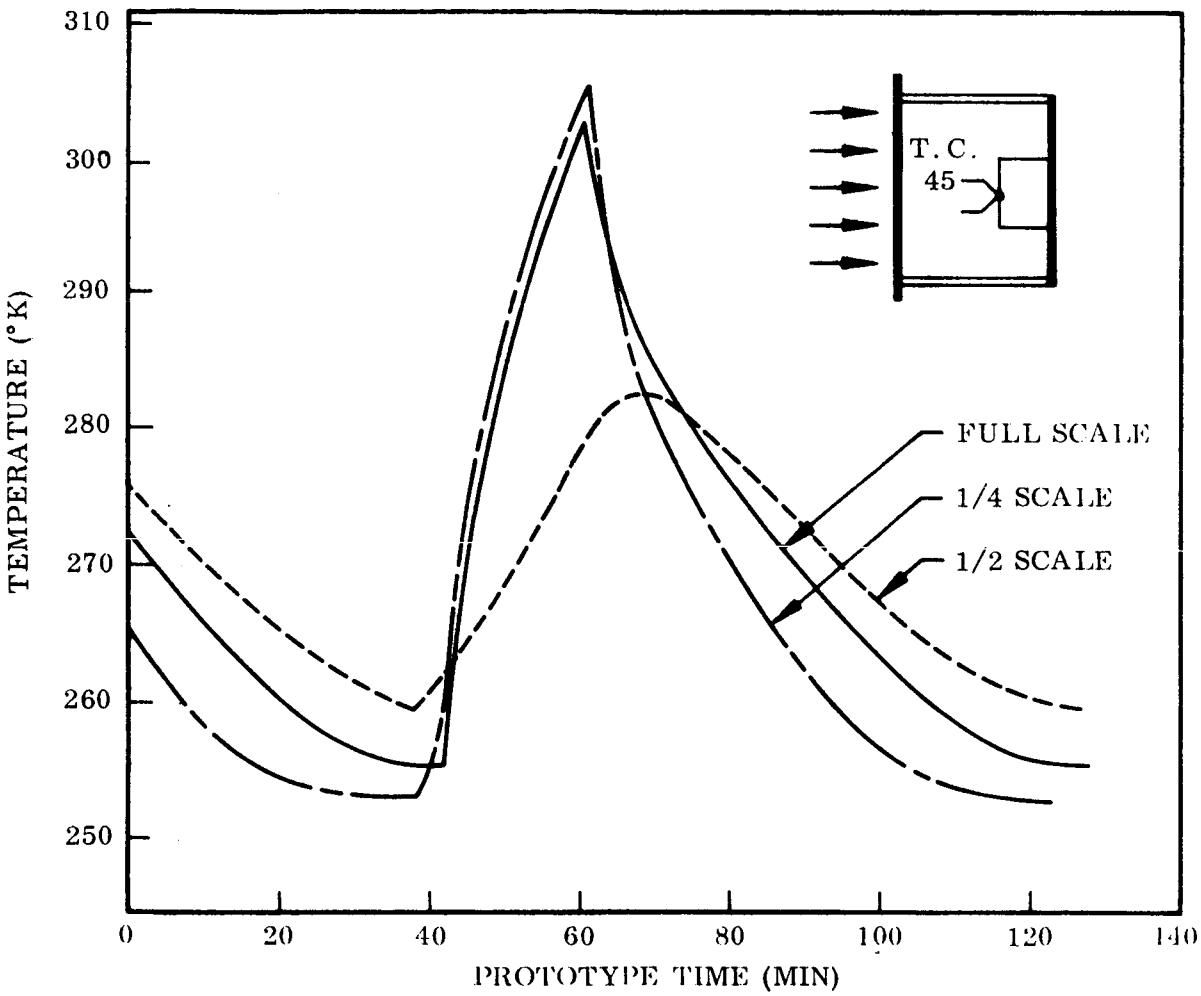

Fig. 20 Predicted and Measured Transient Temperature for Heater Box

between the heater coil and the box. A portion of the error may also be due to changes of surface absorptance of the box interior caused by deposition of tungsten oxide. These effects would be considerably amplified during the transient runs since a limited time exists for complete distribution of the dissipated energy through the box and its mounts.

It should be noted that the periodicity of the half-scale predictions is not in direct agreement with that observed for the prototype. This was due in part to difficulties encountered in accurate control of lamp cycles. As shown in Table 5, the period used for the half-scale test was 18.3 min while the proper period for correct prediction would have been 19.1 min. This resulted in a predicted prototype period that was too short by 3 min and 47 sec. In spite of this error in operating conditions, the predicted prototype response taken from the half-scale results was in good agreement with measured prototype behavior.

3.4.2 Configuration C Results

Results for the steady state runs on configuration C are presented in Tables 9 through 11 for heaters off and in Tables 12 through 14 for heaters on. The tables indicate the general location of the thermocouples, measured absolute temperatures, predicted prototype temperatures, and the differences in absolute values obtained from prototype tests and predictions. The error in each predicted temperature was computed using the prototype temperature as a base condition. For both heater conditions on the cones the maximum and numerical average errors were approximately the same. The magnitude of the maximum error was considerably reduced below that experienced in the configuration A test series. The results also indicate that the location having the largest error for one test condition was not necessarily the same as the location of largest error for other conditions. This behavior leads to the assumption that prediction errors were more attributable to model design and random experimental error than they were to thermometry.

Table 9

STEADY STATE THERMAL RESPONSE OF TRUNCATED CONE WITH HEATERS OFF, SMALL END FACING LAMPS[a]

Thermocouple Location	Thermocouple Number	Small End Illuminated								
		Full	Half Scale				Quarter Scale			
			Measured	Predicted	ΔT	ΔT/T%	Measured	Predicted	ΔT	ΔT/T%
Small End Plate	1	277	314	278	1	0.4	277	277	0	0
	2	277	313	277	0	0	275	275	-2	-0.7
	0	272	307	272	0	0	274	274	2	0.7
	18	271	307	272	1	0.4	274	274	3	1.1
	19	271	309	273	2	0.7	273	273	2	0.7
	20	269	305	270	1	0.4	275	275	6	2.2
Legs	14	257	292	258	1	0.4	257	257	0	0
	15	257	290	261	4	1.6	258	258	1	0.4
	4	230	263	233	3	1.3	233	233	3	1.3
	16	229	262	232	3	1.3	232	232	3	1.3
	11	209	236	209	0	0	209	209	0	0
	17	209	236	209	0	0	209	209	0	0
Heater Box	3	231	262	232	1	0.4	233	233	2	0.9
Large End Plate	5	198	226[b]	200[b]	2	1.0	202	202	4	2.0
	7	199	225	200	1	0.5	201	201	2	1.0
	9	197	224	199	2	1.0	200	200	3	1.5
	10	196	225	200	4	2.0	201	201	5	2.6
	8	200	227	201	1	0.5	202	202	2	1.0
	6	200	229	203	3	1.5	203	203	3	1.5
	12	202	229	203	1	0.5	207	207	5	2.5
	13	200	228	202	2	1.0	203	203	3	1.5
Skin	58	215	238	211	-4	-1.9	219	219	4	1.9
	59	215	245	216	1	0.5	217	217	2	0.9
	60	212	238	211	-1	-0.5	216	216	4	1.9
	61	216	238	211	-5	-2.5	222	222	6	2.8
			Maximum		-5	-2.5	Maximum		6	2.8
			Average		1.0	0.4	Average		2.5	1.2

(a) Temperature °K.

(b) T.C. No. 5 on half-scale model was not identically located geometrically with respect to prototype.

Table 10

STEADY STATE THERMAL RESPONSE OF TRUNCATED CONE WITH HEATERS OFF, SIDE FACING LAMPS[a]

Thermocouple Location	Thermocouple Number	Side Illuminated								
		Full	Half Scale				Quarter Scale			
			Measured	Predicted	ΔT	ΔT/T%	Measured	Predicted	ΔT	ΔT/T%
Small End Plate	1	215	247	218	3	1.4	220	220	5	2.3
	2	213	243	216	3	1.4	218	218	5	2.3
	0	216	247	219	3	1.4	220	220	4	1.9
	18	220	255	225	5	2.3	228	228	8	3.6
	19	215	248	219	4	1.9	219	219	4	1.9
	20	213	241	213	0	0	215	215	2	0.9
Legs	14	219	250	221	2	0.9	223	223	4	1.8
	15	215	244	216	1	0.5	218	218	3	1.4
	4	229	250	221	-8	-3.5	222	222	-7	-3.1
	16	215	244	216	1	0.5	218	218	3	1.4
	11	221	246	216	-5	-2.3	221	221	0	0
	17	214	238	211	-3	-1.4	212	212	-2	-0.9
Heater Box	3	217	244	216	-1	0.5	218	218	1	0.5
Large End Plate	5	219	234[b]	207[b]			217	217	-2	-0.9
	7	242	265	235	-7	-2.9	237	237	-5	-2.1
	9	215	240	213	-2	-0.9	214	214	-1	-0.5
	10	204	230	204	0	0	203	203	-1	-0.5
	8	231	254	225	-6	-2.6	230	230	-1	-0.4
	6	219	243	216	-3	-1.4	216	216	-3	-1.4
	12	220	243	216	-4	-1.8	220	220	0	0
	13	217	241	213	-4	-1.8	218	218	1	0.5
Skin	58	214	248	219	5	2.3	216	216	2	0.9
	59	192	224	198	6	3.1	194	194	2	1.0
	60	216	243	215	-1	-0.5	219	219	3	1.4
	61	276	316	279	3	1.1	280	280	4	1.4
			Maximum		-8	-3.5	Maximum		8	3.6
			Average		-0.3	-0.1	Average		1.2	0.5

(a) Temperature °K.
(b) T.C. No. 5 on half scale model was not identically located geometrically with respect to prototype.

Table 11

STEADY STATE THERMAL RESPONSE OF TRUNCATED CONE WITH HEATERS OFF, LARGE END FACING LAMPS[a]

Thermocouple Location	Thermocouple Number	Large End Illuminated								
		Full	Half Scale				Quarter Scale			
			Measured	Predicted	ΔT	ΔT/T%	Measured	Predicted	ΔT	ΔT/T%
Small End Plate	1	256	285	252	-4	-1.6	252	252	-4	-1.6
	2	251	280	248	-3	-1.2	251	251	0	0
	0	246	280	248	2	0.8	246	246	0	0
	18	252	284	252	0	0	249	249	-3	-1.2
	19	247	280	248	1	0.4	248	248	1	0.4
	20	250	282	250	0	0	251	251	1	0.4
Legs	14	274	307	272	-2	-0.7	275	275	1	0.4
	15	274	307	272	-2	-0.7	275	275	1	0.4
	4	308	341	302	-6	-1.9	306	306	-2	-0.6
	16	307	341	302	-5	-1.6	306	306	-1	-0.3
	11	326	366	324	-2	-0.6	326	326	0	0
	17	328	368	325	-3	-0.9	326	326	-2	-0.6
Heater Box	3	307	342	303	-4	-1.3	306	306	-1	-0.3
Large End Plate	5	323	369[b]	327[b]	4	1.2	319	319	-4	-1.2
	7	323	366	323	0	0	328	328	5	1.5
	9	326	368	325	-1	-0.3	323	323	-3	-0.9
	10	326	372	328	2	0.6	328	328	2	0.6
	8	332	377	333	1	0.3	337	337	5	1.5
	6	337	382	338	1	0.3	337	337	0	0
	12	341	385	341	0	0	(c)			
	13	340	384	340	0	0	340	340	0	0
Skin	58	236	268	237	1	0.4	243	243	7	3.0
	59	236	272	241	5	2.1	240	240	4	1.7
	60	234	269	238	4	1.7	241	241	7	3.0
	61	238	272	241	3	1.3	236	236	-2	-1.3
			Maximum		6	2.1	Maximum		7	3.0
			Average		-0.3	-0.07	Average		0.5	0.2

(a) Temperature °K.
(b) T.C. No. 5 on half-scale model was not identically located geometrically with respect to prototype.
(c) Thermocouple continuity lost – no reading.

Table 12

STEADY STATE THERMAL RESPONSE OF TRUNCATED CONE WITH HEATERS ON, SMALL END FACING LAMPS[a]

Thermocouple Location	Thermocouple Number	Small End Illuminated								
		Full	Half Scale				Quarter Scale			
			Measured	Predicted	ΔT	ΔT/T%	Measured	Predicted	ΔT	ΔT/T%
Small End Plate	1	318	356	315	-3	-0.9	316	316	-2	-0.6
	2	318	358	316	-2	-0.6	313	313	-5	-1.6
	0	309	346	306	-3	-1.0	305	305	-4	-1.3
	18	313	348	308	-5	-1.6	309	309	-4	-1.3
	19	(c)	348	308			309	309		
	20	309	350	310	1	0.3	310	310	1	0.3
Legs	14	(c)	354	313			319	319		
	15	323	362	320	-3	-0.9	322	322	-1	-0.3
	4	325	360	318	-7	-2.2	330	330	5	1.5
	16	352	394	348	-4	-1.1	349	349	-3	-0.9
	11	283	312	276	-7	-2.5	282	282	-1	-0.4
	17	288	321	284	-4	-1.4	285	285	-3	-1.0
Heater Box	3	380	421	373	-7	-1.8	382	382	2	0.5
Large End Plate	5	250	285[b]	250[b]	0	0	250	250	0	0
	7	251	282	250	-1	-0.4	251	251	0	0
	9	(c)	281	248			250	250		
	10	248	282	250	2	0.8	250	250	2	0.8
	8	258	287	254	-4	-1.5	257	257	-1	-0.4
	6	261	289	256	-5	-1.9	256	256	-5	-1.9
	12	262	294	260	-2	-0.8	(c)			
	13	261	293	259	-2	-0.8	263	263	2	0.8
Skin	58	246	283	250	4	1.6	251	251	6	2.4
	59	244	282	249	5	2.0	245	245	1	0.4
	60	247	282	249	2	0.8	245	245	-2	-0.8
	61	252	280	248	-4	-1.6	251	251	-1	-0.4
			Maximum		-7.0	-2.5	Maximum		6.0	2.4
			Average		-2.1	-0.7	Average		-1.4	-0.2

(a) Temperature ° K.
(b) T.C. No. 5 on half-scale model was not identically located geometrically with respect to prototype.
(c) Thermocouple continuity lost – no reading.

Table 13

STEADY STATE THERMAL RESPONSE OF TRUNCATED CONE WITH HEATERS ON, SIDE FACING LAMPS[a]

Thermocouple Location	Thermocouple Number	Side Illuminated								
		Full	Half Scale				Quarter Scale			
			Measured	Predicted	ΔT	ΔT/T%	Measured	Predicted	ΔT	ΔT/T%
Small End Plate	1	276	308	273	-3	-1.1	274	274	-2	-0.7
	2	272	305	270	-2	-0.7	272	272	0	0
	0	269	304	269	0	0	268	268	-1	-0.4
	18	278	312	276	-2	-0.7	278	278	0	0
	19	(c)	305	270			270	270		
	20	270	303	268	-2	-0.7	270	270	0	0
Legs	14	(c)	329	291			299	299		
	15	299	336	298	-1	-0.3	298	298	-1	-0.3
	4	323	359	318	-5	-1.5	328	328	5	1.5
	16	348	394	349	1	0.3	344	344	-4	-1.1
	11	294	323	286	-8	-2.7	288	288	-6	-2.0
	17	293	328	290	-3	-1.0	287	287	-6	-2.0
Heater Box	3	376	420	372	-4	-1.1	375	375	-1	-0.3
Large End Plate	5	264	289[b]	256[b]			258	258	-6	-2.3
	7	282	313	277	-5	-1.8	278	278	-4	-1.4
	9	(c)	294	260			258	258		
	10	254	289	256	2	0.8	250	250	-4	-1.6
	8	280	309	274	-6	-2.1	276	276	-4	-1.4
	6	270	301	267	-3	-1.1	265	265	-5	-1.9
	12	273	305	270	-3	-1.1	(c)			
	13	274	305	270	-4	-1.5	271	271	-3	-1.1
Skin	58	247	287	254	7	2.8	251	251	4	1.6
	59	235	268	237	2	0.9	232	232	-3	-1.3
	60	250	288	255	5	2.0	249	249	-1	-0.4
	61	300	344	304	4	1.3	304	304	4	1.3
			Maximum		-8	2.8	Maximum		-6	2.3
			Average		-1.4	-0.5	Average		-1.8	-0.6

(a) Temperature °K.
(b) T.C. No. 5 on half scale model was not identically located geometrically with respect to prototype.
(c) Thermocouple continuity lost – no reading.

Table 14

STEADY STATE THERMAL RESPONSE OF TRUNCATED CONE WITH HEATERS ON, LARGE END FACING LAMPS[a]

Thermocouple Location	Thermocouple Number	Large End Illuminated								
		Full	Half Scale				Quarter Scale			
			Measured	Predicted	ΔT	ΔT/T%	Measured	Predicted	ΔT	ΔT/T%
Small End Plate	1	296	329	291	-5	-1.7	289	289	-7	-2.4
	2	291	325	288	-3	-1.0	286	286	-5	-1.7
	0	285	322	285	0	0	280	280	-5	-1.8
	18	288	325	288	0	0	283	283	-5	-1.7
	19	(c)	323	286			283	283		
	20	288	326	288	0	0	288	288	0	0
Legs	14	(c)	356	315			321	321		
	15	322	365	323	1	0.3	321	321	-1	-0.3
	4	360	406	359	-1	-0.3	364	364	4	1.1
	16	379	443	383	4	1.1	376	376	-3	-0.8
	11	357	406	359	2	0.6	356	356	-1	-0.3
	17	358	411	364	6	1.7	357	357	-1	-0.3
Heater Box	3	401	455	403	2	0.5	404	404	3	0.7
Large End Plate	5	340	388[b]	344[b]	4	1.2	336	336	-4	-1.2
	7	341	389	344	3	0.9	348	348	7	2.0
	9	(c)	390	345			340	340		
	10	344	392	347	3	0.9	346	346	2	0.6
	8	353	402	356	3	0.9	356	356	3	0.9
	6	358	407	360	2	0.5	356	356	-2	-0.5
	12		411	364			(c)			
	13	363	412	364	1	0.3	361	361	-2	-0.6
Skin	58	265	305	271	6	2.3	269	269	4	1.5
	59	266	302	267	1	0.4	266	266	0	0
	60	267	306	271	4	1.5	269	269	2	0.7
	61	265	303	268	3	1.1	264	264	-1	-0.4
			Maximum		6	2.3	Maximum		7	-2.4
			Average		1.7	0.8	Average		-0.6	-0.2

(a) Temperature °K.
(b) T.C. No. 5 on half-scale model was not identically located geometrically with respect to prototype.
(c) Thermocouple continuity lost – no reading.

The average error listed for each test condition is based upon the numerical sum of all errors for the test and provides a measure of the accuracy of simulation of required internal and external energy levels. The results show that the heater off tests generally resulted in positive average errors while heater on tests resulted in negative average errors. This would indicate that excessive external energy and insufficient internal energy were used for the model tests. However, it is probably equally valid to assume the reverse to be the case during the prototype tests. The random distribution and small value of differences indicate no definite sources of error in design or operation of the models. The average absolute error for all half-scale predictions was 1.1 percent while for all quarter-scale tests it was 1.0 percent. These magnitudes are well within the experimental accuracy of the test procedures used and correspond to an average absolute temperature difference of 3° K. Such results lend considerable weight to arguments that thermal simulation techniques will produce reliable steady state data within the limits of laboratory test procedures.

The transient results for the cones are presented in Figs. 21 through 32 for two orientations of the sample to lamp bank. These orientations produced the largest temperature difference between the end plates and best demonstrate the accuracy of the models. Additional runs were made with the sides of the sample facing the lamp bank; however, the results obtained were not as demonstrative as those shown and indicated no additional difficulties in model prediction of prototype response. Figure 21 presents the thermal response at five thermocouple locations for the prototype tests with the small end facing the lamps. Twelve thermocouples were recorded but only five reported since these locations indicate the areas of greatest thermal fluctuation. The curves clearly show the steady periodic temperature cycle at each thermocouple location and indicate that a large temperature variation was achieved through the length of the sample. This variation is easily evaluated by comparison of thermocouples 12 and 1 and was 85° K over most of the cycle for this orientation. The curves also show the 10-min lag between the response of the front and back plates. The internal heat generation caused a rapid change in temperature near the heaters as is shown by thermocouples 3 and 4. For both orientations the box enclosed heater was started at 77 min, stopped at 92 min, the bare heater started at 92 min and stopped at 107 min. This interchange of heater

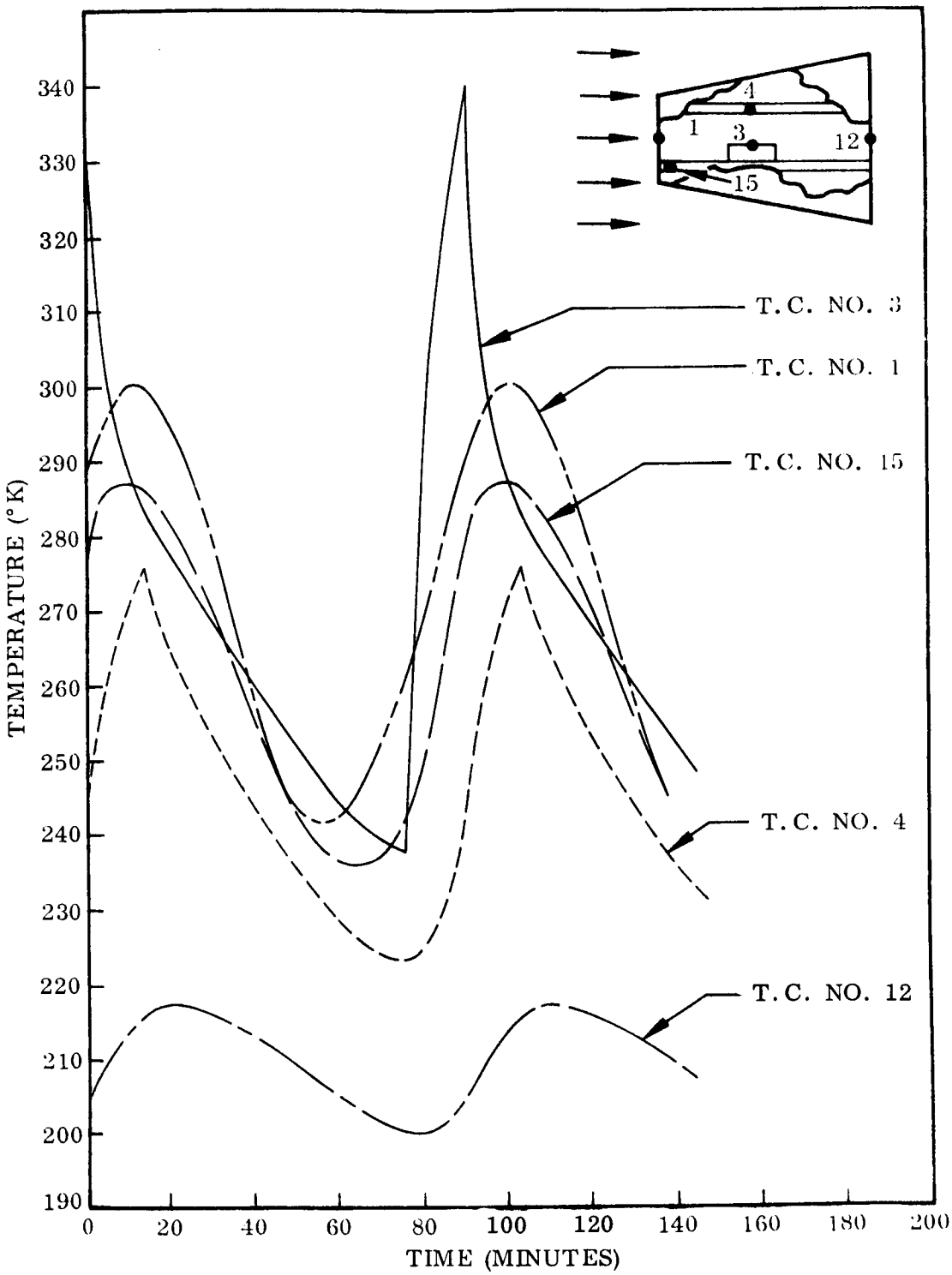

Fig. 21 Prototype Truncated Cone Transient Response, Small End Facing Lamps

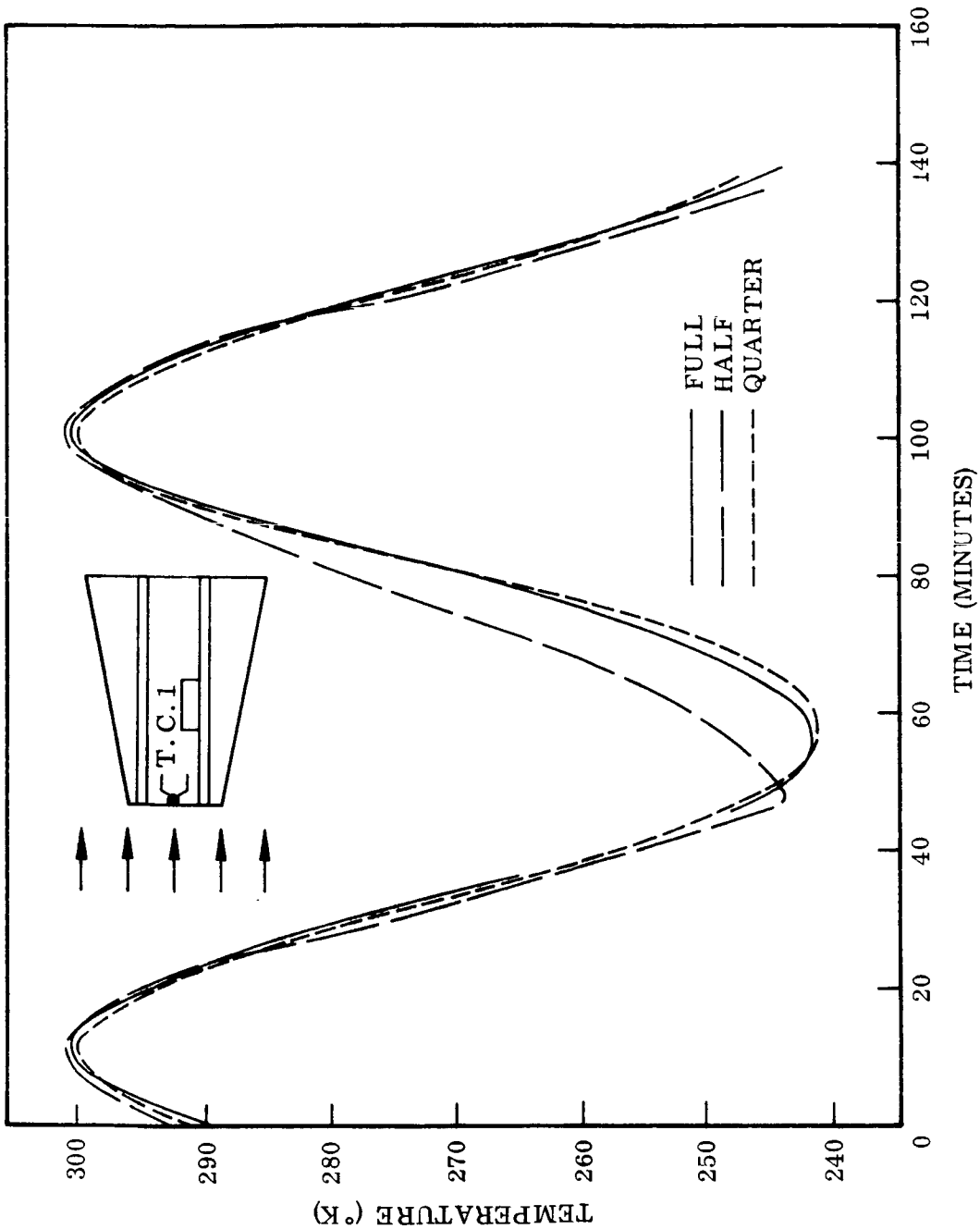

Fig. 22 Truncated Cone Transient Response at Center of Small End, Small End Facing Lamps

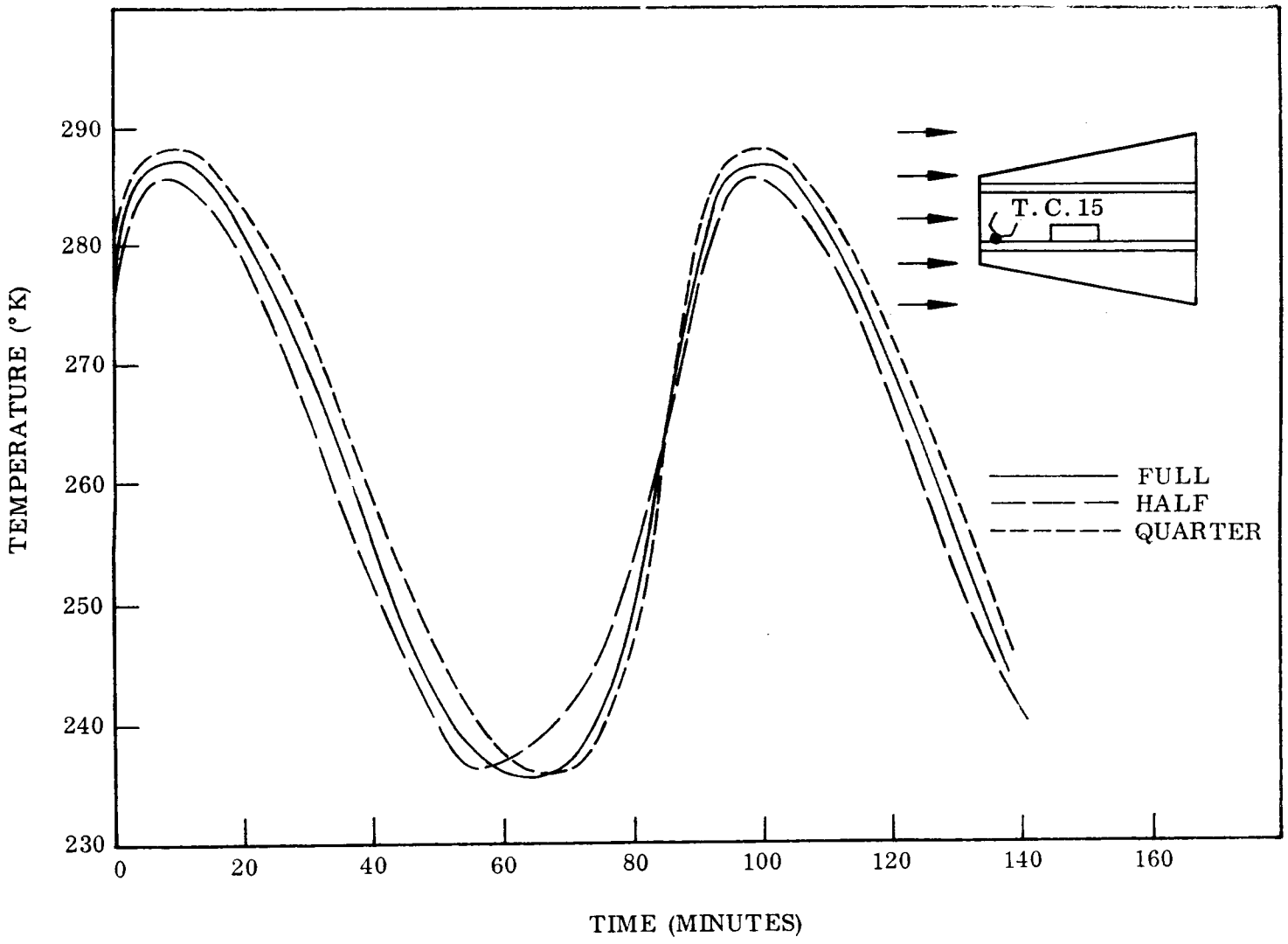

Fig. 23 Truncated Cone Transient Response at Small End Support Leg, Small End Facing Lamps

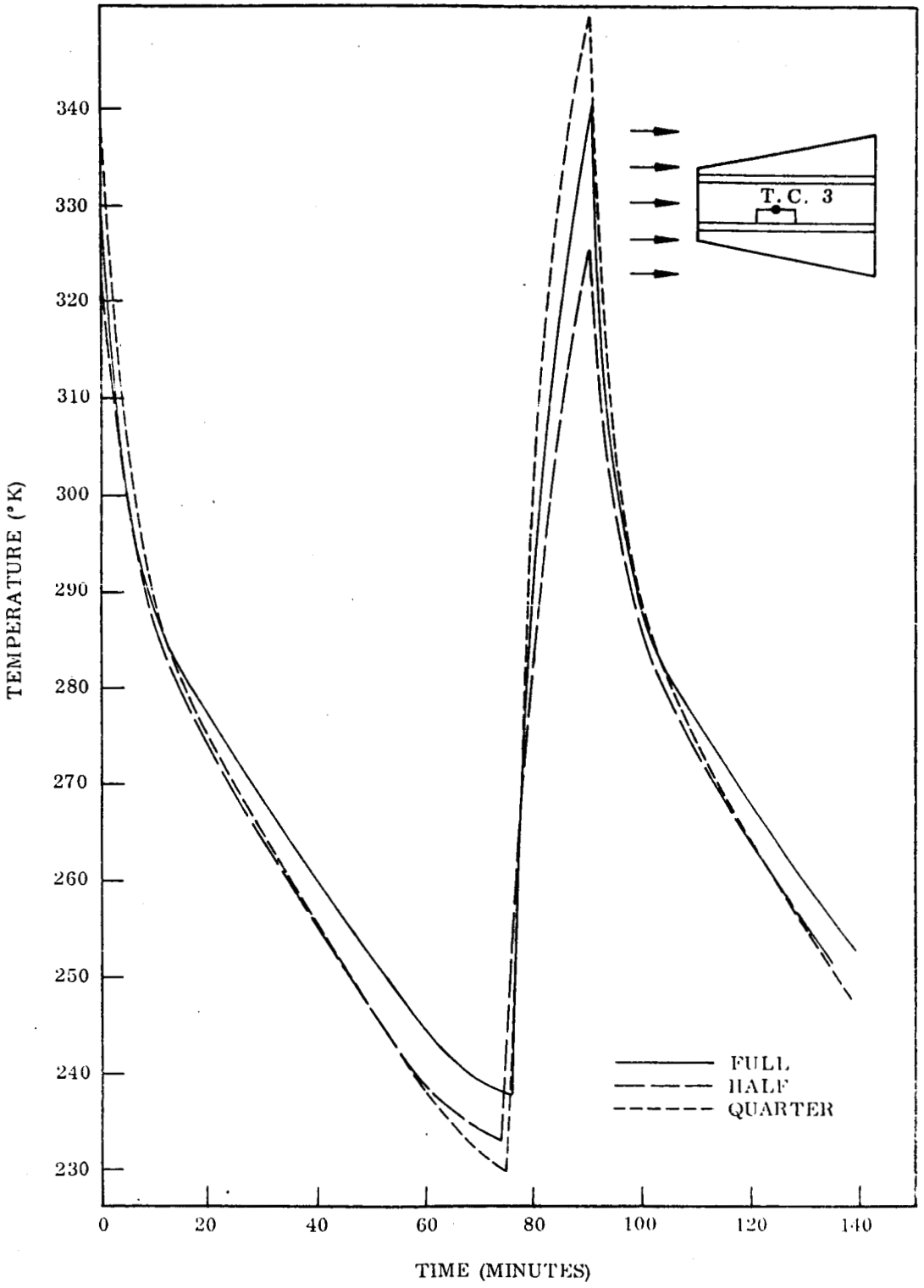

Fig. 24 Truncated Cone Transient Response at Heater Box, Small End Facing Lamps

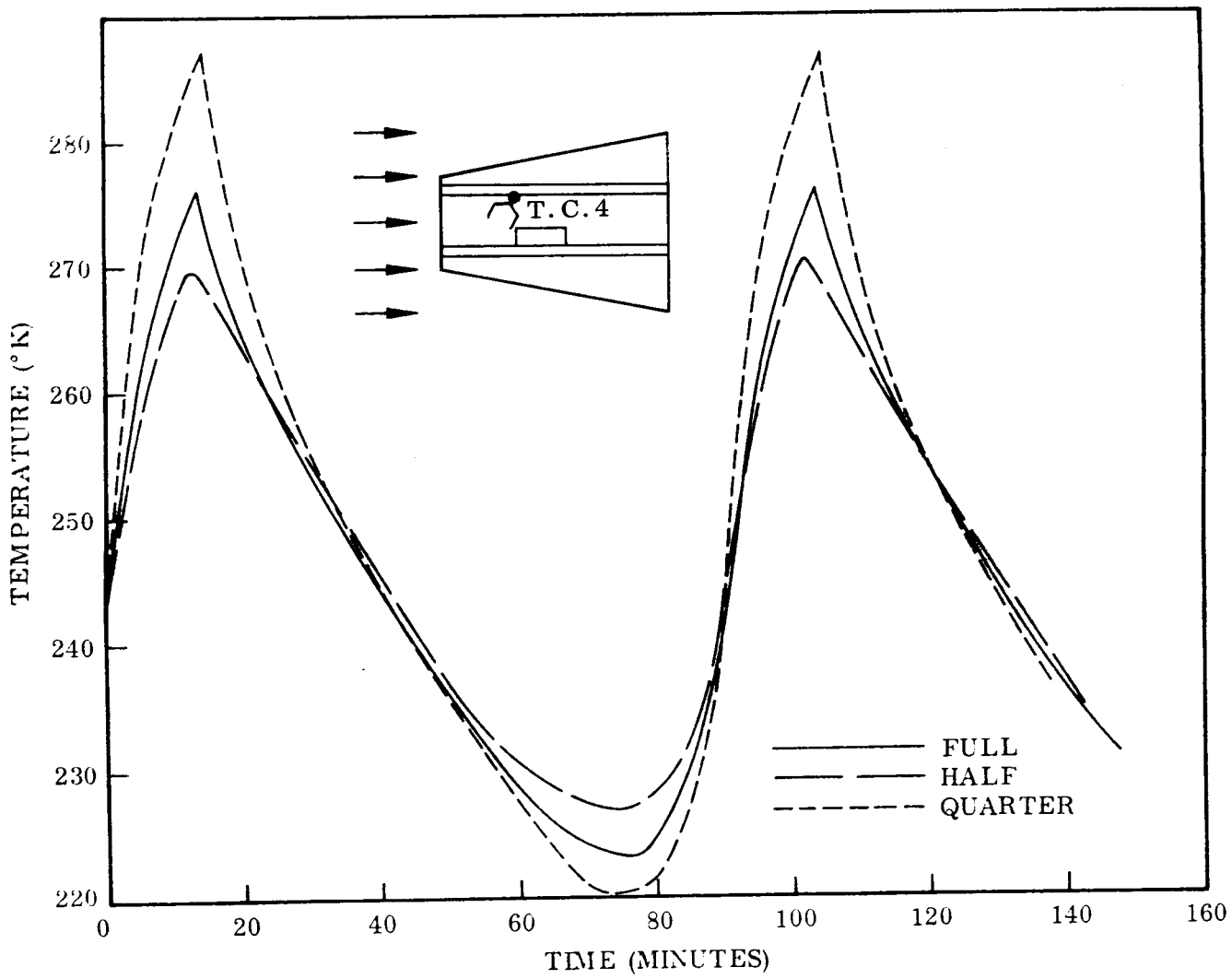

Fig. 25 Truncated Cone Transient Response Near Base Heater, Small End Facing Lamps

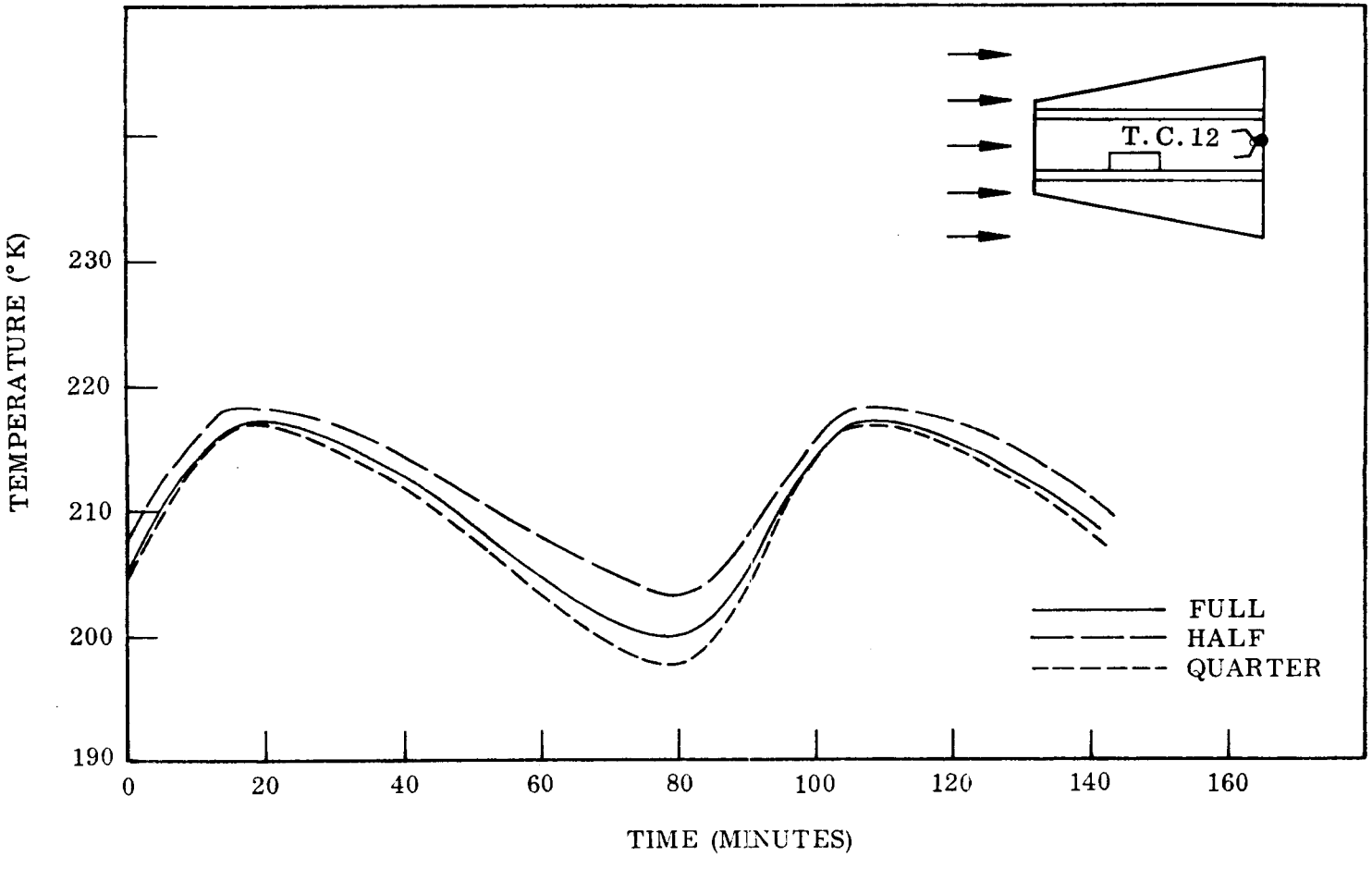

Fig. 26 Truncated Cone Transient Response at Center of Large End, Small End Facing Lamps

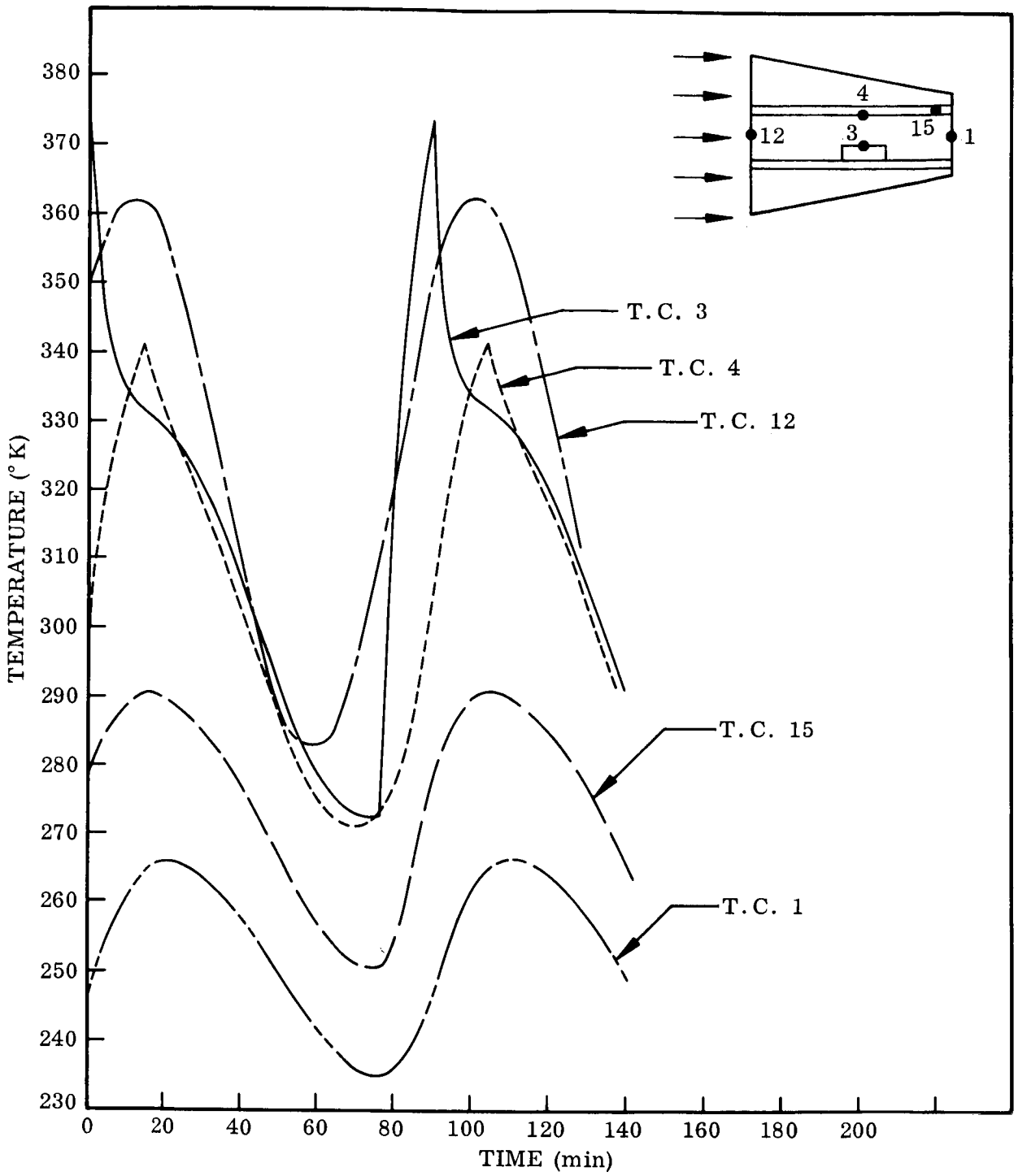

Fig. 27 Prototype Truncated Cone Transient Response, Large End Facing Lamps

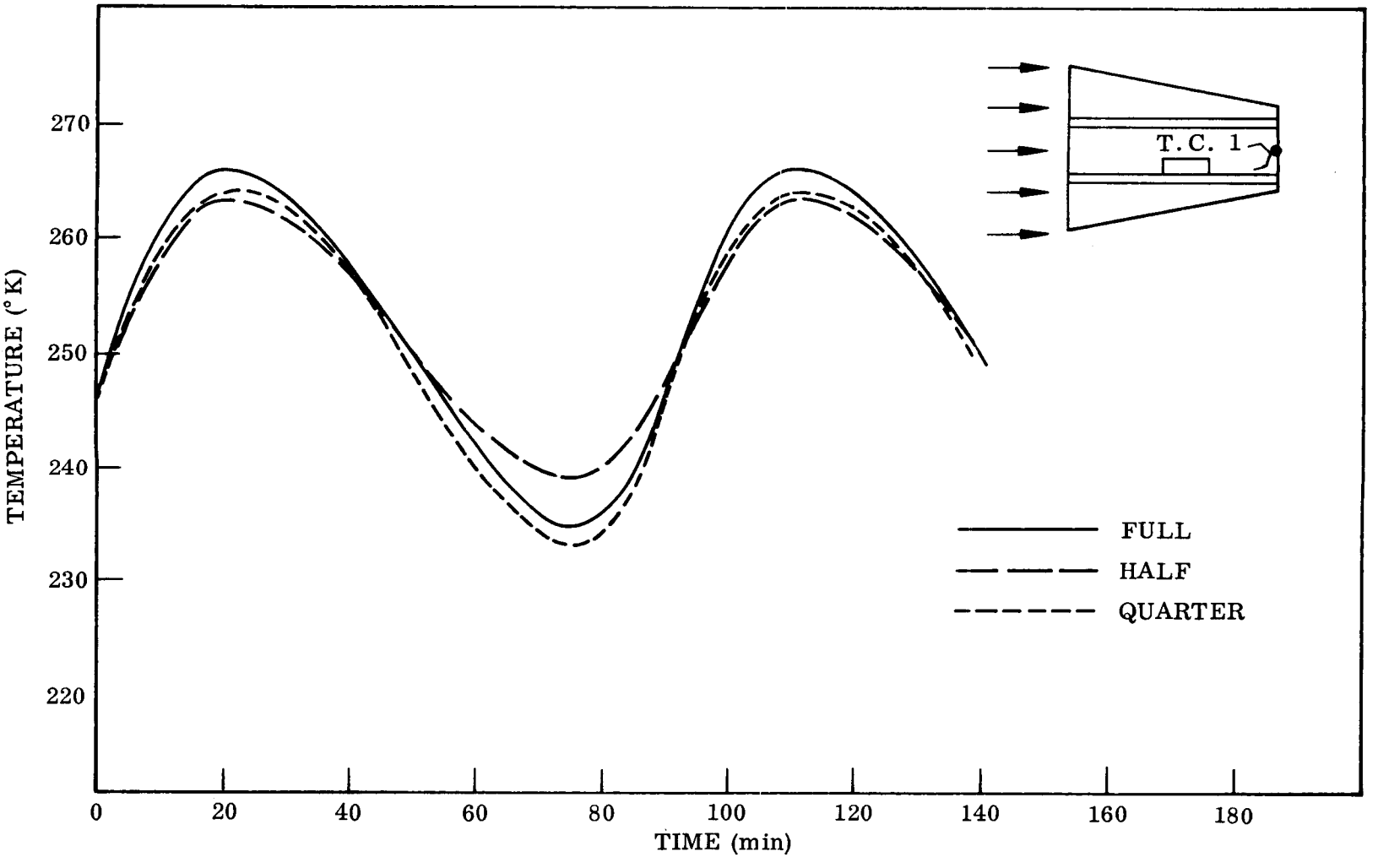

Fig. 28 Truncated Cone Transient Response at Center of Small End, Large End Facing Lamps

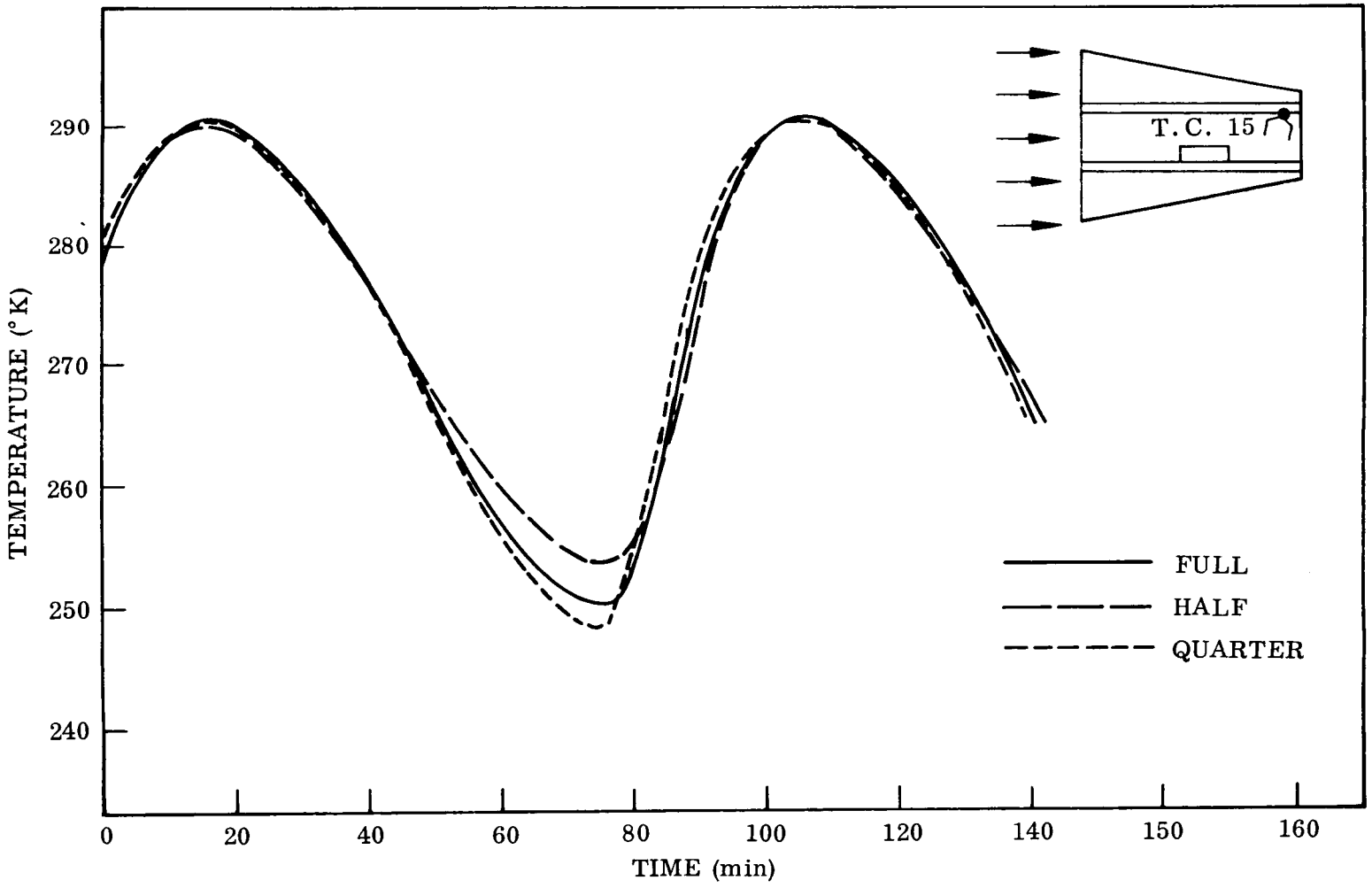

Fig. 29 Truncated Cone Transient Response at Small End Support Leg, Large End Facing Lamps

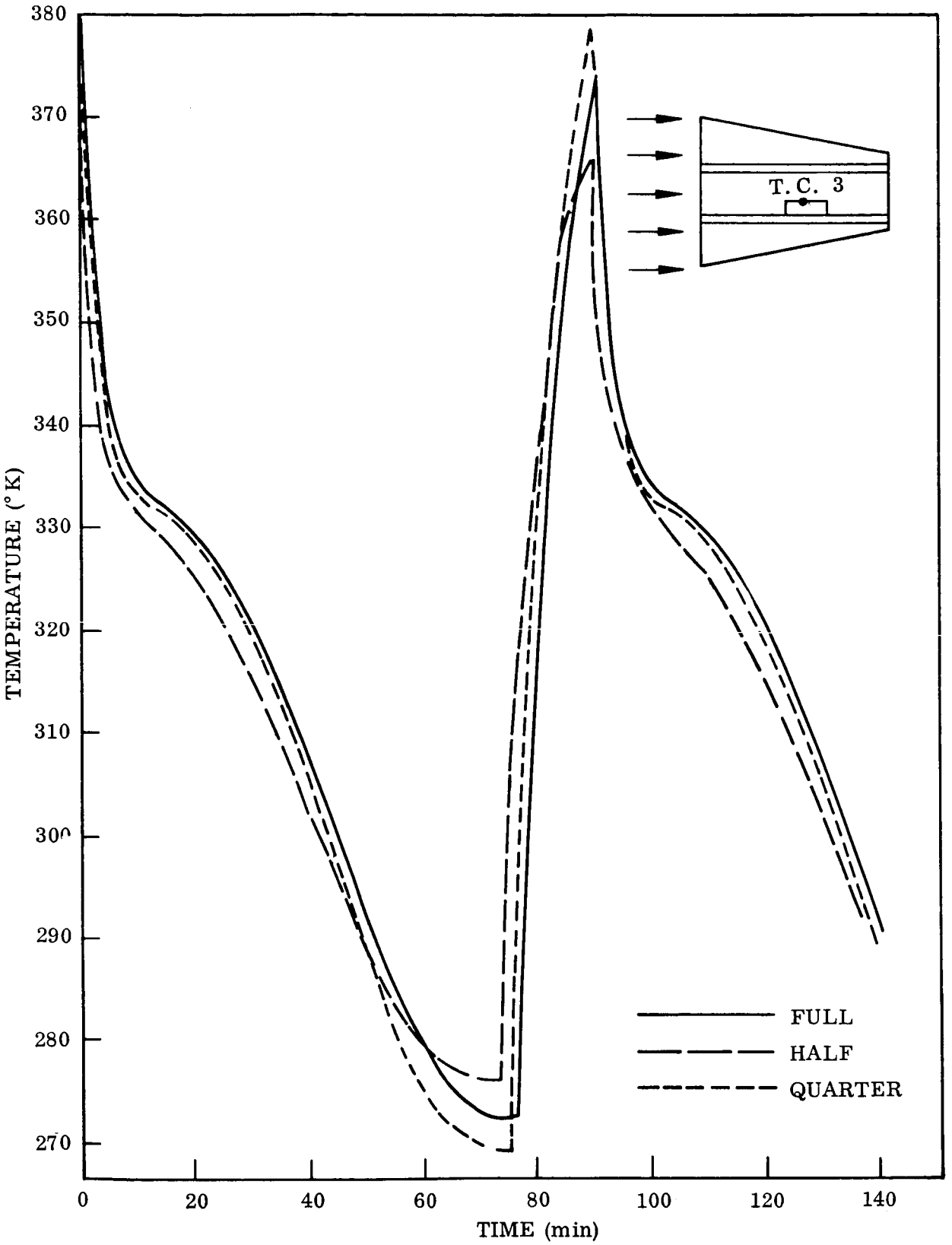

Fig. 30 Truncated Cone Transient Response Near Base Heater, Large End Facing Lamps

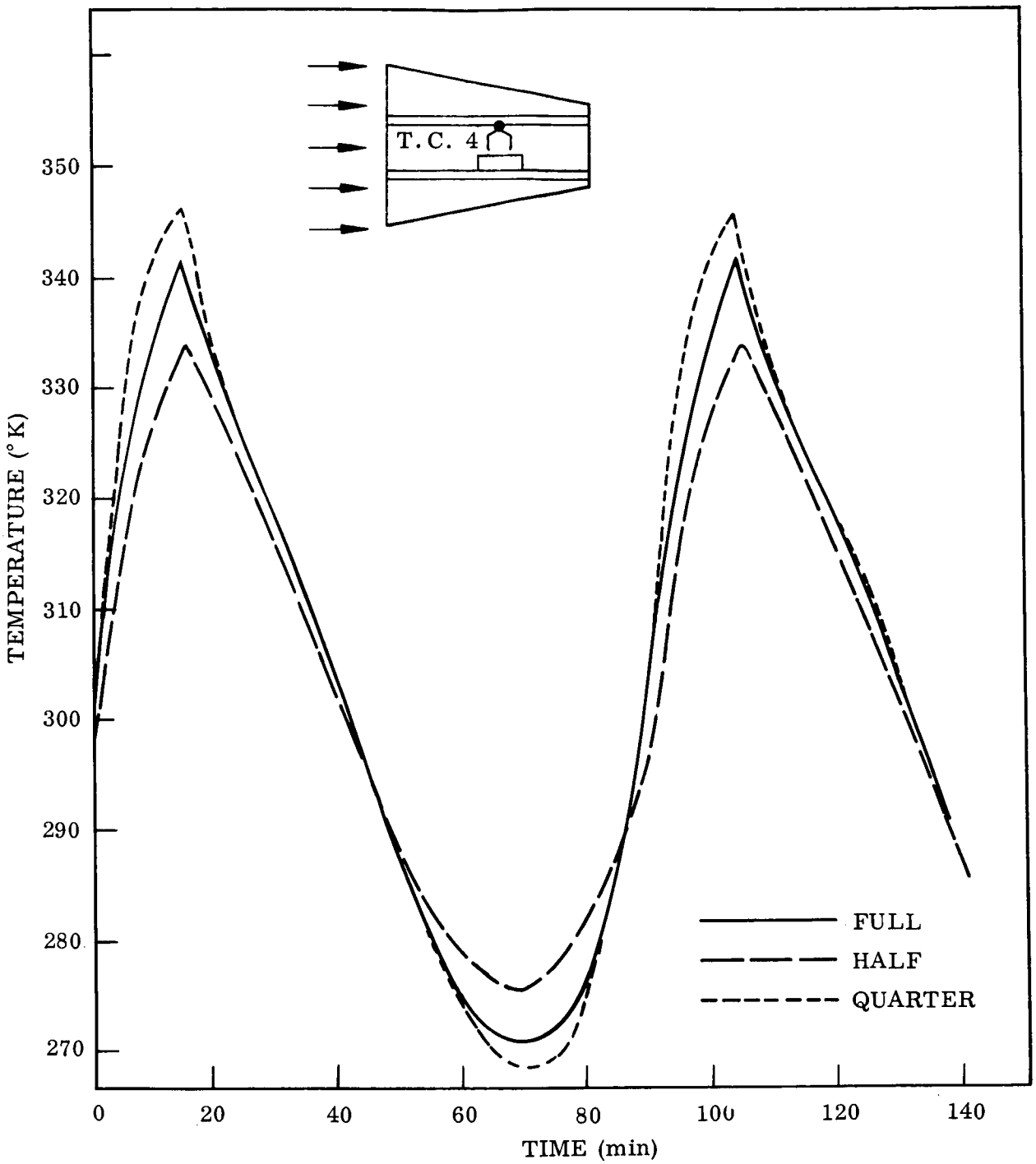

Fig. 31 Truncated Cone Transient Response Near Base Heater, Large End Facing Lamps

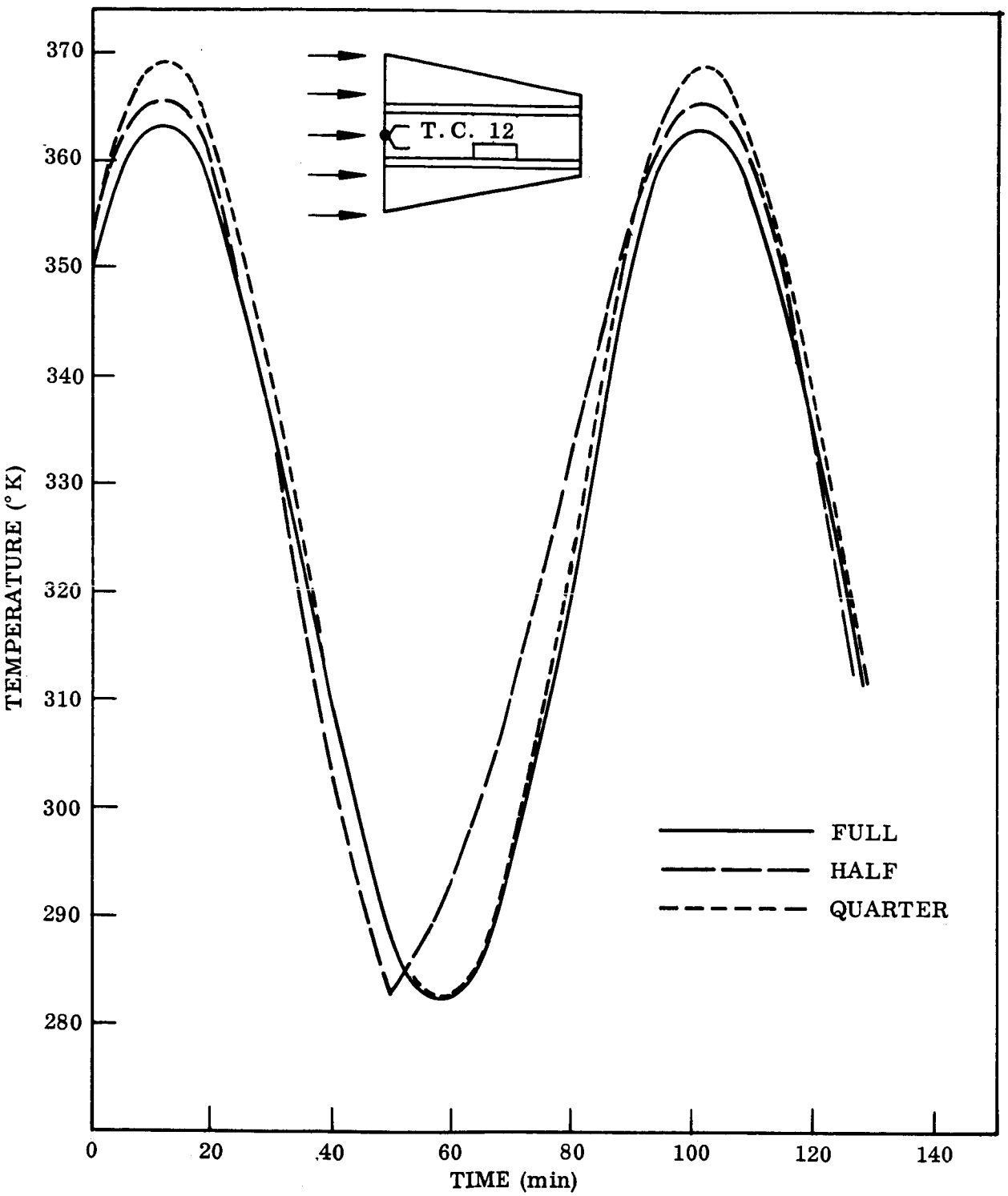

Fig. 32 Truncated Cone Transient Response at Center of Large End, Large End Facing Lamps

power in addition to conduction from the front plate caused a knee in the cooling curve at location number 3. As will be seen later, this knee was accurately predicted from the model results.

Figures 22 through 26 present the temperatures obtained for a given thermocouple location from each of the test models and the prototype. The model temperatures are presented in terms of prototype response and were obtained through reduction of the test data and extrapolation through the model laws. The accuracy of prediction for the prototype was excellent for all thermocouple locations. The comparison is most interesting for locations near the internal heaters. The shape of the response curves and the absolute value of predicted temperatures is excellent when compared directly to the measured prototype response. Figure 24 shows that the knee in the cooling curve at location 3 was faithfully reproduced by both of the small-scale models. The maximum and minimum of the cooling and heating curves near the heaters was predicted within approximately $\pm 10°$ K which was a definite improvement over the accuracy achieved during the first series of tests on configuration A. The extremes of the curves demonstrate the greatest deviation; however, with high heat rates over short durations such differences may be expected for identical prototypes.

Figure 22 presents the thermal response of the small end plate which for this case was facing the lamps. For the half-scale model, the front plate cooled at too fast a rate which resulted in a sharp rise on initiation of heating. This behavior was not observed during recording of the data since the period of the half-scale model was 18.3 min compared to 87 min for the prototype. The shorter cycle time produced sharp curves on the recording instrumentation so that direct comparisons to prototype curves could not be made during operation of the tests. It was found later that the reason for the rapid cool down was that the monitor detector on the lamp bank had too long a time constant to follow the required lamp program. Thus, the lamps shut down entirely near the end of the cooling curve. In spite of the inadequacy of the lamp simulation, temperature predictions were still within excellent limits of the prototype response. This is especially true for those areas removed from the immediate vicinity of the

front plate. These regions are represented by results shown on Figs. 23 through 26. For the more gentle temperature profiles of Figs. 23 and 26, the temperature prediction was within ± 5° K.

Figure 27 presents the transient results for the test series conducted with the large end plate facing the lamps. The larger absorbing area resulted in an increase of the average temperature of the object of approximately 60° K. It also produced response curves having considerably different shapes for each of the thermocouples reported. The knee in the response curve for T. C. No. 3 was amplified over that for the previous orientation. The temperature at T. C. No. 12 was obviously less strongly influenced by the heaters for this test series.

Figures 28 through 32 compare the thermal response obtained from the three sizes of test objects in terms of the prototype thermal levels and again show that excellent prediction accuracies were achieved for the test series. Control of the lamp bank during the half-scale tests was again inadequate as shown on Fig. 32; however, once again this did not seriously affect the response at locations removed from the irradiated end. The accuracy of prediction for the tests was on the same order as that obtained for the first test series with the exception of the heater locations where a slightly smaller difference is observed for peaks of the heating cycle. This decrease may be attributed to the higher overall thermal level of the test object. The results again demonstrate that these regions are the most difficult to reproduce since the energy rates are high and model design is critical. For thermocouple locations with less severe transients the absolute accuracy was considerably better and compared well with that achieved during the steady state tests. In particular, the curve shapes were predicted with excellent correspondence. This is best demonstrated by Figs. 29 and 30.

Section 4
DISCUSSION

The experimental program described in Section 3 dealt with two distinctly different geometries to demonstrate the applicability of thermal model studies to the prediction of spacecraft temperatures. The opposed disks were representative of a largely open structure while the truncated cones provided a totally closed thermal system. These two geometries were selected on the basis of geometrical simplicity with maximum thermal complexity.

Design and fabrication of the prototypes and models were performed using commonly available materials with thicknesses in the prototypes similar to those in use on current hardware. The distribution of energy in the test objects was equally dependent on radiation and conduction. These conditions were purposely included as part of the program scope so that the results obtained would be realistic in terms of the heat transfer in actual spacecraft.

Joint conductance difficulties were purposely eliminated from consideration by fabrication of the majority of joints using welded construction. In cases where bolted joints had to be used, they were assembled with a filler to reduce thermal resistance to a minimum. This form of construction eliminated a number of uncertainties and provided objects which were reliable indicators of the model technique.

The steady state and transient results obtained from the experimental program were generally of high accuracy though certain of the procedures used led to doubtful predictions. The measured peak transient thermal response of the heater box on the opposed disks was in error by 22° K for the half-scale model. This error was partially attributed to poor design of the heater filament geometry in the model. The accuracy was considerably improved by more careful design of the truncated cone heaters,

though the heater regions still provided the least accurate predictions of prototype behavior. A portion of the difficulty in modeling these high heat rate regions was that geometric distortion of heater box thicknesses was used. The thermal model was selected under the assumption that gradients through plate thicknesses were negligible while the model laws were satisfied for gradients in the plane of the plate and for the overall time constant. Utilizing distorted thicknesses in regions of high energy dissipation would be expected to locally distort the temperature distribution. While the heater regions produced the least accurate results, the absolute values predicted for the prototype truncated cone heater transient response were of acceptable accuracy in view of the complex phenomena occurring in these regions. It is doubtful that an analytical prediction would have produced a more satisfactory forecast for the transient behavior of the heaters.

The transient results for regions removed from the heater boxes were within the same limits of error as those obtained for steady state operation. In general, the predictions for the opposed disks were within 10° K of prototype response while for the truncated cone the predictions were within 5° K of prototype response. This accuracy is within the bounds of experimental error and demonstrates the quality of results available from carefully constructed models. The improved accuracy obtained during the second phase of the program was primarily attributed to the experience gained during the opposed disk tests in model construction, instrumentation, and chamber operation. Therefore, it may be concluded that the quality of results obtained from models will be strongly influenced by the experience and techniques of the experimentalist.

In general, the accuracy obtained from model studies is a function of the degree to which the model criteria are satisfied and of random or systematic experimental errors. When special materials are used for construction, it is possible to achieve a design with nearly complete satisfaction of the model criteria. However, when common materials are used which require a certain amount of geometric distortion, then a model design must be selected that best satisfies the model criteria while

imposing the least amount of thermal distortion. The models used in this program required introduction of geometric distortion and produced reliable temperature predictions. More extensive efforts during the design phases may have resulted in better models since the number of designs studied in this program was limited in each case. It is possible that utilization of a computer program analysis would have produced a more optimum model since considerably more combinations could have been considered. An optimum model design could then be selected from the numerous possibilities generated.

Errors are also introduced by thermally induced material property variations. Changes in properties must be considered during the design phase, and where this influence is appreciable, a solution sought which minimizes their influence. To properly assess the degree to which these errors will affect the results requires a detailed thermal analysis of the system. This is best accomplished using a computer solution to forecast the thermal behavior of the prototype. The model behavior may then be assessed using the same procedure. This was not done in this program. However, the thermal property changes for models used in this program were small since the total temperature range used was limited. For model studies with large temperature variations it is possible for this error to achieve sizable proportions. Procedures must then be implemented to select a scale ratio, temperature ratio, or model material that result in minimizing the influence of thermal property changes.

Errors introduced by manufacturing tolerances in material thicknesses are essentially beyond control of the model designer. Tolerances in thicknesses are normally in the range of 1 or 2 mils and have little effect on prototype thermal conditions. However, on small-scale models where skin thicknesses on the order of 0.025 cm (0.010 in.) or less are used, these tolerances may result in considerable error in the model conducting path. To minimize this source of error, the materials used for this program were selectively obtained from available stock to assure that their average thicknesses were those required by the model design. In this selective process it was found that standard stock designated as 0.101-cm thick (0.040 in.) was more frequently

in the range 0.104 ± 0.025 cm (0.042 ± 0.001 in.). The actual average thickness can thus result in a 4 percent increase in path conductance over that assumed when using the manufacturer's nominal thicknesses. This same order of variation was found in other sizes of stock.

The random and systematic experimental errors that increase the uncertainty of model results are the same as those experienced in prototype measurements. The installation and readout of thermocouples, control of sample irradiation, establishment of chamber conditions, and data recording must all be accomplished with extreme care to reduce experimental errors to minimal values. This program demonstrated that thorough checks on the steady state and transient response of thermocouples, before and after installation on the test object, is of considerable value. While these checks were performed on the opposed disk models, erroneous thermocouple responses were still experienced. In view of this finding, more complete checkout procedures were used on the truncated cones. In addition, human error was reduced by incorporation of digital readout equipment during the cone tests. This permitted two readings in rapid succession and provided an immediate indication of an incorrect observation. No large, unexplainable prediction errors were experienced during the cone tests. These procedures are mentioned here to indicate that model experiments must utilize the most up-to-date experimental techniques if errors are to be reduced to minimal levels. The error associated with the experiment is most important when the model temperatures are considerably lower than prototype temperatures. This requires scaling up of the observed values with the result that small errors may become excessive in terms of utility of the end result.

Section 5
CONCLUSIONS AND RECOMMENDATIONS

The experience gained during this program in model design, model construction, and thermal testing leads to the following conclusions and recommendations:

- Thermal models are well suited for studies of thermal behavior in the space environment. Prediction accuracies on the order of 1 percent in absolute temperature can be achieved using steady-state and transient modeling procedures in a simulated space environment.
- The design, construction, and thermal simulation procedures used for model studies must be in accordance with the similarity criteria stated in Section 2. Exact satisfaction of the criteria, both geometrically and thermally, will produce exact similarity between model and prototype temperature and heat rates.
- The use of available construction materials throughout the model will normally require geometric distortion of heat-flow paths. Model scale ratios must be selected concurrently with materials so that the required distortion is a minimum.
- Geometric distortion will cause perturbations on local temperature profiles. However, for areas removed from the local disturbance, the model will preserve similarity.
- Geometric distortion in regions of high heat flux will result in serious prediction errors. Care must be exercised in these regions to assure three-dimensional compliance with the model criteria.
- Steady state models are more easily constructed from available materials than are models for observation of both steady state and transient phenomena. The additional constraints imposed by the transient criteria introduce

considerable material selection difficulties and restrict the selection of model scale ratios. In general, the transient model will produce less accurate predictions than the model designed for only steady state operation.

- This program has established the feasibility and accuracy of thermal modeling on simple geometries having complex thermal behavior. The models provided reliable forecasts of both steady state and transient phenomena for scale ratios of approximately 1/2 and 1/4. The overall absolute temperature prediction accuracy was approximately 3 percent for the disks and 1 percent for the cones. These results provide substantial evidence that model studies can furnish reliable forecasts of full-scale thermal performance in the space environment.
- The techniques required for performance of this program were straightforward since simple geometric arrangements were used. Having shown that the model approach is a useful tool, it is recommended that the techniques be further developed by continued work on actual or contemplated spacecraft hardware.

Section 6

REFERENCES

1. S. Katzoff, Similitude in Thermal Models of Spacecraft, NASA TND-1631, Apr 1963

2. J.B. Wainwright, L.R. Kelley, and T.H. Keesee, "Modeling Criteria and Testing Techniques for the Simulation of Space Environments," Fourth Annual Symposium on Space Environment Simulation, Los Angeles, Calif., May 1963, pp. 1–4

3. B.T. Chao and G.L. Wedekind, "Similarity Criteria for Thermal Modeling of Spacecraft," J.S.R., Vol. 2, No. 2, Apr 1965

4. B.P. Jones, "Thermal Similitude Studies," J.S.R., Vol. 1, No. 4, Aug 1964, pp. 364–369

5. L.G. Clark and K.A. Laband, "Orbital Station Temperature Control," Astronautics, Vol. 7, No. 9, 1962, pp. 40–43

6. A.A. Fowle, F. Gabron, and J.M.F. Vickers, "Thermal Scale Modeling of Spacecraft, an Experimental Investigation," AIAA Space Simulation and Testing Conference, Nov 1964

7. J.M.F. Vickers, Space Programs Summary 37–30, Vol. 4, Dec 1964, pp. 75–77, and Vol. 4, Feb 1965, pp. 111–112

8. D.L. Adkins, "Scaling of Transient Temperature Distributions of Simple Bodies in a Space Chamber," AIAA Thermophysics Specialists Conference, Monterey, Calif., Sep 13–15, 1965; AIAA paper no. 65-660

9. B.P. Jones and J.K. Harrison, "A Set of Experiments in Thermal Similitude," NASA Technical Memorandum NASA TMX-53346, Oct 1965

10. J. M. F. Vickers, "Thermal Scale Modeling," Astronautics and Aeronautics, Vol. 5, May 1965, pp. 34–39

11. B. P. Jones and J. R. Watkins, Thermal Similitude Studies, Part I, Internal Note, NASA Marshall Space Flight Center, Sep 1963

12. -----, Thermal Similitude Studies, Part III, Internal Note, R-RP-INT-64-6, NASA Marshall Space Flight Center

13. J. R. Watkins, Thermal Similitude Studies, Part II, Internal Note, R-RP-INT-64-4, NASA Marshall Space Flight Center

14. -----, Sets of Similarity Ratios for Thermal Modeling, NASA TN D-3452, May 1966

Appendix A

EFFECT OF SOURCE SPECTRAL DISTRIBUTION ON THERMAL MODELING

The thermal behavior of spacecraft is largely dependent upon an interchange of radiant energy between the spacecraft and its environment. This energy exchange is carefully considered during the hardware design phases and is controlled through use of selective thermal control surfaces. The spectral absorbtance and emittance properties of the surfaces may be independent of wavelength (flat reflectors and absorbers) or may be strong functions of wavelength (solar reflectors and absorbers).

The surfaces whose radiant properties are strongly wavelength-dependent will demonstrate significant changes in total absorptance as a function of the spectral distribution of irradiation. This variation in absorptance presents considerable difficulties in hardware thermal testing since the exact distribution of absorbed energy for an entire vehicle is attained only when the solar spectrum is precisely matched. For many totally enclosed vehicle configurations, the degree of source to sun spectral mismatch is a minor difficulty since these vehicles can often be tested by duplication of the total absorbed energy. An example of this approach is found in the techniques in current use for acceptance testing of Agena vehicles where tungsten filament lamps supply the required energy. However, for more complex satellites, where a variety of thermal control surfaces are employed on exposed brackets, instrument packages, support members, etc., the utilization of exact source simulation is mandatory. For geometries of this type the source must simulate not only the spectral distribution but also the collimation of solar energy. Simulation of collimated energy provides shadowing and interreflections of the same degree as those experienced during actual flight.

To date, no solar simulator provides an exact duplication of the energy arriving from the solar disk at a distance of 1 AU. The thermal error caused by the solar mismatch of any given source must be evaluated in terms of each particular test object. This same source of error will be present when thermal models are used in place of the full-scale hardware.

A portion of the program reported herein was devoted to an evaluation of the effects of source spectral mismatch when interreflections are present. This evaluation was conducted to determine the advisability of performing additional experiments on the opposed disk models whose purpose would be to demonstrate the effect of source mismatch on model predictions.

A simplified version of the opposed disk models was selected for this study. The assumed configuration consisted of two isolated opposed disks having dimensions identical to those used in this program, but with no interconnecting members and without a heater box. It was assumed that these disks were irradiated by sources having dissimilar spectral distributions both with and without multiple reflections between the disks. The isolated disks were selected for study to simplify the required computations, to demonstrate the largest possible thermal error due to source mismatch, and to provide results which could be checked experimentally in the event that such a verification is desired.

The computations were performed for two general conditions. The first condition assumed that energy from an external source was incident only upon the front surface of the large disk. The second condition considered energy incident on both the front and rear surfaces of the large front disk. This introduces interreflections between the opposed disk surfaces and provides a measure of the effect of source spectrum on the thermal equilibrium of the two disks. The geometry and surface coatings used for the computations are shown in Fig. A-1. The properties of the assumed coatings are given in Table A-1. The manner in which the values were obtained is given in Appendix B.

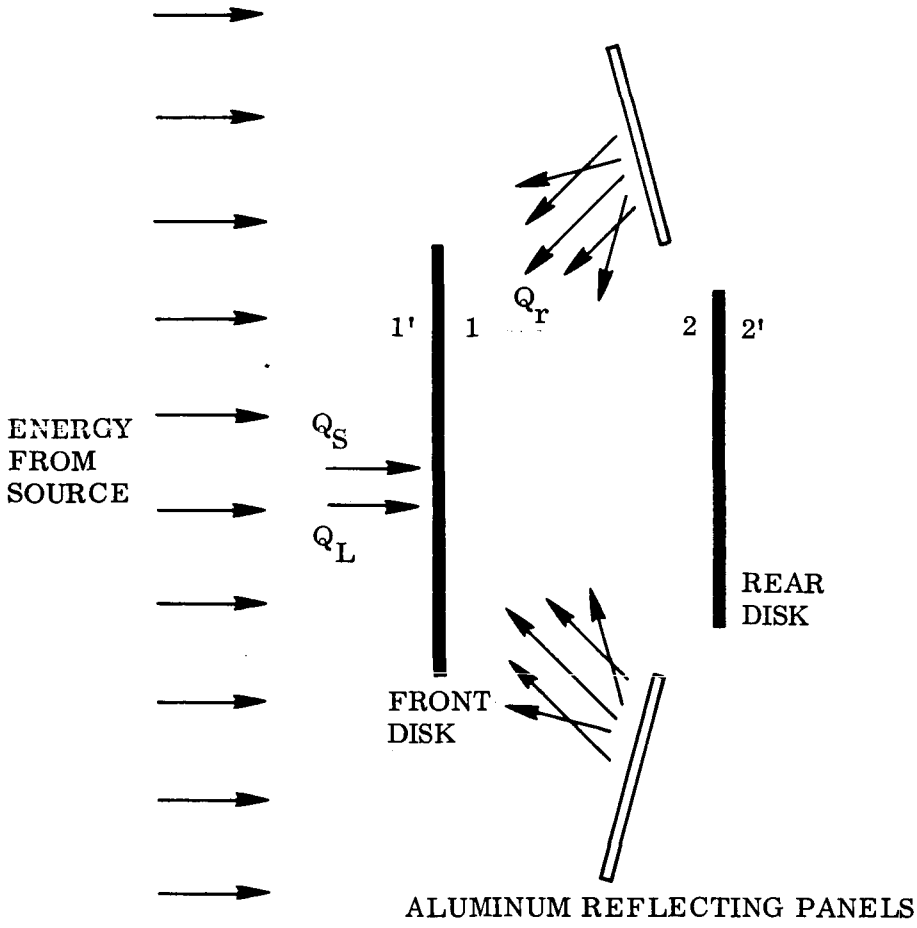

Front Disk dia.	30.7 cm (12.15 in.)
Rear Disk dia.	26.0 cm (10.3 in.)
Disk Spacing	14.2 cm (5.61 in.)

Coatings

Side 1	Fuller white silicone
Side 1'	Fuller white silicone
Side 2	White silicone on Mystic tape (Thermatrol)
Side 2'	aluminum

Fig. A-1 Opposed Disk Geometry for Study of Interreflections

Table A-1

RADIANT PROPERTIES OF SURFACE COATINGS

Coating Type	Side	Solar Absorptance	Infrared Lamp Absorptance		Infrared Emittance
			90 V	40 V	
White silicone	1,1'	0.22	0.27	0.36	0.90
Aluminum	2'	0.14	0.04	0.03	0.03
Thermatrol	2	0.20	0.20	0.26	0.95

The geometry chosen for study provides a system with considerable sensitivity to the spectral distribution of incident energy. The aluminum reflector panels would place energy on the interior of the cones with essentially the same spectral distribution as the source. This distribution would be considerably altered after reflection from surface 1. Each interreflection then results in an additional alteration of the spectrum.

CONDITION 1 NO INTERREFLECTIONS $Q_r = 0$

This condition is similar to that used for the experimental program described in Section 3. Energy is incident on the front plate which in turn shadows the remaining surfaces. For this arrangement, it is necessary to provide sufficient energy to the front plate from any external source to assure that identical energy rates are absorbed. The amount absorbed by solar energy is given by $\alpha_s A Q_s$; therefore, the simulated flight test must assure that

$$\alpha_s A Q_s = \alpha_L A Q_L \tag{A.1}$$

where

A = surface area

α = total absorptance

Q = energy rate per unit area

S = solar energy

L = lamp energy

The values of total absorptance are defined on the basis of the integrated spectral absorptance for each surface and source. For the solar spectrum this is

$$\alpha_s = \frac{\int_0^\infty \alpha_\lambda \, q_{s\lambda} \, d_\lambda}{\int_0^\infty q_{s\lambda} \, d_\lambda} \qquad \text{(A.2)}$$

where

α_λ = surface spectral absorptance

$q_{s\lambda}$ = relative solar spectral intensity

λ = wavelength

A similar definition is used for the absorptance of any other combination of source and surface.

The requirements of Eq. (A.1) may be met by determination of α_L for a given source spectrum followed by adjustment of Q_L. Given that Eq. (A.1) is satisfied, then the simulated test will provide identical results to those expected during solar exposure. Thus, for geometries with completely shadowed internal areas, it is satisfactory to provide the proper amount of absorbed energy at each surface point then errors due to source spectral mismatch can be controlled. The techniques employed during tests of the truncated cones used this approach by proper control of lamp intensity and lamp bank configuration.

CONDITION 2 INTERREFLECTIONS $Q_r \neq 0$

This case considers the error introduced by spectral mismatch when interreflections occur between spectrally selective surfaces. For this case the spectral content is altered by each reflective surface with the result that the total energy absorbed by a

given area is a strong function of the original source energy spectrum. Therefore, when a model or full scale test is conducted using a simulated solar source the results obtained will be influenced by the simulator spectrum.

The geometry selected for study of this effect is that of Fig. A-1 with $Q_r \neq 0$. It is assumed that energy from the source, Q_s, directly radiates the front plate surface and the reflector panels. The panels then reflect energy Q_r to the inner surface of the front plate. A portion of Q_r is absorbed, reflected to surface 2, and re-reflected to surface 1 where another absorption occurs. Summing all absorptions at surface 1 due to the multiple reflections, and assuming all reflections are diffuse, gives

$$Q_1 = A_1 W \int_0^\infty \frac{\alpha_{1\lambda}\, q_\lambda\, d\lambda}{1 - F_{12} F_{21} \rho_{1\lambda} \rho_{2\lambda}} \tag{A.3}$$

For surface 2 the total energy absorbed is

$$Q_2 = A_1 W F_{12} \int_0^\infty \frac{\alpha_{2\lambda} \rho_{1\lambda} q_\lambda\, d\lambda}{1 - F_{12} F_{21} \rho_{1\lambda} \rho_{2\lambda}} \tag{A.4}$$

In these relations

A = surface area

W = radiant power per unit area for source Q, i.e., $Q = \int_0^\infty W q_\lambda\, d\lambda$

q_λ = relative spectral distribution of Q

F_{12} = geometric shape factor from surface 1 to surface 2

α_λ = spectral absorptance of surface

ρ_λ = spectral reflectance of surface

λ = wavelength

Equations (A.3) and (A.4) are based on the further condition that the reflector panels are surfaced and arranged in a manner that precludes their participation in the actual multiple reflections.

For the purposes of illustration it is now desired to perform an energy balance on the disks for three separate source conditions

1. Q_s and Q_r are solar energy
2. Q_s and Q_r are supplied by tungsten filament lamps at 90 volts
3. Q_s and Q_r are supplied by tungsten filament lamps at 40 volts

To perform the computation requires knowledge of the source spectral content and the spectral absorptance of the surfaces. The spectral emissive power of the tungsten lamps was determined as part of this program and is fully reported in Appendix B. The solar spectral content was taken from Johnson's data.* The reflective properties of the surfaces were determined using a heated cavity hohlraum from 2.0 to 5.0 microns and an integrating sphere reflectometer from 0.27 to 2.7 microns. These properties were then integrated against the source spectrum to establish the total values given in Table A-1. The shape factors between the disks were obtained from the tables of Hamilton and Morgan. †

Using the spectral data and shape factors, and performing the integrations indicated by Eqs. (A.3) and (A.4) for conditions 1, 2, and 3, provides the results tabulated in Table A-2. The results given represent the total energy absorbed by each surface due to the external sources.

---

*Johnson, F.S., "The Solar Constant," J. of Meteorology, Vol. II, pp. 431–439, 1959

†Hamilton, D.C., and Morgan, W.R., "Radiant Interchange Configuration Factors," NACA TN 2836, Dec 1952.

Table A-2

TOTAL ENERGY ABSORBED BY SURFACES 1 AND 2

Condition	Q_1	Q_2
Solar energy	$0.252\ A_1\ W$	$0.135\ A_1\ W\ F_{12}$
Tungsten lamps at 90 volts	$0.306\ A_1\ W$	$0.103\ A_1\ W\ F_{12}$
Tungsten lamps at 40 volts	$0.424\ A_1\ W$	$0.124\ A_1\ W\ F_{12}$

It is also necessary to consider the energy emitted, absorbed, and interreflected by each surface in the infrared in order to perform a complete energy balance on the system. For this purpose it is assumed that the surfaces are "grey" and have the values given in Table A-1. It is also assumed that all reflections, emissions, and absorptions take place with a cosine distribution. Under these assumptions, if surface 1 is at temperature T_1 and is emitting at $\sigma \epsilon_1 A_1 T_1^4$ then the total amount of this energy reflected back to 1 by 2 and absorbed by 1 is given by

$$\frac{F_{12} F_{21} \rho_2 A_2 \epsilon_1^2}{1 - F_{12} F_{21} \rho_1 \rho_2} \sigma T_1^4 \qquad \text{(A. 5)}$$

Likewise, the amount emitted by 1 and finally absorbed by 2 is given by

$$\frac{F_{12} A_1 \epsilon_1 \epsilon_2}{1 - F_{12} F_{21} \rho_1 \rho_2} \sigma T_1^4 \qquad \text{(A. 6)}$$

In these equations

σ = Stefan-Boltzmann constant

ϵ = infrared emittance

ρ = infrared reflectance

Similar relations hold for distribution of the energy originally emitted by surface 2. Of this, the amount absorbed by surface 1 is given by

$$\frac{F_{21} A_2 \epsilon_1 \epsilon_2}{1 - F_{12} F_{21} \rho_1 \rho_2} \sigma T_2^4 \tag{A.7}$$

and, the amount absorbed by surface 2 is

$$\frac{F_{12} F_{21} \rho_1 A_2 \epsilon_2^2}{1 - F_{12} F_{21} \rho_1 \rho_2} \sigma T_2^4 \tag{A.8}$$

Through use of Eqs. (A.3) through (A.8) it is now possible to formulate a complete energy balance on the arrangement shown in Fig. A-1. However, one more logical condition should be imposed. That is that under all conditions it is required that the complete system absorb equal amounts of energy from the source. This requirement is synonymous with the procedures used for testing of totally enclosed systems. To meet this condition it is necessary to adjust source levels so that

$$\alpha_{1'} Q_s = \text{constant} \tag{A.9}$$

$$Q_1 + Q_2 = \text{constant} \tag{A.10}$$

A base condition was established by consideration of the one-half scale model size with the possible addition of reflector panels. The available source for irradiation of this model is a carbon arc solar simulator having a beam diameter of 91.5 cm (36 in.). For this arrangement the energy levels would be

$$Q_s = 0.14 \text{ watts/cm}^2 \text{ of surface } 1'$$

$$Q_r = 0.024 \text{ watts/cm}^2 \text{ of surface } 1$$

Equations (9) and (10) are satisfied for

Condition 2 – infrared lamp voltage 90 V

$$Q_L = 0.114 \text{ watts/cm}^2$$

$$Q_r = 0.021 \text{ watts/cm}^2$$

Condition 3 – infrared lamp voltages 40 V

$$Q_L = 0.084 \text{ watts/cm}^2$$

$$Q_r = 0.015 \text{ watts/cm}^2$$

Using these energy levels for irradiation of the assumed opposed disks, it is possible to establish their temperatures by solution of the energy balance. For the front disk this is given by

$$\alpha_{1'} A_1 Q_s + Q_1 + \frac{F_{12}F_{21}A_1\rho_2\epsilon_1^2}{1 - F_{12}F_{21}\rho_1\rho_2}\sigma T_1^4 + \frac{F_{12}A_1\epsilon_1\epsilon_2}{1 - F_{12}F_{21}\rho_1\rho_2}\sigma T_2^4 = A_1(\epsilon_1 + \epsilon_{1'})\sigma T_1^4 \quad (A.11)$$

and for the rear disk by

$$Q_2 + \frac{F_{12}F_{21}\rho_1 A_2\epsilon_2^2}{1 - F_{12}F_{21}\rho_1\rho_2}\sigma T_2^4 + \frac{F_{21}A_2\epsilon_1\epsilon_2}{1 - F_{12}F_{21}\rho_1\rho_2}\sigma T_1^4 = A_2(\epsilon_2 + \epsilon_{2'})\sigma T_2^4 \quad (A.12)$$

Simultaneous solution of Eqs. (A.11) and (A.12) provides the values given in Table A-3.

Table A-3
DISK EQUILIBRIUM TEMPERATURES

	Disk Temperature (°K)	
	Front	Rear
Solar spectrum	252	210
Infrared lamps at 90 V	250	205
Infrared lamps at 40 V	250	204

These results indicate that the use of a tungsten source to simulate solar energy does not cause a large change in absolute temperature of the two disks. The front disk temperature drops from 252°K to 250°K while the rear plate temperature drops from 210° K to 205° K for simulation using a tungsten source. The temperature difference between the front and rear plates is increased from 42° K to 45° K. These are minor changes in the thermal condition considering the rather significant difference in the solar and tungsten spectrum.

The results apply only to the special conditions assumed in the computations and cannot be considered as a general evaluation of errors due to a spectral mismatch. However, the surface coatings and geometry were chosen to amplify the effect of source spectral mismatch while using an available model configuration. The inclusion of connecting legs between the disks and an internal heater would further reduce the resulting temperature differences and cause an experimental confirmation of the results to be insensitive to the change in spectrum.

If the configuration shown in Fig. A-1 were tested under a one sun solar simulated test then its temperature distribution would be that stated in Table A-2. The size tested would be that of the half-scale model of Section 3 since the available solar simulator has a maximum beam diameter of only 91.5 cm. The quarter-scale model could then be used with both solar and tungsten energy to predict the half-scale (prototype) thermal response. The computed results of the postulated experiment are given in Table A-4.

Table A-4

COMPUTED TEST RESULTS FOR OPPOSED DISK MODEL

Test Objective	Disk Temperature (° K)			
	Front		Rear	
	Quarter Scale Measured	Predicted for Half-Scale	Quarter Scale Measured	Predicted for Half-Scale
Half-scale (prototype) solar energy	252		210	
Quarter-scale (model) solar energy	223	252	186	210
Quarter-scale (model) tungsten 90 V	221	250	181	205
Quarter-scale (model) tungsten 40 V	221	250	180	204

The computed results show that the quarter-scale model would exhibit only slight thermal variations as the incident spectrum is changed. In fact, errors due to model construction, lamp intensity control, and thermometry could easily exceed the expected differences from changes in source spectral distribution. Therefore, it is probable that an experimental verification of the computations using the available opposed disk model would not clearly demonstrate the effect of a source mismatch. In view of these findings it is obvious that further experimentation with the opposed disks, using available source facilities, is not appropriate for a study of thermal errors caused by source spectral mismatch.

Appendix B

TUNGSTEN FILAMENT LAMP CHARACTERISTICS

Performance of the experimental program reported in Section 3 and completion of the computations of Appendix A each required knowledge of the spectral emissive power of the tungsten filament lamps. The lamps used were G. E. type T-3, 120 volt, quartz enclosed single wound tungsten filament lamps backed with Cerrogold coated Research Inc. reflectors.

A spectral calibration was performed to establish the spectral emissive power of these lamps as a function of supply voltage. This was accomplished by comparison to an N. B. S. calibrated strip lamp over the wavelength range 0. 25 to 5. 00 microns. The voltage range covered was 15 to 115 volts.

The calibration arrangement is shown in Fig. B-1. S_1 is a working standard whose spectral radiance was known and S_2 the unknown radiant source. M_1, M_2, and M_4 are plane front surface aluminized mirrors. M_3 is a 61 cm focal length, spherical, first surface mirror used to establish an image of the source on the entrance slit, S, of the Perkin-Elmer Model 98 monochromator. C is a 13 cps mechanical chopper. The magnification of the image at the entrance slit was 2 : 1.

The calibration was performed by direct comparison of energy emitted from the unknown source to that from the standard. This was accomplished by rotation of mirror M_1 to alternately place energy from S_2 and S_1 on the entrance slit. This procedure eliminates effects of surface absorptance in the optical system, path length, and considerations of variable slit width.

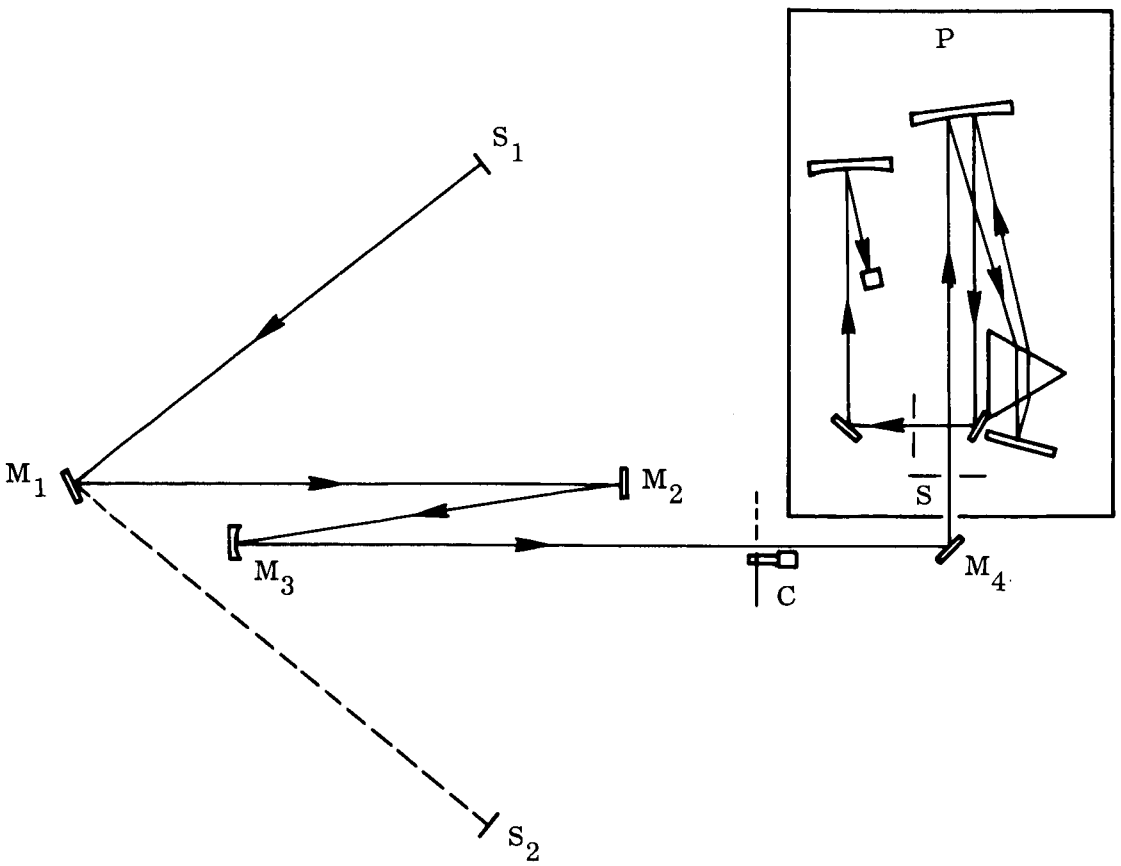

Fig. B-1 Lamp Calibration Apparatus

Power supplied to the T3-500 lamps was monitored using a 0 to 300 volt, 1/2%, triple range Weston voltmeter and a 0 to 10 amp, 1/2%, triple range Weston ammeter. The power source was a Research Inc. silicone rectified phase sensitive power supply. This type of power supply controls energy by modification of the supply voltage wave form rather than variation of the input sine wave amplitude. Therefore, the readings obtained for voltage and amperage using standard meters are not true indications of the power level of the lamp. However, the readings are repeatable using the same meters so that known radiant conditions are obtained at prescribed voltage readings. The same instruments were used when chamber calibration was performed.

Lamp filament temperature was also determined during the spectral calibration. This data can be used to establish or determine lamp conditions since the filament temperature is directly related to the spectral emissive power. The apparent filament temperature was measured using a Pyro Microptical Pyrometer manufactured by the Pyrometer Instrument Co. The observed values were adjusted using published data on the brightness temperature of tungsten. Significant gradients were observed along the filament length for lamp operation at 40 and 15 volts. The lowest observed temperature was for areas near the filament supports which acted as cooling fins. For example, with 40 volts on the lamp, the filament temperature between supports was 1625°K while at a support it was 1510°K. The data given for filament temperature is for the highest temperature region. The filament temperatures are presented in Table B-1.

Table B-1

FILAMENT TEMPERATURES FOR G. E./T3-500 TUNGSTEN FILAMENT LAMPS

Operating Condition		Filament Temperature (°K)
Volts	Watts	
115	465	2420
90	351	2225
65	194	1995
40	92	1625

Results of the spectral calibration are presented in Table B-2 as a function of wavelength and voltage. Those entries omitted from the table were not determined due to insufficient energy for comparison to the reference standard. This data was plotted in terms of the relative spectral radiance and is presented in Fig. B-2. These curves represent the basic information required for computation of surface absorptance at specified voltages.

The experimental accuracy of the calibration is estimated as 5% for the three highest voltages and 8% for the 40 volt operating condition. This decrease in accuracy was caused by the uncertainty involved when directly comparing a low intensity source to a high intensity standard. Changes in amplifier settings were required over ranges which were slightly nonlinear.

The accuracy of the 15 volt determination cannot be definitely stated since the lamp energies were very low level requiring changes on both amplifier gain and slit width. The monochromatic band pass and slit width were used to compute the apparent energy level of the unknown lamp. This procedure is indirect and may have introduced large errors into the final result.

Table B-3 presents a comparison of observed maximum energy wavelengths from Table B-2 and those computed using the filament temperatures and Planck's radiation law. The comparison was excellent for the three highest operating levels. At 40 volts the discrepancy was somewhat larger and was consistent with the increased experimental error.

Table B-2

SPECTRAL RADIANCE OF G. E./T3-500 INFRARED LAMP
WITH CLEAR QUARTZ ENVELOPE

Microwatts

Steradian-Nanometer – mm^2 of source

Wave-length	115V	90V	65V	40V	15V
0.25	5.77×10^{-3}	6.74×10^{4}			
0.27	2.21×10^{-2}	3.03×10^{-3}	2.60×10^{-5}		
0.30	9.30×10^{-2}	1.30×10^{-2}	1.74×10^{-4}		
0.35	7.01×10^{-1}	6.67×10^{-2}	5.20×10^{-3}	3.64×10^{-5}	
0.40	2.73×10^{0}	4.45×10^{-1}	2.71×10^{-2}	2.19×10^{-4}	
0.45	7.32×10^{0}	1.57×10^{0}	1.05×10^{-1}	1.52×10^{-3}	
0.50	1.57×10^{1}	4.62×10^{0}	4.53×10^{-1}	6.05×10^{-2}	
0.55	3.56×10^{1}	1.01×10^{1}	1.05×10^{0}	1.83×10^{-2}	
0.60	5.78×10^{1}	1.60×10^{1}	1.92×10^{0}	3.13×10^{-1}	
0.65	6.95×10^{1}	2.25×10^{1}	2.96×10^{0}	6.03×10^{0}	
0.70	8.62×10^{2}	3.65×10^{1}	7.32×10^{1}	1.72×10^{0}	
0.80	1.29×10^{2}	6.32×10^{1}	2.50×10^{1}	4.00×10^{0}	
0.90	1.70×10^{2}	9.30×10^{1}	4.60×10^{1}	8.20×10^{0}	
1.00	1.92×10^{2}	1.13×10^{2}	6.17×10^{1}	1.34×10^{1}	
1.10	2.20×10^{2}	1.22×10^{2}	7.15×10^{1}	1.81×10^{1}	
1.20	2.22×10^{2}	1.28×10^{2}	7.87×10^{1}	2.20×10^{1}	2.62×10^{0}
1.30	2.10×10^{2}	1.29×10^{2}	8.30×10^{1}	2.52×10^{1}	3.72
1.40	2.00×10^{2}	1.28×10^{2}	8.50×10^{1}	2.68×10^{1}	4.37
1.50	1.75×10^{2}	1.17×10^{2}	8.60×10^{1}	2.70×10^{1}	5.86
1.60	1.68×10^{2}	1.08×10^{2}	8.40×10^{1}	2.73×10^{1}	7.25
1.70	1.52×10^{2}	1.00×10^{2}	7.90×10^{1}	2.76×10^{1}	8.00
1.80	1.36×10^{2}	8.89×10^{1}	7.20×10^{1}	2.64×10^{1}	8.37
1.90	1.14×10^{2}	8.07×10^{1}	6.42×10^{1}	2.31×10^{1}	9.25
2.00	1.00×10^{2}	7.30×10^{1}	5.60×10^{1}	2.28×10^{1}	9.50
2.10	8.80×10^{1}	6.31×10^{1}	4.92×10^{1}	2.12×10^{1}	9.60
2.20	7.86×10^{1}	5.92×10^{1}	4.63×10^{1}	1.95×10^{1}	9.62
2.30	6.91×10^{1}	5.37×10^{1}	4.10×10^{1}	1.85×10^{1}	9.40
2.40	6.46×10^{1}	4.87×10^{1}	3.68×10^{1}	1.63×10^{1}	9.25
2.50	5.70×10^{1}	4.46×10^{1}	3.45×10^{1}	1.57×10^{1}	8.79
2.60	5.23×10^{1}	4.11×10^{1}	3.30×10^{1}	1.50×10^{1}	8.50
2.70	4.55×10^{1}	3.62×10^{1}	2.94×10^{1}	1.42×10^{1}	8.12
2.80	4.14×10^{1}	3.20×10^{1}	2.57×10^{1}	1.35×10^{1}	7.81
2.90	3.52×10^{1}	2.71×10^{1}	2.20×10^{1}	1.22×10^{1}	7.30
3.00	3.05×10^{1}	2.44×10^{1}	1.97×10^{1}	1.07×10^{1}	6.90
3.50	1.90×10^{1}	1.60×10^{1}	1.17×10^{1}	6.40×10^{0}	4.50
4.00	8.80×10^{0}	7.70×10^{0}	5.90×10^{0}	3.50×10^{0}	2.90
4.50	3.20×10^{0}	2.80×10^{0}	2.20×10^{0}	1.80×10^{0}	1.30
5.00	1.80×10^{0}	1.40×10^{0}	7.00×10^{-1}	3.00×10^{-1}	

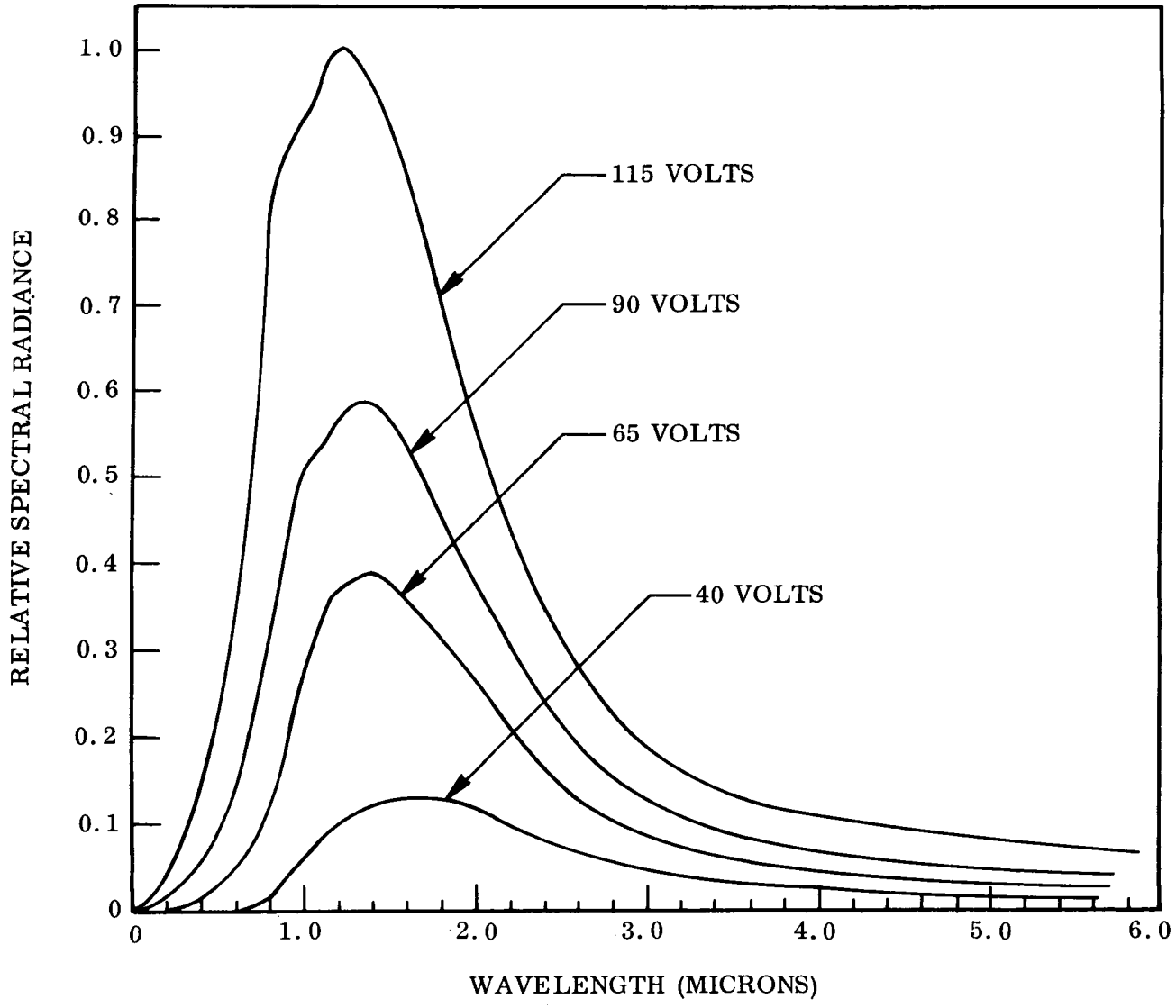

Fig. B-2 Relative Spectral Radiance of G.E. Type T3-500 Quartz Lamp

Table B-3

MAXIMUM SPECTRAL RADIANCE WAVELENGTHS

Voltage	Power (watts)	λ_{max} From Table B-2	λ_{max} From Filament Temperature
115	465	1.20	1.20
90	351	1.30	1.30
65	194	1.40	1.45
40	92	1.70	1.78

SURFACE ABSORPTANCE

The total absorptance of a surface for energy incident from any source is defined as

$$\alpha = \frac{\int_0^\infty \alpha_\lambda E_\lambda \, d\lambda}{\int_0^\infty E_\lambda \, d\lambda} \qquad \text{(B.1)}$$

where

λ = wavelength

α_λ = spectral absorptance of the surface at wavelength λ

E_λ = monochromatic emissive power of source

Evaluation of the integral requires knowledge of α_λ and E_λ which are measured separately in the laboratory. These properties are seldom easily described mathematically as functions of λ so that the data are presented in tabular or graphical form. Also, data referring to the spectral distribution of sources are normally

presented in a relative form similar to that used in Fig. A-2 rather than as absolute data as presented in Table A-2. Given that tabular data of the properties are available, the computation is performed by summation over the data points using the relation

$$\alpha = \frac{\sum_{n=1}^{N} \alpha_{\lambda n} \left[E_{\lambda n}/E_{\lambda \max}\right] \Delta_{\lambda n}}{\sum_{n=1}^{N} \left[E_{\lambda n}/E_{\lambda \max}\right] \Delta_{\lambda n}} \qquad \text{(B. 2)}$$

where

$\alpha_{\lambda n}$ = average absorptance over wavelength interval $\Delta_{\lambda n}$

$E_{\lambda n}/E_{\lambda \max}$ = average relative spectral emissive power over $\Delta_{\lambda n}$

Selecting sufficiently narrow uniform wavelength intervals provides reasonable accuracy in the result. A better summation procedure is to select the $\Delta_{\lambda n}$ so that each interval represents an equal amount of source energy.

These intervals are established from the relation

$$\Delta_{\lambda} = \frac{E_{\lambda \max}}{E_{\lambda n}} \frac{}{N} \sum_{n=1}^{N} \left[\frac{E_{\lambda n}}{E_{\lambda \max}}\right] \Delta_{\lambda n} \qquad \text{(B. 3)}$$

This procedure was used for integration of spectral properties quoted in this report.

Figure B-3 presents the spectral reflectance of materials used on the models referred to in Section 3 and for the computations performed in Appendix A. These properties were determined using procedures that are presently accepted as standard for spectral reflectance measurements. The spectral near normal reflectance from 0. 27 to

2.5 microns was measured in a Gier-Dunkle integrating sphere attached to a Perkin-Elmer model 98 monochromator. In this instrument the sample receives energy from the monochromator at an angle of approximately 7 circular degrees off normal and reflects hemispherically to the sphere walls. The instrument response is observed first for direct sphere irradiation and then for sample irradiation. After correction for entry port and detector port losses, the ratio of readings provides the absolute spectral reflectance of the test surface.

The spectral near normal reflectance from 2.0 to 5.0 microns was determined using a heated cavity reflectometer attached to the inlet slits of a Perkin-Elmer model 98 monochromator. In this system a sample is exposed to the infrared energy of a high temperature cavity by placing it inside the high temperature region. The sample is maintained at room temperature by water cooling of its back surface. External optics are used first to view the cavity wall and then the sample surface to obtain a ratio of energy levels from these two sources. The ratio of readings must be corrected for sample emission and entry port effects to obtain the true value of spectral reflectance. Again, the sample is viewed at an angle of 7 circular degrees off its surface normal.

The spectral curves of Figs. B-2 and B-3 were used to establish surface absorptance as a function of lamp voltage over the voltage range of 10 to 115 volts. The results of these computations are presented in Fig. B-4. Comparison of the curves shows that the different surfaces provide considerable changes in surface absorbance with both positive and negative slopes. These changes with voltage are sufficient to double the absorptance and must be considered when establishing chamber conditions for the model test.

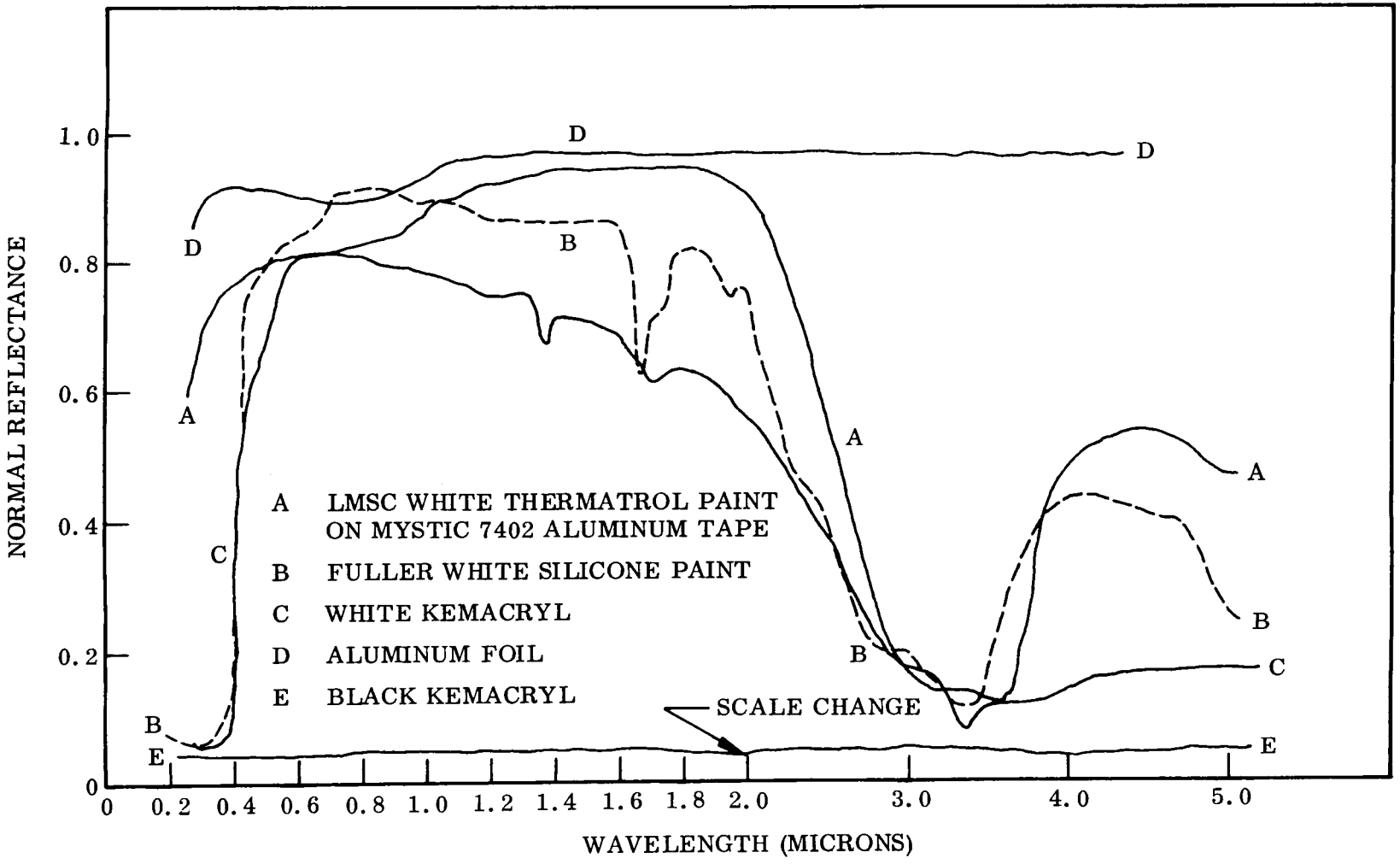

Fig. B-3 Spectral Reflectance of Standard Thermal Control Surfaces

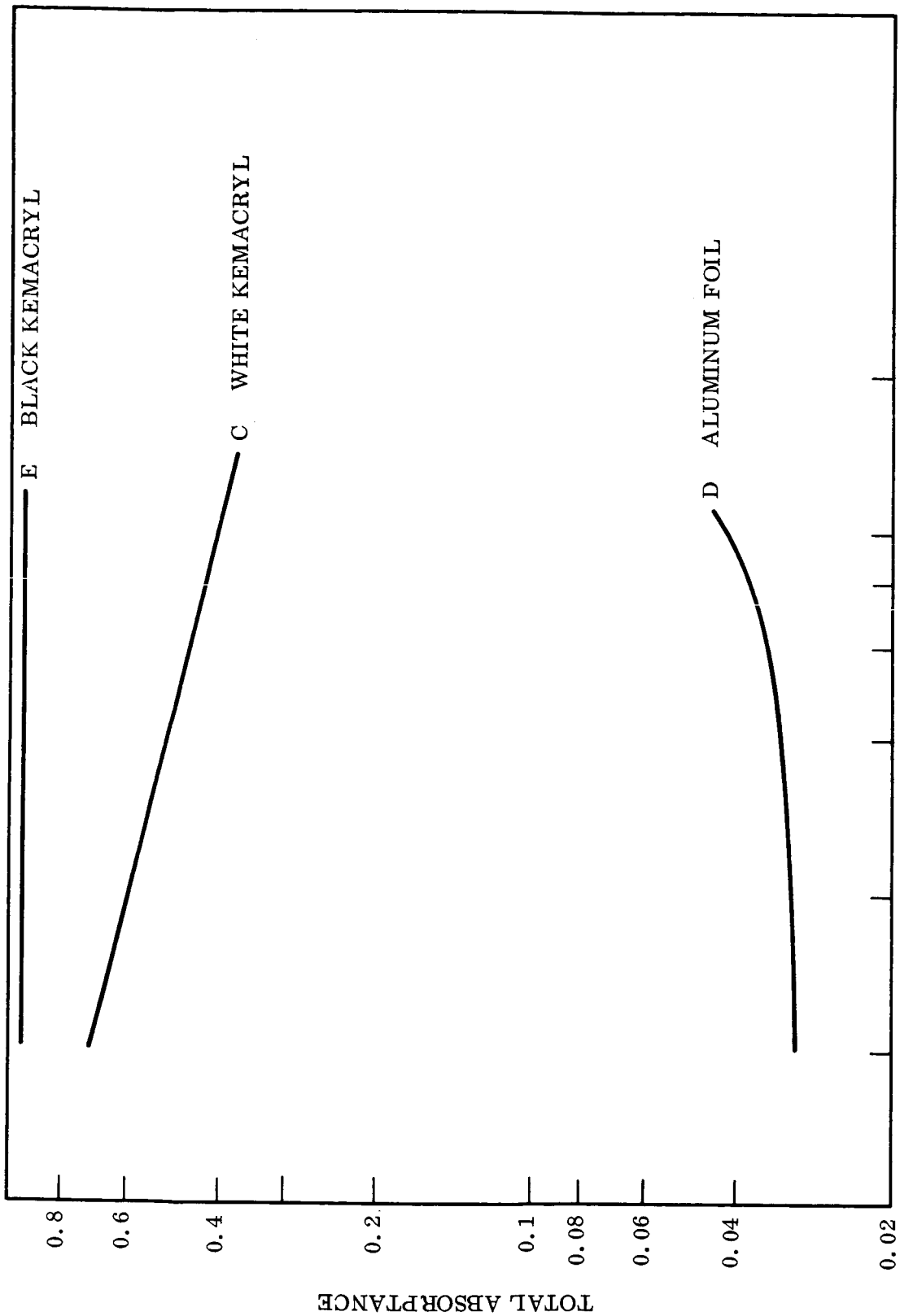

Fig. B-4 Surface Absorptance for G.E. T3-500 Reflector Backed Lamps

Appendix C
SOURCES OF ERROR

The accuracy of model predictions is governed by the uncertainties associated with two distinctly separate phases of the model study. A portion of the overall error is introduced during design and construction of the model. The models prediction accuracy will depend upon how well its construction completely satisfies the model criteria. Therefore, variations in thermal properties of materials, radiative properties of surfaces, dimensional tolerances, and thermal behavior of joints must be controlled or eliminated during this phase of the effort. Additional uncertainties are introduced during the experimental effort and these are associated with random or systematic experimental errors. Since the overall accuracy is affected by these two independent sources they are treated separately in this appendix.

C.1 EXPERIMENTAL ERROR

The accuracy of the experimental measurements performed during model tests is governed by the same sources of error as the accuracy achieved during full-scale testing. For the tests conducted in this program the major sources of error were in temperature measurement, control of internal energy dissipation, control of external radiant energy sources, and for the steady periodic tests, control of heater and source bank periodicity. An estimate of probable experimental error can be established by considering the accuracy of each of these independent contributing sources.

C.1.1 Temperature Measurement

For copper-constantan thermocouples calibrated on model before test operations. Average temperature 300°K.

Steady-state readout accuracy	±10 μv (±1/4° K)
Periodic readout accuracy	±40 μv (±1° K)
Thermocouple calibration	±40 μv (±1° K)
Installation and response uncertainty	±60 μv (±1-1/2° K)
Estimated maximum error	±140 μv (±3-1/2° K)
Estimated probable error (rms)	±82 μv (±2° K)

C.1.2 Internal Energy Dissipation

For tungsten filament heater at 100 watts ($1^{\underline{a}}$, $100^{\underline{v}}$)

Power readout accuracy	±1 watt
Line and feedthrough losses (30 ft of 20 ga. copper wire at 0.010 ohms/ft)	±0.3 watt
Voltage fluctuation (±1/2%)	±0.5 watt
Estimated maximum error	±1.8 watts
Estimated probable error (rms)	±1.15 watts

C.1.3 External Radiant Energy

For 15 tungsten filament lamps placing 0.14 watt/cm^2 on surface of test object

Calibration accuracy (from 0 to $115^{\underline{v}}$ averaged over frontal area of specimen with ±5% uniformity)	±0.01 w/cm^2
Control accuracy (using Thermac feedback temperature controller)	±0.003 w/cm^2
Estimated maximum error	±0.013 w/cm^2
Estimated probable error (rms)	±0.01 w/cm^2

C.1.4 Effect of Error in Energy Rates on Temperature

Errors in measurement or control of model energy rates are directly related to errors in model temperatures. Since the energy absorbed or dissipated by the model is in balance with that emitted to the surroundings, then variations in energy are related to variations in overall model temperature through the 4th power of absolute temperature. For local points in the model, for example the top of the heater box on the opposed disks, this dependence does not apply since conduction plays a strong part in distributing the energy to other connecting members. In these regions a change in energy rate causes a change in temperature with other than 4th power dependence. The actual effect for such regions must be evaluated experimentally by observation of changes in temperature for small step changes in energy. However, since such data was not obtained during the experimental effort, the 4th power dependence will be used as an overall estimate of error. Therefore, it is assumed that

$$K_1 \Delta E_1 + K_2 \Delta E_2 = \Delta(T^4) \qquad \text{(C.1)}$$

where

ΔE_1 = small variation in radiant energy

ΔE_2 = small variation in internal energy dissipation

K_1, K_2 = constants

$\Delta(T^4)$ = small variation in 4th power of model temperature

The thermal error caused by ΔE_1 and ΔE_2 can be expressed as

$$\frac{\Delta E_1 + \Delta E_2}{4(E_1 + E_2)} = \frac{\Delta T}{T} \qquad \text{(C.2)}$$

For $E_1 \approx 250$ watts, and $E_2 \approx 100$ watts and the measurement errors estimated above, the results are

Estimated maximum error due to energy measurement or control	$\frac{\Delta T}{T} = 0.016$
Estimated probable error due to energy measurement or control (rms)	$\frac{\Delta T}{T} = 0.012$

The total experimental error is the sum of the individual errors due to temperature measurement and energy control.

Estimated maximum experimental error in temperature	2.8%
Estimated probable experimental error in temperatures	1.9%

These values correspond to errors in absolute temperature of approximately 8.5° K and 5.5° K at an average prototype temperature of 300° K.

The above treatment is based upon the assumption that neither systematic nor human errors occurred during the experiments. A study of the experimental results failed to indicate large systematic errors in the steady-state measurements though such errors were certainly encountered during the steady-periodic runs. These were caused by improper control of lamp bank cycles and are clearly evident in the data presented in Section 3. For the half-scale model of the truncated cone the prototype prediction was in error on the order of 20° K at the peak of the heating cycle. This was caused by improper intensity control during the cycle. For the quarter-scale cone model the period was controlled within 3 sec of the required 90 min with excellent predictions obtained. Comparison of these results provides a measure of the error caused by improper control of lamp bank periodicity and amplitude.

Variations in cold wall temperature are also a potential source of experimental error. For the experiments conducted during this program the cold wall temperature was constant at an average value of 83° K. Correct testing of the half-scale models, whose temperature ratio was 1.13, required a cold wall temperature of 94° K. This condition could not be provided using the present cooling system. However, for an average sample temperature of 300° K, the prediction error caused by the coolder cold wall condition is approximately 0.077% or 0.23° K. This low magnitude was considered negligible and was not accounted for during the data reduction process.

C.2 ERRORS DUE TO MODEL DESIGN

Thermal designs of the models used during this program were performed as much as possible in accordance with the model criteria. This required the use of identical surfaces, geometric distortion of all conducting paths, geometric distortion of some radiative paths, the construction of filled bolted joints, and reasonable duplication of internal heater geometries. With these models it is possible that errors were introduced during both the design and construction phases.

C.2.1 Errors Due to Distortion of Conducting Paths

The conducting paths through plate and tubing were geometrically distorted in thickness to provide proper ratios of A_n^* and θ^*. For the tubing, it is estimated that this distortion caused a negligible error in overall performance since the desired axial heat transfer was achieved along the length of tubes. The distortion resulted in non-conformance with similarity criteria for conduction across the tubes and for radiation between the outer tubular surface and the surrounds. However, the overall thermal performance of the designs was not strongly dependent upon these characteristics; therefore, the effect of this distortion was assumed negligible. Computations performed during the design phase confirmed this assumption and indicated that the change in radiative slope factors was less than 0.1%.

For the plate material, distorted thicknesses provided proper similarity along the length of the plate, but gradients across thicknesses were not preserved. For most regions in the models the energy rates through surfaces were sufficiently low to neglect the distortion in thickness. However, for regions having high flux levels, such as the heater boxes, this is not the case. The heater box on the opposed disk was constructed of 6061 aluminum and dissipated 100 watts. Assuming that this energy was uniformly distributed over the box would give a gradient of 0.24° K/cm through the box thickness for the full scale object. The corresponding total gradient would be 0.075° K. For the distorted thickness used on the half-scale model the predicted total gradient would be 0.038° K while the distorted quarter-scale model would predict 0.47° K.

Thus, the distortion used in design of the quarter-scale stainless steel model introduced a prediction error on the order of 0.5° K for the heater box surface temperature under steady-state conditions. Under transient conditions the error is more difficult to estimate due to the complexity of the geometry involved. However, consideration of the test results indicates an error on the order of 10° K for the opposed disk quarter-scale model. It is doubtful that this was caused solely by distortion of the box thickness since the joints, heater filament location, thermocouple installation, and power level also are potential contributors to an error at this location.

C.2.2 Errors Due to Thermal Variations in Properties

The possible influence of changes in thermal properties was presented in Section 2 where it was shown that for materials having exponential temperature dependence the properties could be represented by

$$K_n = \bar{K}_n T^a \tag{C.3}$$

and

$$C_p = \bar{C}_p T^b \tag{C.4}$$

The model ratios of properties become

$$K_n^* = \bar{K}_n^* T^{*a_m} T_p^{(a_m - a_p)} \tag{C.5}$$

$$C_p^* = \bar{C}_p T^{*b_m} T_p^{(b_m - b_p)} \tag{C.6}$$

where

K_n = thermal conductivity

$\bar{K}_n$ = constant

a = thermal conductivity temperature coefficient

C_p = specific heat

$\bar{C}_p$ = constant

b = specific heat temperature coefficient

Equations (C.5) and (C.6) show that for the conditions given in Eqs. (C.1) and (C.2), the thermal property ratios are variable over the entire temperature range when $a_m \neq a_p$. The amount of variation can be assessed by direct evaluation of K_n^* and T^* at the upper and lower temperature limits of the experiment.

Table C-1 presents values for the temperature coefficients and is based upon published values of K_n and C_p at 273° K and 360° K. Considerable variation exists in reported values for these properties; therefore, average values were selected for the tabulation. Performing the computation indicated by Eqs. (C.5) and (C.6) for the quarter-scale model shows an 18 percent change in K^* over the prototype temperature range of 273° K to 360° K. This corresponds to a 6 percent change in T^*. For C_p^* the change over the same temperature range is 2.1 percent, corresponding to a variation in θ^* of 16 percent. These results indicate the possibility of large model errors due to the significantly different values of a and b for the stainless steel model and aluminum prototype. However, the actual thermal

Table C-1

COEFFICIENTS FOR THERMAL CONDUCTIVITY AND SPECIFIC HEAT[(a)]

	K (cal/sec cm°K)		C_p (cal/gm° K)					
Material	273°K	360°K	273°K	360°K	a	b	$\bar{K}$	$\bar{C}$
304 S.S.	0.033	0.038	0.110	0.117	0.5	0.2	0.002	0.036
6061 Al	0.41	0.42	0.230	0.237	0.07	0.11	0.025	0.075

(a) Data represent average values taken from published information. Various investigators report ±15% variation from the tabulated values.

error depends upon the system under investigation. For the stainless steel model the change in specific heat ratio was of minor influence since it was of small magnitude. The error caused by variation in K* must be evaluated in terms of the conductive heat rates involved. For example, the opposed disk model had a large gradient from the front to rear disks with only minor gradients in the radial directions. Therefore, the temperature distribution of the disks themselves would not be seriously affected by an incorrect value of K*. However, the connecting legs would suffer from changes in K* in the axial direction since the front to back gradient was imposed across the ends. For the quarter-scale model where T* was nominally chosen as unity, the expected error in center temperature, due to changes in K*, would be on the order of 2 percent or 5° K.

For transient runs on the quarter-scale opposed disks the changes in K* and C_p^* indicate a variation in θ^* of approximately 16 percent during a single period, for those elements undergoing 100° K thermal changes. This changing time constant partially accounts for the less accurate predictions obtained from the transient runs.

As indicated by Eqs. (C.5) and (C.6), the temperature exponents a and b must be considered in establishing the model ratios. For cases where $a_m = a_p$, $b_m = b_p$,

and $T^* \neq 1$, the model ratios become

$$\frac{\rho^* V^* \bar{C}_p^* T^{*(1+b)}}{\theta^*} = A_I I^* = Q^* = \frac{\bar{K}_n^* A_n^* T^{*(1+a)}}{L^*} = A_i^* T^{*4} \qquad (C.7)$$

The half-scale models utilized identical materials thereby satisfying the requirements $a_m = a_p$ and $b_m > b_p$. Therefore, these models are governed by the criteria of Eq. (C.7). Rearrangement of the formulation gives

$$T^* = \left[\frac{\bar{K}_n^* A_n^*}{L^{*3}}\right]^{(3-a)^{-1}} \qquad (C.8)$$

$$\theta^* = \frac{\rho^* \bar{C}^* L^{*2}}{\bar{K}_n^*} T^{*(b-a)} \qquad (C.9)$$

In this form it is clear that a and b must be constant throughout the model to provide constant temperature and time ratios. For the models tested in this program, constant values of the exponents existed for all elements since a single material was used for model construction. Where dissimilar materials are used for construction the values of a , b and (b - a) must be held constant to provide single values of θ^* and T^*. Again, the absolute magnitude of error due to variations of these exponents must be assessed in terms of the thermal behavior of each element.

C.3 SUMMARY

The considerations presented in the previous paragraphs point out the potential sources of error in the experimental program. The overall error associated with experimental measurements is estimated as ±5° K. These are average values and are subject to considerable modification depending upon the thermocouple location involved. Inspection of the experimental results shows that this estimated error is of the proper order with the exception of transient predictions for heater box

temperatures. For those regions the prediction error was on the order of 10° to 20° K. It is apparent that a different approach should have been used in design of the heater boxes to assure better compliance with the model criteria.